3-12-2020

# Adaptive, High-Resolution Ultrasound Phased Array Imaging for use in the Inspection of Laser Brazed Joints in the Automotive Sector

Andrew Ouellette
*University of Windsor*

# Adaptive, High-Resolution Ultrasound Phased Array Imaging for use in the Inspection of Laser Brazed Joints in the Automotive Sector

By

Andrew Ouellette

A Dissertation
Submitted to the Faculty of Graduate Studies
through the Department of Physics
in Partial Fulfillment of the Requirements for
the Degree of Doctor of Philosophy
at the University of Windsor

Windsor, Ontario, Canada

2020

Adaptive, High-Resolution Ultrasound Phased Array Imaging for use in the Inspection of Laser Brazed Joints in the Automotive Sector

by

Andrew Ouellette

APPROVED BY:

T.P. Chu, External Examiner
Southern Illinois University

S. Chowdhury
Department of Electrical and Computer Engineering

W. Kedzierski
Department of Physics

D. Xiao
Department of Physics

R. Maev, Advisor
Department of Physics

February 3rd, 2020

## DECLARATION OF ORIGINALITY

I hereby certify that I am the sole author of this thesis and that no part of this thesis has been published or submitted for publication.

I certify that, to the best of my knowledge, my thesis does not infringe upon anyone's copyright nor violate any proprietary rights and that any ideas, techniques, quotations, or any other material from the work of other people included in my thesis, published or otherwise, are fully acknowledged in accordance with the standard referencing practices. Furthermore, to the extent that I have included copyrighted material that surpasses the bounds of fair dealing within the meaning of the Canada Copyright Act, I certify that I have obtained a written permission from the copyright owner(s) to include such material(s) in my thesis and have included copies of such copyright clearances to my appendix.

I declare that this is a true copy of my thesis, including any final revisions, as approved by my thesis committee and the Graduate Studies office and that this thesis has not been submitted for a higher degree to any other University or Institution.

## ABSTRACT

The inspection of welded and brazed joints has been performed in several industries using ultrasonic phased array. In the automotive sector, many of the current standards for brazed joint inspection do not apply due to the high variations in surface geometry and limited accessibility to the inspection region. As the automotive industry looks to integrate laser brazing into the production process, the need to determine the size and geometry of the joint, as well as the presence of any defects, is desirable to ensure product quality and reduce costs. Currently, the use of destructive techniques, such as cross-sectioning, is employed in the inspection process, with the ultimate desire being the shift to non-destructive methods. With this in mind, ultrasonic techniques have been investigated as a possible testing method.

Ultrasound techniques have evolved over the decades, starting from a single element and eventually moving to phased array techniques. Recently, the investigation of the full matrix capture method has become popular in the field of ultrasound imaging. This technique, which separates the data acquisition process from the image formation process poses a viable solution to the inspection of laser brazed joints due to the ability to compensate for varying surfaces in post-processing.

In this work, we make use of this technique, deriving the image formation process as an inverse problem for an arbitrary set of ultrasonic emitters and receivers. From this, the image formation process becomes equivalent

to solving the inhomogeneous Helmholtz equation. By approximating the solutions to such an equation using the ray series expansion, an estimation of the solutions can be found in a time-efficient manner. When these solutions are found, the inverse process can be rewritten as a weighted, time-delayed summation of the acquired ultrasonic data.

In current work, further approximations to this image formation process are often made; however, in the inspection of the laser braze process, these approximations are found to degrade image quality in a number of cases. In this work, we propose our second order corrections as a viable solution to increase the limit under which ultrasound imaging can currently occur. This is accomplished through the design of an ultrasonic array transducer and the manufacturing of a series of simulated defects, with the final assessment being performed on real joints.

These techniques were found to improve imaging in a select set of samples when the radius of curvature dropped below 2 mm. In these cases, the use of the amplitude weighting was found to drastically improve system resolution, allowing for the determination of joint size, geometry and the presence of defects.

## ACKNOWLEDGEMENTS

This work would not have been possible without the help from various individuals and organizations. In addition to Ford Motor Company, who provided the funding for this work, the contributions and feedback of both Dr. Bita Ghaffari and Dr. Elizabeth Hetrick, from Ford Research and Advanced Engineering have helped guide the project.

Within our group, Dr. Serge Titov provided much valuable feedback in the early stages of this work and Dr. Roman Maev for giving feedback throughout. Other group members, such as Dimitry Shinas have also given invaluable help in editing the work for clarity and helping to further the project's goals.

The contributions of Pragma NDT must be noted for the support they have provided in getting the acquisition hardware working with our specific project.

Finally, the support of administrative staff, particularly Sarah Beneteau and Kimberly Lefebvre. Without their help in regards to funding, navigating the university's bureaucracy, and acquiring replacement equipment following the numerous burglaries, my studies here would have ended long ago.

## TABLE OF CONTENTS

## LIST OF TABLES

## LIST OF FIGURES

# Chapter 1

# Introduction

## *1.1. Overview of Work*

Laser brazing is a commonly employed joining method in numerous industries, including the automotive sector. In the automotive sector, laser brazing is currently under investigation as a supplemental technique to welding, where it offers advantages in terms of its lower heat input, which reduces thermal stress and the formation of intermetallic compounds that occur during welding. Despite the advantages brazing offers, like all joining and manufacturing techniques, brazing is susceptible to the formation of a variety of defects. These defects, depending on the type, size and location, as well as the physical makeup of the joint, determine its overall yield strength. As a result of this, the determination of these parameters is crucial to ensure that the final product meets the design criteria and that the final assembly is safe to put into service. As the automotive sector operates on a large scale, such assurances prevent premature failure and critical failure, ensuring the safety of the public and the reputation of the manufacturer are maintained.

As part of the quality assurance process, cross-sectioning is currently performed at regular intervals to ensure process parameters are in line with the original specification. This physical sectioning is a destructive process and therefore selective by its nature, resulting in the production of scrap materials and an increased cost of production. In this work, we look to design an alternative inspection technique based on ultrasonic imaging, with the eventual goal being

the replacement of the current destructive technique with a non-destructive alternative. Such a technique must be capable not only of detecting the presence of defects but measuring the physical dimensions of the brazed joint. The limitations of any inspection technique must also be characterized, to ensure that the system is capable of being integrated into a quality assurance process.

Although ultrasound offers the potential for being a suitable replacement from a theoretical basis, the majority of ultrasonic inspections rely on the use of phased array, manual or electronic scanning. These techniques rely on operator training, and a priori knowledge of the inspected part to form high-quality images. In the laser brazing process, the melting of the brazing material results in a surface geometry that varies between samples, resulting in a majority of ultrasonic inspection systems being unviable for establishing an alternative to cross-sectioning. Despite this, the advent of recent technologies that can adapt the imaging process to an unknown geometry was expected to overcome many of these challenges.

In order to access the ability of the imaging system, the design of a transducer and the selection of acquisition hardware was undertaken as part of this project. After this was done, implementation challenges were overcome to allow for the scanning of production samples, including the design of a housing and coupling method, and the writing of code for the acquisition, processing and display of ultrasonic images. With this completed, currently available implementations were found to be insufficient in the imaging of brazed joints that displayed a surface curvature with a small radius.

After currently available techniques were found to be insufficient, the adaptation of inverse methods to a high-speed imaging technique was performed. These adaptations, once implemented, were found to correct for and explain the shortcomings of previous techniques, as well as propose future improvements that can be made. Using these techniques, discussed in this work, an evaluation of the limits of the ultrasound imaging technique was undertaken. This evaluation was conducted with both experimental and simulated data, on both idealized representations of brazed joints and physical samples.

When this was completed, it was determined that in many cases ultrasound imaging can form a viable measurement of laser brazed joints. The primary limitation of the imaging system was found to occur when the radius of the braze dropped below the 2 mm mark, where the surface physically limits the transmission of sound and degrades image quality as a result.

### *1.2. Author Contributions*

In order to complete this work, many sub-projects were undertaken by the author. The notable contributions in this work that were completed by the author are as follows,

- Design of ultrasonic array and selection of data acquisition hardware
- Design of a coupling method to inspect laser brazed joints
- Development of code to acquire and process data using current adaptive techniques
- Development of code to simulate wave propagation for use in second-order techniques

- Acquisition and simulation of data for comparison of current and newly proposed techniques
- Comparison of various techniques for imaging brazed joints
- Assessment of system limitations

Outside of the requirements of such a system, which are defined in accordance with our research partner, this work was completed by the author, with guidance provided by various parties as outlined in the acknowledgements section.

### *1.3. Dissertation Outline*

As the primary goal of this work is determining the viability of an ultrasound-based imaging system for inspecting laser brazed joints, this work starts with a review of the brazing process, explaining the relevant defects and measurements that are required for a system to be considered capable of performing an evaluation of the brazed joint. In this section, current methods are explored for comparative purposes.

Once the parameters of the braze joint have been established, the background information for wave propagation is dealt with from a theoretical perspective. This theoretical background serves as the basis for the discussion of the limitations of the current inspection technique, and the potential areas for improvement that can be explored in future work.

In order to facilitate the analysis of the system's capability, both numerical and experimental simulations of ultrasound waves must be conducted. In the next chapter, two numerical techniques, that of the pseudospectral finite element

method and that of ray-based modelling are used. The trade-off of accuracy versus performance of each method results in this work requiring both. This chapter also introduces the theoretical foundations of the ray series expansion from which much of the imaging and results section is formulated.

In the next section, the imaging method used in this work is derived using a change of basis notation. Using this format, a simple derivation of the image formation process can be formed from an inverse method. This inverse method is then simplified using the ray series expansion derived in the previous section. When this is done, the standard approach of delay and sum imaging used in many systems is shown to be a further approximation to this simplified expression. This allows for a clear theoretical basis as to why the original inspection technique fails. This section also reviews comparative techniques.

Following the theoretical establishment of imaging, the design of a transducer and selection of acquisition electronics that optimized the imaging process was undertaken. By optimizing the basis used in imaging, the ease of acquisition and quality of acquired images acquired in subsequent chapters is ensured.

In order to determine the viability of the imaging system, experimental and simulated data was acquired from a series of phantoms with a varying radius of curvature and the presence of a variety of defects. These phantoms were designed to simulate a series of defects that are expected in the brazed joint. This chapter shows under which circumstances image quality is improved and where it approaches that of traditional imaging theory.

In the second-last chapter, the investigation of a series of brazed joints, some of which were designed to contain defects is performed and compared to cross-sections and x-ray computer tomography. This chapter serves to establish the viability of an ultrasonic inspection system for assessing the quality of laser brazed joints.

In the final chapter, the limitations and abilities of the system are summarized, as well as the potential improvements that can be made to the system. It is found that the proposed system can detect a variety of defects, with the potential for characterization of defects possible once more data becomes available.

# Chapter 2

# Laser Brazing in the Automotive Sector

## *2.1. Introduction to Laser Brazing*

Brazing is a process in which two sheets are joined using a filler metal. Physically, it is similar to soldering, with the principle difference being the heat at which the filler metal melts. In an ideal case, these filler metals are chosen such that, above a temperature, they exhibit a wetting property with respect to the base material. A wetting property is defined by the measure of the contact angle between a liquid and a solid structure. If this angle, measured relative to the surface, is found to be greater than 90 degrees, the material is said to be non-wetting and will bead on the surface. If the wetting angle is less than 90 degrees, however, the liquid will display a tendency to flow across the surface of the material.

Physically, the wetting process is a balance between the free energy of each boundary along the edge, mainly the solid-liquid, $\gamma_{SL}$, the liquid-vapour, $\gamma_{LV}$ and the solid-vapour, $\gamma_{SV}$. In this manner, the contact angle, $\theta$, can be found through the relation,

$$\cos\theta = \frac{\gamma_{SV} - \gamma_{SL}}{\gamma_{LV}} \tag{1}$$

In this work, the primary focus is that of the flare at v-groove joint, shown in Figure 1. From an analysis point of view, the formation of such a joint can be performed fairly simply, where the contact angle for a uniformly heated sample

should be constant on all corners of the joint. The result, however, is rarely uniform due to the surface conditions, temperature variations in the workpiece and other parameters.

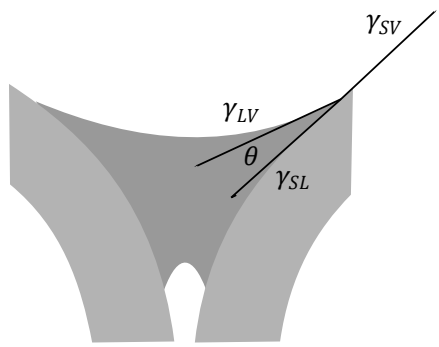


Figure 1 – An example of an idealized brazed joint between two plates. The metal is drawn into the workpiece until an energy balance is formed between each contact angle, as depicted for one section of the joint.

In the brazing process, unlike the soldering process, melting does not occur along a eutectic, and the fillers are not chosen to reach a lower melting point. In general, the fillers in the braze process are chosen to create mechanical strength in the joint and are often chosen from copper alloys with a weight percentage of copper greater than 90%. In this work, the percentage weight is in the 97% region, indicating that the phase composition of the material should be stable regardless of slight alloying changes[1]. This was confirmed using cross-sectioned joints comparing to the raw bronze of similar content.

With the advent of hybrid vehicles, consisting of mixed alloys of steel, aluminum alloys and other metals, a reduction in the vehicle weight and subsequent fuel costs can be realized[2]. These vehicles, however, pose an issue in the joining process. High strength steels, which have become far more common, are

susceptible to thermal cracking when melted[3]. Additionally, the intermetallic compounds formed in aluminum-steel joints prevent joining techniques such as welding from occurring[2]. As a result, alternatives to welding are currently being explored in the automotive industry.

Brazing is one such alternative, as the base material can be joined without the formation of intermetallic compounds caused by melting. Brazing has the additional benefit of reducing stress caused during welding while offering the ability of a continuous, high speed joining process that does not exhibit ageing effects common in rivets and adhesive joining. In the automotive industry, one of the primary brazing techniques being explored is that of laser brazing, where a laser is used to heat the substrate. Lasers offer many advantages over other heat sources due to the highly localized heating of the joint, resulting in an efficient and cost-effective process.

In this work, the formation of all joints was done at a partner facility. As a result, the choice of braze material, joint geometry, heating rates, wire feed rates, surface conditions and other factors that affect joint quality were not explored. The chosen parameters were based on the design of production samples or were varied to generate the desired defect. As a result, the details of the joining process parameters are completely excluded in this work, with only the resulting joint being available for analysis.

### *2.2. Defects Encountered in the Brazing Process*

The brazing process is robust; however, like all joining processes, it is susceptible to several types of defects. The severity of the defect is often

determined by the degradation of joint strength; however, the appearance may also play a role in acceptance. Defects can range from a joint not meeting a minimum size to more complex defects, such as the presence of pores, cracks and other abnormalities in the joint structure.

In this work, the primary desired quantity is that of the braze size. In general, the throat thickness, $D$, defined by the minimum thickness of the braze fillet must be determined alongside the leg lengths, $L_1$ and $L_2$, defined as the bond length between the braze and substrate. The geometric features of the braze joint are indicated in Figure 2; In general, the leg length is measured directly measure, rather than following the curvature of the part, yielding some deviation between the two.

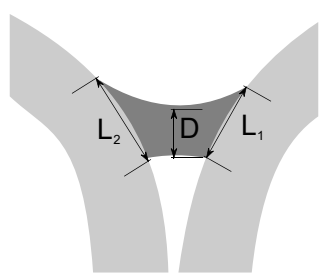


Figure 2 – A depiction of the braze joint measurement. The leg lengths, $L_1$ and $L_2$, are determined by the contact between the braze material and steel while the throat thickness $D$ is detmined by the minimum thickness of the joint.

In addition to this primary feature, any inspection technique should ideally be capable of determining the presence of any defects which hinder these measurements from being a relative indicator of joint quality. Due to the complexity of defect formation, isolation of a single defect in a workpiece was

found to prove difficult. For this reason, many example defects in both this section and the results section display a variety of defects simultaneously.

### *2.3. Porosity and Voids in Sample*

In a sample, porosity and voids can result from two primary processes, either gas being trapped during the formation of the joint, or differences in the solubility of atmospheric gases, which precipitate out of liquid during cooling. Inspection of braze joints should ideally determine the location, size and degree of porosity and voids within the sample. If the degree of porosity is low, as seen in Figure 3, it may not compromise joint quality as pores are known to be fairly stable under a variety of loading conditions.

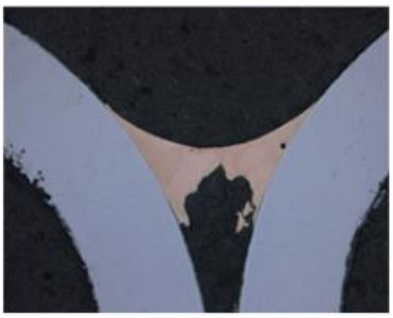

Figure 3 – A depiction of a small pore in the upper right of a malformed braze joint. If the number or size of pores becomes large, joint quality can be compromised.

#### *2.3.1. Inclusions and Flux Entrapment*

In the brazing process, flux, surface coatings or other materials can become entrapped in the braze metal. When this occurs, the quality of the joint can be affected in a manner similar to a pore or void being present. Depending on the material being entrapped, it is expected that only entrapment that results in the secondary defects to the joint would be detectable by any inspection.

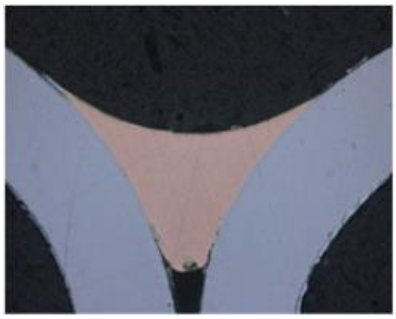

Figure 4 – An example of a zinc coating being entrapped in the braze material. This zinc coating appears to not have seriously affected the braze joint.

### *2.3.2. Noncontinuous fillet*

When the feed rate of wire is insufficient for the braze rate, or the geometry of the braze changes, the fillet can become non-continuous. This can result in variations in the throat thickness and, in extreme cases, a gap in the braze can form. As this effect occurs along the length of the braze, any measure to detect it would involve multiple measures along the braze surface, with uniformity established through these measures.

### *2.3.3. Lack of Adhesion*

If the surface of the material is contaminated or heating is uneven, the flow of material can be obstructed, resulting in no adhesions or a lack of adhesion. This defect, seen in Figure 5, shows a region under which adhesion did not occur, creating a small air gap in the sample. Depending on the location and extent of the defect, joint quality may be affected.

Figure 5 – An example of a lack of adhesion, where a region of incomplete fusion is present between the base material and filler.

### *2.3.4. Base-metal erosion*

If the laser travel speed is insufficient, the base material can melt, under which cases alloying can occur between the braze material and the base, resulting in lower yield strengths and potential intermetallics forming. This defect, seen in Figure 6, was not found viable for inspection with the techniques used in this work.

Figure 6 – An example of a void trapped in the brazing process. Melting of the base material is also found to be present.

### *2.3.5. Unsatisfactory Surface Appearance*

For any finished product, the surface appearance should be uniform. Although many process changes can affect surface appearance, the visibility of the surface results in it being outside of the scope of this project.

### *2.3.6. Crack*

Cracks in the braze material form when the braze material undergoes cooling stresses beyond its elastic limit. In these cases, the braze will form cracks along its surface. Cracking was not observed in any samples in this work.

## *2.4. Evaluation of Laser Brazed Joints*

In any process, deviations and defects can result in a product that does not conform to engineering standards for safety and appearance. These deviations must be controlled to create a product that does not pose a risk to the purchaser and is of a quality that a purchaser would not reject it. In order to ensure the quality of brazed joints, standards have been developed[4]; however, as only some standards apply to automotive joints, not all are discussed here. Additional resources for testing are presented based on active research where applicable. This review was conducted in parallel with one on welding[5] but due to a shift in project focus we shall only discuss brazed joints here.

### *2.4.1. Destructive Evaluation of Brazed Joints*

The destructive evaluation process is an inspection process that results in the sample being unfit for further use. Currently, destructive testing is predominantly used in the automotive sector, where a section of the joint is removed for x-ray or cross-sectional analysis. Although x-rays are a non-destructive testing technique, most currently available x-ray systems are not capable of imaging joints found in the automotive industry due to the size of the parts. As a result, an x-ray is typically a destructive process done on sectioned joints.

Cross-sectional analysis is a process whereby a specific location is sectioned and embedded in a resin polymer. This sample is then polished to a suitable degree to be viewed under a microscope for measurement. In addition, etching agents can be added, which dissolve the material based on the chemical resistance of the present alloys and allow for a characterization of the microstructure of the material. If the material chemical composition is of interest, it is also possible to perform x-ray fluorescence imaging, allowing for the mapping of the chemical makeup of a small region.

In this work, the base material was found to be relatively unchanged under etching, such that cross-sectioning was only used for joint geometry measurements. These sections, shown in the previous section, formed the initial analysis point; however, in the case of micro defects, such as porosity, the isolation of a pore during the cutting and polishing process posed a challenge, with x-ray being employed as an alternative measure.

### *2.4.2. Non- Destructive Testing Methods*

### *2.4.3. Visual inspection*

Visual testing, as the name implies, makes use of visual evaluation of a joint. Visual inspection often employs additional implements, such as radius gauges, which measure the radius of the joint, magnifiers and light sources.

In the inspection of brazed joints, visual inspection is limited in that only surface-breaking defects can be observed. As no physical measurement outside of the surface geometry can be made, visual inspection is employed only as a

supplemental technique. In this study, surface irregularities were noted as possible sites of defects within the samples provided.

In Figure 7, surface irregularities can be noted, including a region with burn marks; such irregularities are indicative of joint overheating. These surface defects have been used as an indicator of regions that may contain both surface and subsurface defects; however, defects have also been found in regions without such indicators.

Figure 7 – An image of a region in which visual inspection has yielded a possible overheating of the material. Such regions may need additional testing to ensure that this overheating has not compromised the joint quality or produced secondary defects.

### *2.4.4. Dye and fluorescent penetrant inspections*

Liquid penetrant inspection is a process that involves the use of visual inspection aided by a visible or fluorescent dye, which acts to aid in the detection of surface-breaking cracks and other defects.

The testing process involves a 3-stage inspection process. In the first stage, the liquid penetrant is applied and allowed to sit on the surface for a prescribed time. Using proper penetrant results in the liquid being drawn into the cracks through a

capillary effect. After removing excess penetrant from the surface of a part, the application of a developer draws the penetrant from the cracks, making a visible defect on the surface of a part.

Liquid penetrant testing poses some difficulty in the proper cleaning of parts but provides an application for the detection of surface cracks and surface breaking pores in traditional brazing techniques [6,7]. As such surface-breaking defects pose a detection issue in ultrasonic imaging, such techniques have the potential to supplement those discussed in this work.

#### *2.4.5. Acoustic emission*

Acoustic emission testing is an in-process method that may involve both ultrasonic and audible frequencies of sound waves. During the manufacturing process, the formation of cracks occurs due to residual stress within the material exceeding the elastic deformation limit. When this occurs, a fracture results, for which a distinct acoustic signature is produced. Other defects, such as oil on the surface of the metal will produce a signature based on its vaporization. This process has been used in the monitoring of laser welds[8–10] and could be implemented in the in-process detection of some defects in the laser braze process, such as cracking, quite readily.

Although acoustic emission has been used in the welding of joints, the isolation of the defect signal from surrounding noise is difficult in cases where the signature is of much lower strength. Access to the facility where the brazing occurs was limited during this research. As a result, this process was considered unviable, as it requires physical calibration in a plant-like environment.

### *2.4.6. Radiographic inspection*

Radiography is widely used in industrial processes. In general, a radiographic inspection can be separated into distinct areas, mainly radiographic imaging, and computed tomography. Some additional techniques, such as backscatter radiography[11], which allows for the examination of large workpieces, were determined to be a viable solution in the future, but as the process is still in its infancy, it does not currently offer the resolution required in this inspection. In this work, radiography has been used to supplement ultrasound imaging as it offers a much higher resolution. Despite this, the health concerns of radiation, cost of system and inspection part size limit most radiographic systems to a post-process destructive test in the automotive sector.

#### *2.4.6.1. X-ray Imaging*

X-ray imaging forms the basis of the subsequent techniques. In this form of imaging, a source of x-rays is used to radiate a sample. As the x-rays encounter the sample, the majority of them pass through the mostly empty martial, with a portion being reflected off of the nucleus of the atoms. These reflected x-rays result in a loss of the transmitted intensity. By placing an x-ray detecting film, or digital sensor on the opposite side of a sample, the number of x-rays hitting the detector over a period of time results in a recorded intensity or exposure. This process can be seen in Figure 8 below.

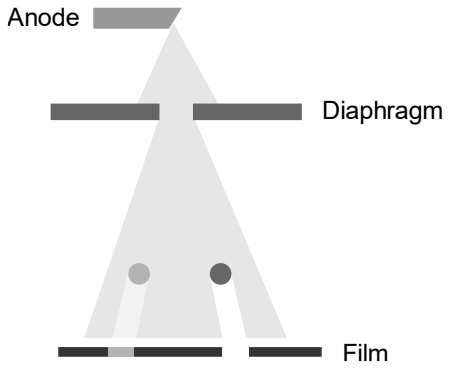


Figure 8 – A depiction of the x-ray process. the specimen obscures a portion of the x-ray based on its atomic number, resulting in variations in the exposure of the film or detectors placed opposite the source.

As the attenuation depends on the atomic number of the specimen, any change in material will result in a change in exposure in the resultant image. In this way, voids and cracks can be detected readily, with material changes resulting in a lesser contrast. To determine the additional parameters, such as the location of voids in the sample, the thickness of the sample, depth of cracks, etc. we must employ imaging techniques using a series of x-ray images.

#### *2.4.6.2. Tomographic Reconstruction*

This process relies on a series of x-rays taken at selected angles to localize defects such as pores inside of an inspected part. For a sample with a single pore, the use of a series of scans taken at different angles will produce images based on the location of the pore, as seen in Figure 9.

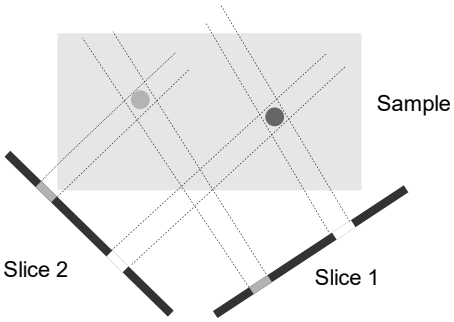


Figure 9 - A depiction of the tomographic x-ray method. Using a series of x-ray images, the location of defects such as voids can be determined. In cases where multiple defects are present, tomography is limited due to the inability to uniquely identify the location of the defect, as seen by the overlap in the back-traced image.

By tracing the location of the defect with respect to the orientation of the image with respect to the part, it is possible to determine the position of the defect in a 2d space. This technique is used in cases where a simple characterization is needed. As the series of images increases, the use of more complicated techniques used in x-ray computed tomography (x-ray CT) can be employed. Due to the smaller sample size, this technique must be done from a maximum likelihood point of view, rather than a standard statistical process used in x-ray CT[12].

#### *2.4.6.3. X-ray CT*

X-ray CT relies on the use of a plane wave inverse reconstruction technique known as the filtered back-projection algorithm. This process relies on the use of a series of CT images taken at differing angles along with the specimen. In general, a 3d reconstruction can be done by either translating such a detector or acquiring a series of 2d images, for which the back-projection becomes a volume.

By rotating the sample, a series of 2d projections can be collected at several angles. When the slices are put next to each other, they form what is known as a sinogram. The reconstruction process works in a similar manner as regular tomography while employing a sufficiently large sample set as to not require complicated statistical models.

Although outside of the discussion here, further filtering techniques based on inverse methods apply a weighting to the pixel based on the geometry of the problem at hand. Inverse problem form the basis upon which most modern CT's are based, allowing for higher quality reconstructions to occur. Even more quality can be gained using iterative processing; however, these processes are still used mostly in research applications.

In the imaging of brazed joints, x-ray CT's were used in this work for comparative purposes. These scans were performed externally, with the resultant images allowing for resolutions of greater than 0.1mm to be obtained on sections of the workpiece. These scans were used as a comparative method, however, as they require sectioning the workpiece, they are considered to be a destructive technique, and are not considered a viable testing method.

### *2.4.7. Ultrasonic inspection*

This section covers the current inspection methods for brazed joints. As the development of a new technique for this type of inspection is the focus of this work, detail of the laser brazes inspection technique used in this work is left for subsequent sections. In current ultrasonic inspection techniques, the geometry of the joint is often exploited to allow for imaging to occur. This is often performed

on pressure vessels, where an incident ultrasound beam produces a reflection from regions between two plates, as seen in Figure 10, where a reflection occurs from the interface between the flat plates. This technique can also be done using pairs of transducers or a phased array. Although this technique is accepted for brazed joints in some situations, the accessibility and geometry of the majority of brazed joints in the automotive sector significantly limits its applicability.

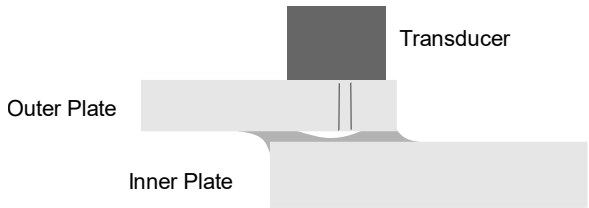


Figure 10 – An example of the braze inspection common in pressure vessels. Here the reflections of waves from any defects in the braze joint indicated by arrows can be analyzed as a simple 1D system.

Emerging techniques, upon which this work is based, allow for direct imaging through the surface of the joint. This is done using a variety of methods, but often makes use of phased array imaging to view through the surface. These techniques have emerged in the nuclear, oil and gas industry, where they are used to inspect welds in pipes [13]. The foundation of these techniques is covered in subsequent chapters on ultrasound imaging.

# Chapter 3

# Ultrasonic Propagation Theory

In this work, we deal with the propagation of ultrasound waves through matter, particularly solid and fluid media. This chapter discusses the propagation of waves, starting with the simple case of a fluid media, under which the derivation of non-linear effects can be performed. The propagation of stress waves in solid media is then discussed, along with the generation of sources and receivers from a conceptual perspective. Finally, some phenomena such as dispersion are discussed in a conceptual manner.

Both the fluid and stress wave derivations in this chapter are based on standard texts[14,15], with additional applications added where noted. As this chapter is designed to serve as the basis for subsequent chapters, readers unfamiliar with ultrasound are encouraged to read it.

## *3.1. Pressure wave in fluid Media*

In fluid media, sound waves are governed by the adiabatic equations that relate pressure and density, mainly, the equation for conservation of mass, Euler's equation and the adiabatic equation of state. These equations allow us to express the spatial and temporal variations of the pressure, $p$, density $\rho$ and velocity, $v$, as[14],

$$\frac{\partial \rho}{\partial t} = -\nabla \cdot \rho \mathrm{v} \tag{2}$$

$$\frac{\partial \mathrm{v}}{\partial t} + (\mathrm{v} \cdot \nabla)\mathrm{v} = -\frac{1}{\rho}\nabla p(\rho) \tag{3}$$

$$p = p_0 + \rho' \left[\frac{\partial p}{\partial \rho}\right]_S + \frac{1}{2}(\rho')^2 \left[\frac{\partial^2 p}{\partial \rho^2}\right]_S + \cdots \tag{4}$$

Where the equation of state is taken under the assumption of constant entropy. It is often of convenience to introduce a term, c, which is simply the speed of sound in fluid media.

$$c^2 \equiv \left[\frac{\partial p}{\partial \rho}\right]_s \tag{5}$$

### *3.1.1. Non-Linear Waves*

Although not explored in-depth in this work, non-linearity can be used in the field of imaging to gain some insight into the inspected material. If we compute the divergence of the second term in the uncoupled equations and substitute into the third, we can eventually find an expression for a new density, $\rho'$, in terms of the initial density[14],

$$\frac{\partial^2}{\partial t^2}\left(\frac{\rho'}{\rho_0}\right) = \nabla^2 c^2 \left(\frac{\rho'}{\rho_0}\right) + \frac{\rho}{c}\left[\frac{\partial c(\rho_0)}{\partial \rho}\right]\left(\frac{\rho'}{\rho_0}\right)^2 \tag{6}$$

Here, the concept of non-linear waves emerges as the fact that in the linear wave equation, we assume that the density does not change appreciably due to the propagation of the wave. When the intensity of the wave is great enough however, it is possible to have new behaviour emerge in relation to the change in density. One particular area of application is that of cracks, where small changes in pressure can result in hairline cracks opening or closing, resulting in differing reflections during imaging[16].

In the limiting case where the density does not change, we are left with the familiar wave equation of sound,

$$\frac{\partial^2}{\partial t^2}\psi = \nabla^2 c^2 \psi \tag{7}$$

Where the wave, $\psi$, is a solution of the given equation, with the choice of a variable being more commonly associated with waves. The Laplacian operator $\nabla^2$, takes its form depending on the symmetry of the problem.

### *3.2. Waves in Solid Media*

In a solid media, the isotropic elastic wave equation takes the form[15],

$$(\lambda + \mu)\frac{\partial \Delta}{\partial i} + \mu \nabla^2 u_i - \rho \frac{\partial^2 u_i}{\partial t^2} = 0, \text{for } i = x, y, z \tag{8}$$

Where the Cartesian coordinates, $\boldsymbol{x} = [x, y, z]^T$ define the spatial location of some points. The displacement field, $\boldsymbol{u} = \left[u_x, u_y, u_z\right]^T$, the density, $p(\boldsymbol{x})$, and the first and second lame constants, $\lambda(\boldsymbol{x}), \mu(\boldsymbol{x})$ as a function of position, $\boldsymbol{x}$, define the wave propagation. The dilation, $\Delta$, is defined in accordance with,

$$\Delta = \frac{\partial u_x}{\partial x} + \frac{\partial u_y}{\partial y} + \frac{\partial u_z}{\partial z} \tag{9}$$

Where $u_i$, is the displacement in the $i^{th}$ direction. The Laplacian operator, $\nabla^2$, takes on the familiar form,

$$\nabla^2 = \frac{\partial^2}{\partial x^2} + \frac{\partial^2}{\partial y^2} + \frac{\partial^2}{\partial z^2} \tag{10}$$

The application of the Helmholtz decomposition theorem can now be applied. As the functions are smoothly varying, they can be written as the sum of a curl-free and divergence-free vector field as noted in[17].

- The curl free component, often referred to as the dilatational wave, corresponds to the traditional compression or longitudinal wave encountered in liquid media. This wave is spatially symmetric.
- The divergence-free component often called the distortional wave, or shear wave is the antisymmetric solution.

As these waves have a differing spatial symmetry, it is often simplest to treat them completely separate from one another in a homogeneous medium, as changes in symmetry require an inhomogeneity to be introduced as will later be shown. As a result, it is common to write the shear and longitudinal components as,

$$\nabla^2 u_i - \frac{1}{c_T^2}\frac{\partial^2 u_i}{\partial t^2} = 0, \text{for } i = x, y, z \tag{11}$$

$$\frac{\partial \Delta}{\partial i} - \frac{1}{c_L^2}\frac{\partial^2 u_i}{\partial t^2} = 0, \text{for } i = x, y, z \tag{12}$$

Where the speed of sound for the longitudinal, $c_L$, and the transverse, $c_T$, wave is found in accordance with the relations,

$$c_L = \sqrt{\frac{\lambda + 2\mu}{\rho}} \tag{13}$$

$$c_T = \sqrt{\frac{\mu}{\rho}} \tag{14}$$

Differentiation of the wave equation can yield an alternative, more useful form of the wave equation for elastic media. By performing this arrangement, we can eliminate Δ between the two equations, yielding the two characteristic wave equations,

$$\nabla^2 u_i - \frac{1}{c_T^2}\frac{\partial^2 u_i}{\partial t^2} = 0, \text{for } i = x, y, z \tag{15}$$

$$\nabla^2 u_i - \frac{1}{c_L^2}\frac{\partial^2 u_i}{\partial t^2} = 0, \text{for } i = x, y, z$$

Showing that the waves both obey the characteristic wave equation. Despite this somewhat simplified form, the spatial parity of the wave should be noted, as it is not evident in this form of the equation. The derivation of sound waves can be done in a variety of ways, including lattice structures, field theories, and more, with books on these details being available [18]. The acoustic wave propagation can also be derived from the phonon propagation in quantum mechanics; however, the details of both treatments are outside the scope of this work, where we deal purely with the results of the wave equation itself.

### *3.3. Source Representation of Spatially Symmetric Waves*

The wave equations thus far describe the propagation of waves through a media but do not describe the source or detection of sound. In later chapters, we explore the physical generation of sound; however, a purely theoretical approach is undertaken here. In ultrasound, as in much of physics, the two bases most

commonly used are a spherical basis and a plane wave basis. In this section, we discuss the details of each representation based on standard approaches[14].

Without regard to the type of wave propagation, a wave is any mathematical construct that obeys the wave equation for either propagation form. The introduction of a source or sync term is given by the addition of a potential $f(r,t)$ to the equation, under which the modified equation becomes,

$$\nabla^2\psi - \frac{1}{c^2}\frac{\partial^2\psi}{\partial t^2} = f(r,t) \tag{16}$$

for longitudinal waves and

$$\frac{\partial\Delta}{\partial i} - \frac{1}{c_L^2}\frac{\partial^2 u_i}{\partial t^2} = f(r,t), \text{for } i = x, y, z \tag{17}$$

for shear waves. Here, we can note immediately that the shear wave solution can occur along any dimension, indicating 3 possible solutions. As these solutions are of the same form in an isotropic media, only one shall be considered here.

The introduction of a point source is often done by first re-writing the equation in the frequency domain through the application of the Fourier pairs,

$$f(t) = \frac{1}{2\pi}\int_{-\infty}^{\infty} f(\omega)e^{-i\omega t}d\omega \tag{18}$$

$$f(\omega) = \int_{-\infty}^{\infty} f(t)e^{-i\omega t}dt \tag{19}$$

under which, the Helmholtz equation is found for longitudinal waves,

$$[\nabla^2 + k^2(r)]\psi(\boldsymbol{r}, \omega) = f(\boldsymbol{r}, \omega) \tag{20}$$

where the wavenumber, $k(r)$, relates the frequency and propagation speed as,

$$k(r) = \frac{\omega}{c(r)} \tag{21}$$

The solution to such an equation can take two primary forms, that of a point source and that of a plane wave. For a plane wave, the propagation of the wave occurs in two directions outwards from the source as,

$$\psi(\boldsymbol{x}) = \begin{cases} Ae^{i\boldsymbol{k}\cdot\boldsymbol{x}} \\ Be^{-i\boldsymbol{k}\cdot\boldsymbol{x}} \end{cases} \tag{22}$$

whereas the point source takes the form of a radially symmetric equation,

$$\psi(r) = \begin{cases} \left(\frac{A}{r}\right) e^{ikr} \\ \left(\frac{B}{r}\right) e^{-ikr} \end{cases} \tag{23}$$

### *3.4. Spherical Basis*

For a spherical basis, we can define the radial displacement of the wave as,

$$u_r = \frac{\partial\psi(r,t)}{\partial r} \tag{24}$$

For a source, $u_r$, with an initial radius $a$, substitution into the Helmholtz equation yields a relationship between the source and frequency at the boundary $r = a$,

$$u_r(a) = U(\omega) \tag{25}$$

where $U(\omega)$ is the initial intensity for a frequency $\omega$. Under the assumption that the wave is a source, we are interested only in the wave solution that yields and outward propagation,

$$\psi(r) = A\frac{e^{ikr}}{r} \tag{26}$$

For which the displacement field is,

$$u_r(r) = A\, e^{ikr}\left(\frac{ik}{r} - \frac{1}{r^2}\right) \tag{27}$$

Under the assumption of a point source of sound, we assume that $ka \ll 1$, under which the simplification in the source term becomes,

$$u_r(\omega, a) = -\frac{A}{a^2} \tag{28}$$

which allows for the definition of the initial amplitude of the wave,

$$A = -u_r a^2 \tag{29}$$

It is common to normalize this factor to the surface area of the wavefront at $r = a$, defining the source strength $S_\omega = 4\pi a^2 u_r$, such that,

$$\psi(r) = -S_\omega \frac{e^{ikr}}{4\pi r} \tag{30}$$

### *3.5. Shear Wave Basis*

In the case of shear waves, it is best to use direct solutions to the wave equation in a spherical basis, mainly the spherical Bessel function of the first kind, $j_1$. In the case of shear waves, we note that the solution takes the form of,

$$j_1(x) = \frac{\sin(x)}{x^2} - \frac{\cos(x)}{x} \tag{31}$$

As the distance from the origin increases, we can note that the behaviour is of the same form of the longitudinal wave, where the higher-order terms are ignored, arriving at,

$$\phi(r) = -\frac{S_\omega e^{ikr+\frac{\pi}{2}}}{4\pi r} \tag{32}$$

In this way, we see that both the longitudinal wave and shear wave can be dealt with using a similar mathematical treatment, so long as the parity change is noted correctly.

### *3.6. Plane Wave Basis*

Although this work makes use of the spherical wave basis in many descriptions, some elements are better described using a plane-wave basis. In the plane wave basis, we can take the direct solutions that are widely known, mainly,

$$\psi(x) = \frac{A}{|r|^2} e^{i\boldsymbol{k}\cdot\boldsymbol{r}} \tag{33}$$

$$\phi(x) = Ae^{i\boldsymbol{kx}} \tag{34}$$

These plane waves form the basis of boundary interaction, with the reflection and transmission coefficients determined using these expressions. In imaging, plane waves are frequently used as a basis in simple media, as a mapping of many point sources can be expressed in plane wave notation through the radon transform.

### *3.7. Propagation in an Inhomogeneous Medium*

In an inhomogeneous medium, the Helmholtz equation must be modified. In a general description, the only values that are spatially dependent are the propagation speed, and conversely wavenumber, and the potential $f(r)$ such that,

$$[\nabla^2 + k(r)^2]\psi(r) = f(r) \tag{35}$$

and likewise for the case of shear waves. The transition between shear waves and longitudinal waves that occurs at a boundary, a phenomenon is known as mode conversion, shall be covered subsequently.

In general, the approach of Green's functions is employed in solving these equations. Green's functions assume that the wave equation is a combination of the homogeneous solution, $H_\omega$, plus a solution, $g_\omega$, such that,

$$G_\omega(r.r_0) = g_\omega(r, r_0) + H_\omega(r) \tag{36}$$

In this radial symmetric case, the second wave is described as a point source with an origin at the surface of the sphere, such that,

$$[\nabla^2 + k(r)^2]G_\omega(r.r_0) = \delta(r - r_0) \tag{37}$$

The solution of these equations is known formally as the Green's theorem for bounded surfaces and is described by[14]

$$\psi(r) = \int_s \left[ G_\omega(r, r_0) \frac{\partial \psi(r_0)}{\partial n_0} - \psi(r_0) \frac{\partial G_\omega(r, r_0)}{\partial n_0} \right] dS_0 - \int_v f(r_0) G_{\omega(r,r_0)dV_0} \tag{38}$$

Such solutions, known as Green's solution, form a simplistic model from which to work. Despite this form, it is important to note the two issues that arise from such a solution. The first is the fundamental point source assumption, which was derived only as a high-frequency approximation to the wave equation. The second mathematical issue is that both writing and solving such integrals in a closed-form solution is rarely possible. For this reason, it is common to employ numerical techniques, such as those discussed in the numerical methods section.

One of the fundamental theorems that can be derived from such solutions is that of Helmholtz reciprocity. This theorem states that the interchange of the source and destination in the Green's functional form leaves the solution unchanged. In this way, we can note that the inverse propagator is interchangeable with the forward propagator, a critical assumption in the field of imaging[19,20].

### *3.8. Reflection and Refraction*

At a surface between two media, the wave undergoes refraction into the second media and a reflection back into the first. One of the simplest derivations is through the analysis of the slowness surface of the material, shown in Figure 11. At the boundary between two media, the wave must be continuous, therefore requiring that the distance of propagation perpendicular to the surface of the boundary be constant between the reflected and refracted wave. This requirement, combined with the fact that the distance travelled is scaled by the sound speed immediately yields Snell's law through geometric relations,

$$\frac{\sin\theta}{\sin\theta'} = \frac{c}{c'} \tag{39}$$

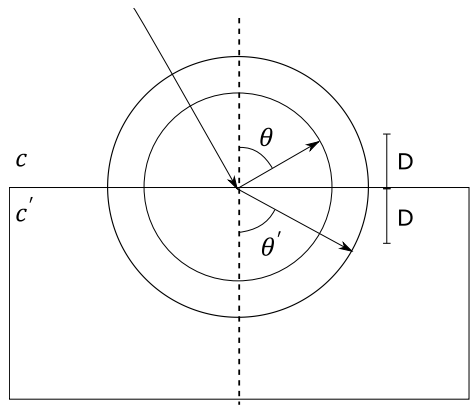


Figure 11 – A depiction of the acoustic slowness surface. As the rays reflect and refract, the continuity condition at the boundary requires that propagation in the vertical direction, $D$, be equal on either side of the boundary, yielding the relation of Snell's law.

In industrial acoustic imaging, the material in question often supports both longitudinal and transverse waves at differing sound speeds. In theory, this means that for either an incident shear or longitudinal wave on a planar boundary, $I_s, I_d$, we have a reflected shear, $R_s$, reflected longitudinal $R_d$, transmitted shear, $T_s$, and transmitted longitudinal, $T_d$, wave. Each of these waves has its own respective angle given in accordance with Snell's law, with all being related through the relation,

$$\frac{1}{c_d}\sin\theta_d = \frac{1}{c_S}\sin\theta_S = \frac{1}{c_S'}\sin\theta_S' = \frac{1}{c_d'}\sin\theta_d' \tag{40}$$

These angles, along with the respective directions of propagations, are labels in Figure 12. In addition, as the reflected and incident angle are equal, Snell's law need not be applied to solve for them.

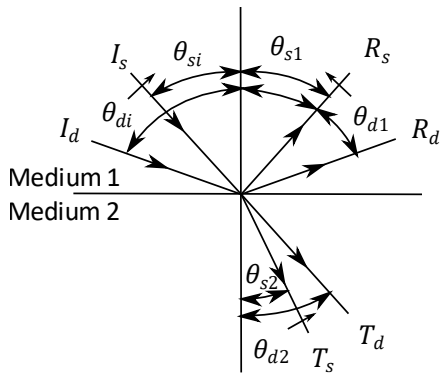


Figure 12 – A depiction of the varying wave propagation directions, after encountering a boundary. Smaller arrows are used in the case of shear waves to denote the displacement direction. Adapted from [18].

To determine the transmission and reflection coefficients, we consider the wave as continuous across the boundary. For an incident wave, this implies that both the position, stress, and intensity must be constant across the boundary. As reflection imaging is used in ultrasound, reciprocity allows for the use of the simplified intensity coefficients[19]. For each incident wave, a total of 4 coefficients can be found, corresponding to the transmitted shear, $T_s$, reflected shear, transmitted longitudinal and reflected longitudinal wave. These are related to the impedance of the material, $Z$, in accordance with,

$$Z_i = c_i \rho, \;\; i = s_1, s_2, d_1, d_2 \tag{41}$$

As a result, the intensity coefficients become a problem of solving the system,

$$A \begin{bmatrix} R_d \\ T_d \\ R_s \\ T_s \end{bmatrix} = B \tag{42}$$

where the matrix A is given by,

$$A = \begin{bmatrix} -\cos\theta_{d1} & -\cos\theta_{d2} & -\sin\theta_{s1} & \sin\theta_{s2} \\ -\sin\theta_{d1} & \sin\theta_{d2} & \cos\theta_{s1} & \cos\theta_{s2} \\ -Z_{d1}\cos 2\theta_{s1} & Z_{d2}\cos 2\theta_{s2} & -Z_{s1}\sin 2\theta_{s1} & -Z_{s2}\sin 2\theta_{s2} \\ -Z_{s1}\dfrac{c_{s1}}{c_{d1}}\sin 2\theta_{d1} & -Z_{s2}\dfrac{c_{s2}}{c_{d2}}\sin 2\theta_{d2} & Z_{s1}\cos 2\theta_{s1} & -Z_{s2}\cos 2\theta_{s2} \end{bmatrix} \quad (43)$$

and the matrix B takes the form based on the incident wave. For longitudinal incidence,

$$B = \begin{bmatrix} -\cos\theta_{di} \\ \cos\theta_{di} \\ Z_{d1}\cos 2\theta_{di} \\ -Z_{s1}\dfrac{c_{s1}}{c_{d1}}\sin 2\theta_{di} \end{bmatrix} \quad (44)$$

For incident Shear vertical waves, we have,

$$B = \begin{bmatrix} -\cos\theta_{si} \\ \cos\theta_{si} \\ Z_{s1}\cos 2\theta_{si} \\ -Z_{s1}\sin 2\theta_{si} \end{bmatrix} \quad (45)$$

We can now solve the system through the application of Cramer's rule or similar methods. In this work, the coefficients are implemented using a lookup table, with an approximate coefficient being looked up based on the given angle, rather than solving the transmission/reflection equation.

### *3.9. Diffraction*

In the case of plane and point sources, the source term is simple mathematically; however, in most cases, we lie somewhere in between these two wave modalities where diffraction effects apply. Diffraction effects are caused by sources of waves in this regime, either a physical source or the reflection of waves off of a limited size object, acting as a new source of sound.

The simplest case of diffraction is that of the single-slit diffraction pattern. In ultrasound, as the transmission sources, or elements, increase in size above that of half wavelength, the spatial emission pattern becomes that of the Fraunhofer diffraction formula. In this case, the source of wave, which has a finite width D, is broken into smaller, point source terms with even spacing across the slit.

These emitters have a constant phase with respect to each other, resulting in the characteristic angular pattern derived by Fraunhofer,

$$I(\theta) = I_0 \operatorname{sinc}^2\left(\frac{D\pi}{\lambda}\sin(\theta)\right) \tag{46}$$

where the intensity, $I$, is given as a function of angle from the center, $\theta$, and the initial intensity $I_0$. As will be discussed in the imaging section of this work, ultrasound transducers tend to use elements that are not true point sources, meaning that such directivity plays a key role in the imaging process.

In general, we need not limit ourselves to a line of emission, where the solution takes on a simple expression, with numerical methods being used to describe more generic diffraction patters. Diffraction techniques apply to these same cases, where the interference pattern results in regions with both high and low intensity depending on the refracting media.

### *3.10. Resonance*

The resonant effect can occur between any two objects that are spaced at a distance in continuous waves; however, in pulsed waves, these are limited to spacing near the wavelength of the sound. This resonance results in constructive

interference that increases or decreases the intensity of the wave in a spatial region. In imaging, this effect may eventually prove useful through an iterative reconstruction process[21].

### *3.11. Attenuation*

In many systems, it is common to analyze the system in the absence of losses; however, such cases are seldom realized in nature. In ultrasound, these losses are grouped together as attenuation, describing losses that are not accounted for in the chosen model of sound propagation. These losses occur due to both elastic and inelastic scattering within the media. In general, elastic scattering accounts for the majority of loses in ultrasound wave propagation.

Elastic scattering comes in a variety of forms, one of which is Rayleigh scattering. In this scattering regime, the size of the scattering material is much smaller than the wavelength of the material. Rayleigh, in his work, noted that this results in a frequency-dependent attenuation proportional to $\lambda^{-4}$ [22]. This scattering regime acts primarily as a filter to the frequency content of a wave spectrum, mainly, applying a linear transform that acts to reduce high-frequency content in a waveform.

In addition to this scattering, incoherent scattering plays a critical role in the loss of wave energy. This scattering results from scattering off structures that are not accounted for in the sound propagation model. In general, a homogeneous medium is assumed for imaging; however, the material is often better approximated as a sum of gain structures with distinct boundaries that result in incoherent scattering. These boundaries separate material of slightly varying

density and sound speed, resulting in scattering from each boundary. This scattering, seen in Figure 13, results in the generation of noise within a sample due to the scattering effects.

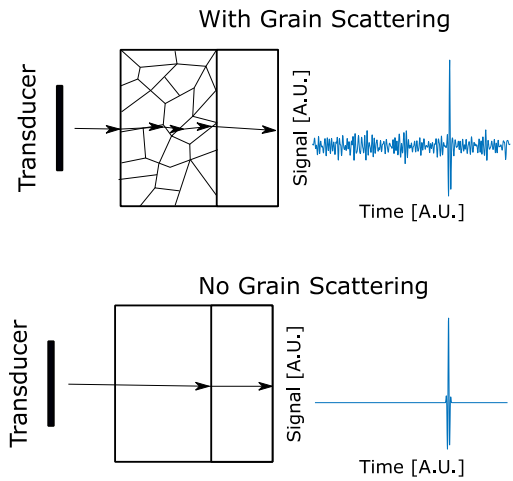


Figure 13 – An example of Incoherent scattering, where the reflections are small, overlapping and do not contain a clear signature. This scattering results in a lossy propagation, which is often grouped in with other attenuation.

### *3.12. Dispersion*

Sound propagation, in many cases, is assumed to be non-dispersive. Dispersion is a measure of the frequency dependence of the speed of sound. In general, as the frequency of the wave increases, its speed of propagation also increases. For a pulsed wave, such as those often used in acoustic measurements, this results in a frequency phase dependence on the propagation. In a dispersive medium, the lower frequencies are delayed, resulting in a broadening of the pulse tail as the wave propagates. This phenomenon is visually depicted in Figure 14, where the asymmetric Gaussian envelope obtains a tailing effect due to propagation.

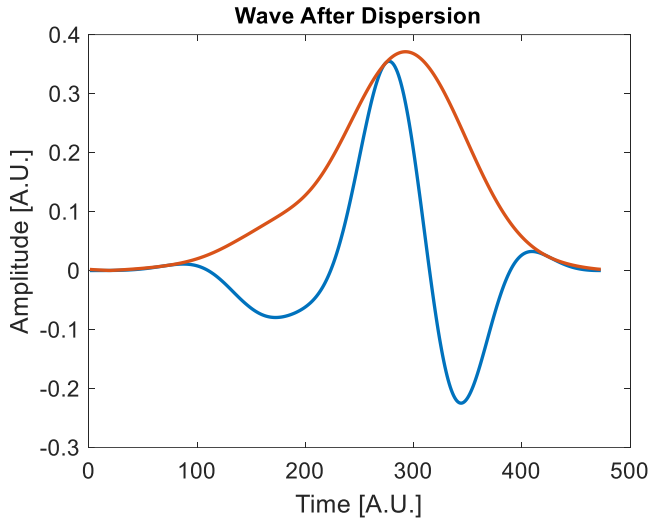


Figure 14 – A dispersive media results in a broadening of the wave pulse. Dispersive effects are often ignored from a theoretical perspective but do play a factor in the resolution limit of the system.

# Chapter 4

# Ultrasound Modelling

The homogeneous wave equation has known, analytic solutions; however, the homogenous wave equation, even ignoring dispersion and attenuation, can rarely be solved using analytic methods. In order to solve such problems, we must instead rely on numerical methods of wave modelling. These methods take many forms, but for the most part, involve solving the wave equation, or an approximation to it, using computational methods.

In this work, we look at two solutions to the wave equation, one using available toolkits that rely on the finite difference pseudospectral models[23–25] and another that relies on the ray-based models. Both models take a different approach to the wave equation, with the finite difference model often resulting in higher accuracy at the cost of computational efficiency. More models were reviewed and are available[14]; however, the discussion of most are outside the scope of this work. In this work, the finite difference model was used for more robust simulations, where the full effects of wave phenomena needed to be considered. The ray model was chosen as an approach to allow for high-speed reconstruction, where simulation time is the most critical factor. In this section, we discuss the implementation of both models.

The spectral model code makes use of the k-wave toolbox, with only the development of the necessary setup code performed as part of this work. In the

case of the ray model, the code was developed completely from scratch, using only the theoretical applications, which were developed previously[26–28].

### *4.1. Pseudospectra Model of the Wave Equation*

Finite difference models represent a physical medium as a discrete set of points, or a grid for which the specific properties of the medium are known. This grid can, in general, be of any form; however, the most common are square or rectangular grids.

On a rectangular grid, the wavefunction defines a spatial gradient, for which a derivative must be found. This derivative can be done using a variety of models, including finite difference, central difference, or in the case of spectral models, Fourier series, to express the spatial derivative, as seen in Figure 15[29]. In cases where the wave is broadband in nature, the functional form may span an extensive range of points simultaneously, making methods that use a larger series more accurate in the modelling process. In the spectral model, this series is expanded globally through the computation of the Fourier transform. Using numerically optimized transforms, the use of global methods can be faster than an expansion involving a large number of terms, making the spectral model viable when broadband signals are considered.

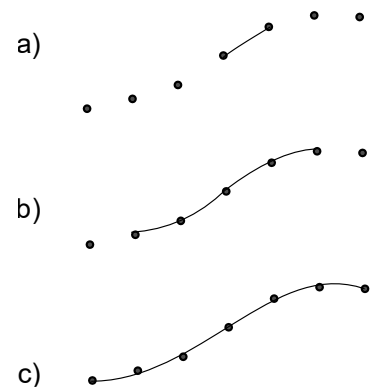


Figure 15 – An example of the differing methods for computing a spatial derivative of multiple points spanning the grid defined by j. Both finite difference, a), and central difference, b), models offer advantages when the difference is localized; however, in the case where a broadband wave is modelled, the computation of a large number of terms makes the spectral model c), more efficient. Adapted from [29]

In addition to the spatial derivative, the time evolution of the wave must be solved. This poses some issues, in that the same expansion cannot be applied. In the case of the simulations used in this work, the spectral model makes use of a central difference time step, employing the relation between the Fourier transform and its derivative (or simply the sin and cos relations) [29],

$$\mathcal{F}\left\{\frac{\partial}{\partial x}f(x)\right\} = ik_x\mathcal{F}\left\{\frac{\partial}{\partial x}f(x)\right\} \tag{47}$$

This step poses a potential problem, in that a fine time step is needed for the numerical stability of the model. The k-space method employed by the model attempts to relax this constriction; however, the operator used in this method relies on a low variance between the properties of the spatial grid. As a result, this parameter will not be covered here, as the benefit was not realized in most performed simulations.

In order to make use of the model, the definition of an input term, or source, medium, sensor and the computational grid is performed. Based on sample code, a number of simulation environments have been realized in this work, including both shear and longitudinal models for a wide variety of part geometries. In each case, the performance of the model has been verified using the standard method of reducing time steps and grid spacing until error is minimal.

### *4.2. Ray Methods Solution to the Wave Equation*

Ray methods are one of the most common solutions to the wave equation used in the field of physics. Ray methods make use of a generalized coordinate space to simplify the solutions to the wave equation. The derivation covered here can be found more in depth than covered here[14], with only the notable results making it to this section. Ray theory allows for a numerical solution to the wave equation that can be orders of magnitude faster than other methods as a result.

Mathematically, ray methods are derived from the Helmholtz equation, making the mathematical approximation of an asymptotic expansion that takes the form[14],

$$p(x) = e^{i\omega\tau(x)} \sum_{j=0}^{\infty} \frac{A_j(x)}{(i\omega)^j} \tag{48}$$

where $\omega$ is the frequency of the wave, $\tau$, its propagation length, $A_j$, its initial amplitude for the $j^{th}$ power. By taking derivatives of this equation, and substituting into the Helmholtz equation, we obtain an expression,

$$\nabla^2 p = e^{i\omega r}\left\{[-\omega^2|\nabla\tau|^2 + i\omega\nabla^2\tau]\sum_{j=0}^{\infty}\frac{A_j}{(i\omega)^j} + 2i\omega\nabla\tau\cdot\sum_{j=0}^{\infty}\frac{A_j}{(i\omega)^j} + \sum_{j=0}^{\infty}\frac{\nabla^2 A_j}{(i\omega)^j}\right\} \quad (49)$$

which, when ordered in terms of powers of frequency yields,

$$\begin{array}{cc} O(\omega^2) & |\nabla\tau|^2 = c^{-2}(x) \\ O(\omega) & 2\nabla\tau\cdot\nabla A_0 + (\nabla^2\tau)A_0 = 0 \\ O\left(\omega^{1-j}\right) & 2\nabla\tau\cdot\nabla A_j + (\nabla^2\tau)A_j = -\nabla\text{^}2\, A_{j-1} \quad j = 1,2,\ldots \end{array} \quad (50)$$

where the first term is known as the eikon equations and the second term the Boltzmann transport equation. As the series is divergent, it is common to ignore higher-order terms, as these result in larger errors. The most important note of the ray series is that it is assumed a high-frequency approximation or small wavelength approximation, as noted by the ordering of terms by frequency. Ray methods, which use the ray series, work best in situations when the boundaries present in a material vary slowly with respect to the wavelength as a result of this.

These two solutions define a common coordinate system, as seen in Figure 16, where the path that the ray takes, $\tau$, is related to its amplitude or divergence through the divergence as a function of $\tau$.

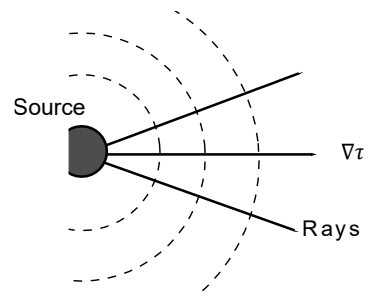


Figure 16 – A conceptual 2D representation of ray theory. The rays visually present the path along which the wave propagates through a medium. Adapted from [14].

### *4.2.1. Solutions to the Eikonal Equations*

The solutions to the Eikonal equation are derived by looking at the path or trajectory the wave follows. Since the trajectory, $\nabla\tau$, is perpendicular to the waveforms, the trajectory of the ray can be defined using the differential equation,

$$\frac{dx}{ds} = c\nabla\tau \tag{51}$$

Where $s$ is a generalized distance. As the eikon equation is defined by the relation between the path and sound speed, we see that the differential term $dx/ds$ is unity. In this regard, the parameter $s$ is simply the arc length of the ray. In the waveform, this propagation length simply corresponds to the phase associated with its travel. To solve the eikon equation, the common approach is to perform a transform into the coordinate system of the ray, under which the travel time becomes given by the path integral,

$$\tau(s) = \tau(0) + \int_0^s \frac{1}{c(s')} ds' \tag{52}$$

such that the phase of the wave is delayed in accordance with its travel time. The equation can now be arranged. Using the fact that in the ray's coordinate system $|dx(s)/ds|^2 = 1$, we can express our equation in the form of a variational principle,

$$S\{y\} = \int_{x_0}^{x_1} L(y, y', x)dx \tag{53}$$

which is minimized in the Euler Lagrange equation,

$$\frac{\partial L}{\partial y} - \frac{d}{dx}\left(\frac{\partial L}{\partial y'}\right) = 0 \tag{54}$$

which results in stationary travel time in accordance with the equation of motion,

$$\frac{d}{ds}\left(\frac{1}{c}\left(\frac{dx}{ds}\right)\right) + \frac{1}{c^2}\frac{\partial c}{\partial x} = 0 \tag{55}$$

This method, known often as Fermat's principle, is one of the most used methods in phased-array imaging, stating simply that the solutions to the equations are ones that result in highly constructive interference (as the phase change between neighbouring rays is zero). This form of the equation can be solved to yield other relations, including Snell's law.

#### *4.2.2. Boltzmann Transport Equations*

The second term in the expansion is known as the Boltzmann transport equations. This term is often written in the more familiar form,

$$\nabla \cdot (A_0^2 \nabla \tau) = 0 \tag{56}$$

We can then remark that gauss' divergence theorem relates the integral over the divergence of F to the divergence at the surface,

$$\int_V \nabla \cdot F dV = \int_{\partial V} F \cdot \boldsymbol{n} dS \tag{57}$$

From this, we obtain the equation,

$$\int_{\partial V} A_0^2 \nabla \tau \cdot \boldsymbol{n} dS \tag{58}$$

From this, we arrive at the familiar expanding surface as in the point source case, where energy is conserved across the surface. In ray theory, this gives each ray a converging or diverging surface normal to it. These rays form a set of surfaces, such that the directional derivative $\nabla \tau \cdot \boldsymbol{n} = 1/c$ is satisfied. This results in the Boltzmann transport equation,

$$\int_{\partial V_0} \frac{A_0^2}{c} dS = \int_{\partial V_1} \frac{A_0^2}{c} dS = const \tag{59}$$

where the partial volume represented by the integral is the region encapsulated by the rays. From this equation, we can understand that the region between neighbouring rays is of a fixed total amplitude and related to the divergence of the rays,

$$A_0(s) = A_0(0) \sqrt{\left| \frac{c(s)}{c(0)} \frac{J(0)}{J(s)} \right|} \tag{60}$$

where $J$ is the Jacobian, whose determinant specifies the ratio of differential volume elements.

In this formulation, we have created a system of field equations that originate from a source of sound in space. The field equations we have derived, however, suffer from the same limitation of the green's functional form previously derived. When the divergence of the rays becomes zero, the amplitude according to the field equations approaches infinity. When deriving green's functions, we noted that the point source approximation holds only for $ka \ll 1$, meaning that the field equations must be changed to account for this. The most common method of doing so is to apply an empirically derived convergence limit to the field, such that regions where the convergence increases beyond the limit of $ka$ are re-normalized to prevent an unphysical result. The empirical limit is often enforced such that the beam width is limited to $\pi\lambda$[30].

#### *4.2.3. Ray Model*

With the equations of rays defined by the acoustic path length and divergence of the rays, we must implement a mathematical model for the equations that suits numerical techniques. The formulation of the ray model assumed each ray has a field around it based on the distance from its center to neighbouring rays. The amplitude is scaled in accordance with the initial amplitude and a phase component as,

$$P^{beam}(s,n) = A^{beam}(s)\phi(s,n)e^{i\omega\tau(s)} \tag{61}$$

Although any functional form can be employed, the most common forms are that of the triangle and gaussian functions defined with respect to neighbouring rays, such that the rays form a uniform field in space. In this work, we make use of

Gaussian beams, which are shown to be smoother spatially[14]. The gaussian equations take the form,

$$\phi(s,n) = e^{-\left(\frac{n}{W(s)}\right)^2} \tag{62}$$

In all cases, the width of the ray, $W(s)$, is determined in accordance with its amplitude at the specified path length,

$$W(s) = |q(s)\delta\theta_0| \tag{63}$$

where $\delta\theta_0$ is the angular spacing between rays. In the case of Gaussian beams, the amplitude is scaled in accordance with the fact that overlapping Gaussian functions result in a total area over unity, as such,

$$A^{beam}(s) = \frac{1}{(2\pi)^{\frac{1}{4}}}\sqrt{\frac{\delta\theta_0}{r}\frac{c(s)}{c(0)}\frac{2\cos\theta_0}{W(s)}} \tag{64}$$

In some models, it is common to launch initial rays with fixed spacing. In the model employed in this work, however, the rays are specified as a set of rays that intersect with a discretized set of spatial points corresponding to a boundary, as seen in Figure 17. This makes some computations easier; however, as the ray spacing is no longer uniform, two Gaussians must be employed for proper modelling, making the rays asymmetric.

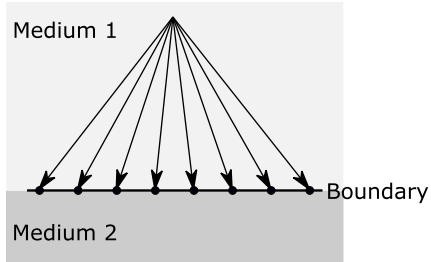


Figure 17 – A depiction of the rays propagating from a source to the evenly spaced points along a boundary. These initial rays form the basis of secondary rays in the new media.

At the boundary, the angle of each ray changes in accordance with Snell's law. This was accounted for using the vector form of Snell's law[31], which is much more practical for ray tracing techniques, where the direction of the propagating rays is of concern.

$$\hat{s}_2 = \frac{c_2}{c_1}\left[\widehat{N} \times \left(-\widehat{N} \times \hat{s}_1\right)\right] - \widehat{N}\sqrt{1 - \left(\frac{c_2}{c_1}\right)^2 \left(\widehat{N} \times \hat{s}_1\right) \cdot \left(\widehat{N} \times \hat{s}_1\right)} \tag{65}$$

Here, the new refracted ray, $\hat{s}_2$, is related to the change in the sound speeds, $c_1, c_2$ and the incident wave direction, $s_1$, with respect to the surface normal, $\widehat{N}$. This change yields a new set of rays propagating in the second media with new angles. In order to simulate the wave after the boundary, the physical rays, indicated by solid lines in Figure 18, are used to compute a new ray, indicated by the dotted line. By tracing the physical rays back to an origin, the distance of propagation of the new ray can be related to its divergence through the angular spread of the beam in either direction.

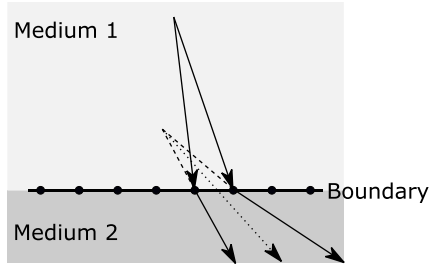


Figure 18 – A depiction of how a new ray is computed at the boundary. By tracing an origin using the two transmitting rays, a new direction and divergence of the ray can be formed in the secondary media.

To compute the initial amplitude of this ray, the amplitude at the boundary is determined using the arc angle of the field incident on the boundary, under the assumption that the source is normalized to a total radius of $2\pi$. This amplitude is then scaled by the reflection coefficient at the point of intersection between the new ray and the boundary.

With the second-order term computed, the first-order term is then determined. The time of flight can be expressed in a number of ways. In this work, the recasting of the rays to a new origin was extended by computing an originating time of the new set of rays. This time is computed such that the second medium is considered to be the sole propagator.

With the above performed, a computation grid must be specified. This grid is chosen to be after the boundary, with each point specified using a $x, z$ space in the form $x + iz$. For each point in the grid, the computation is performed in a similar manner, so a single term is outlined here.

For each ray, the contribution of the ray incident on the pixel is determined, taking into account the amplitude as a function of arc angle, such that the full

width half maximum is defined as a function of the angle between the original and new rays. This arc angle is converted to a beam width using the distance from the origin, with any amplitude falling below the empirical renormalization width being set to this factor. Finally, these rays are scaled with respect to the original amplitude. This yielded, for each point, a set of corresponding amplitudes. The phase of the ray is then computed with respect to the origin for each ray based on its sound speed, the distance of travel and the original phase factor.

In this work, the use of pulsed waves was employed. In order to correct the pulse shape, two approaches can be taken. In the case of a highly dispersive media, an optimal solution would involve recalculating the previous phase and amplitude factor (whose renormalization depends on the wavelength in the medium) for each frequency component in the pulse. The modified approach, used here, makes the assumption that the field term and phase term can be modelled after the central frequency, taking into account the pulse shape only in the time domain.

In both cases, each ray produces a time-varying signal with a unique amplitude, offset and in the case of dispersion, pulse shape. The summation of these signals produces a unique signature for the propagation between the source and destination.

Although the signature produced by such a summation represents the actual signal, in most cases, the signal is not used in imaging. As will be discussed in

the next section, the impulse response function for such a signal contains adequate information to reconstruct the signal in question. In pulsed imaging, this can be taken one step further by instead considering what will be termed the equivalent response function. This function aims to emulate the regions of high intensity within a resulting signal using Fermat's principle.

By determining regions of stationary phase within the signal points where maximal constructive interference occurs can be found. By extracting the phase for these signals, the amplitude can be computed by approximating the signal as a temporally enveloped signal around these stationary phase points, with the signal decay based on the pulse envelope. When this is done for all stationary points, the production of the equivalent response function occurs. The equivalent response function mirrors the amplitude of the original; however, the pulse broadening caused by the varying paths is not accounted for. The variation between these terms, along with an example pulse, is seen in Figure 19 for an arbitrary boundary, origin and destination.

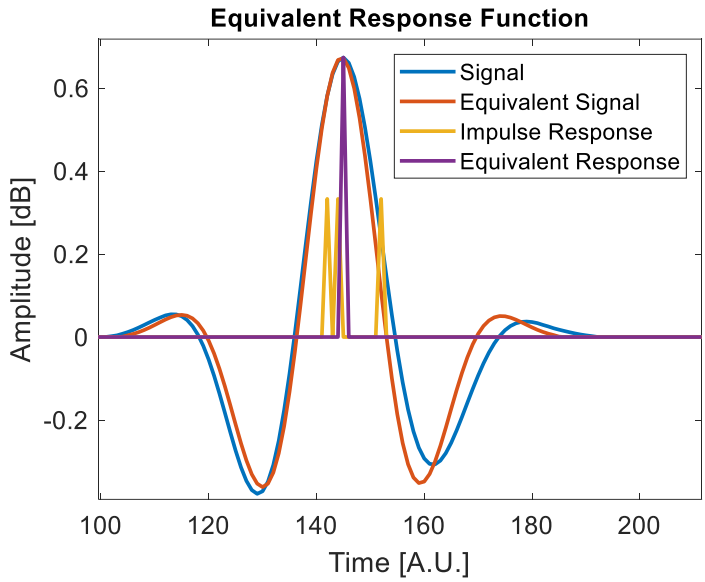


Figure 19 – A depiction of the equivalent response function. The various transmissions through a boundary in the impulse response function are often indistinguishable due to the resolution limits of the ultrasound transducer. In these cases, an equivalent response function can be used, introducing only a slight error in the wave tail from ignoring the frequency dependence of the interference.

In this work, the final approximation is to take the amplitude and time of the equivalent response function, rather than use the true response function. This approximation only applies in cases where one or more path is a stationary state solution. This term is selected based on the amplitude of the rays for computational efficiency, with the assumption that the greatest amplitude ray will correspond to the maximal amplitude of the equivalent response function.

# Chapter 5

## Imaging Theory

Imaging is defined as the effort of creating an accurate physical representation of an object based on a series of measurements. The system that makes these physical measurements, combined with the techniques that are used to process them, are grouped into what is known as the imaging system. In this section, we discuss imaging theory at its most basic level in terms of ultrasound imaging. The theory in this chapter, of course, has a much wider range of applicability due to the similar projective theory being used in x-ray CT imaging[32]; however, the subtleties are not explored here.

In ultrasound, the imaging system is often expressed as a series of emitters and receivers that form a spatial basis inside which a measurement can occur. If we define a basis in a purely spatial context, we can define a point in this basis, $\boldsymbol{x}$, using bra-ket notation[33,34]. Mainly, we can define an input point in our system,

$$|\boldsymbol{x}\rangle \tag{66}$$

termed the ket, this input has a dual termed the bra and presented as,

$$\langle\boldsymbol{x}| \tag{67}$$

and corresponding to a measurement point. Together, these form the expression of any spatial measurement. In imaging, we often use an infinite series of such points to form spatial basis, where all possible positions within the system form the basis on which our image shall be formed.

### *5.1. Coupled Basis and Wave Propagation*

In ultrasound, we work not with a spatial basis, but a coupled space-time basis. This basis is presented using a slight modification to the previous notation, mainly, we specify a point in space, at a point in time, $t$, by writing,

$$|\boldsymbol{x}, t\rangle \tag{68}$$

with a complete basis spanning all of space and time. In ultrasound, we can conceptualize a measurement in this basis as a Dirac delta measurement of some property at a specific point in space-time. If we define our temporal origin at $t_0$, we can specify a later point in time, $t$, using the notation,

$$|\boldsymbol{x}, \mathrm{t}_0; t + t_0\rangle \tag{69}$$

In order to transition between two times, we can also specify a unitary operator, $U_t$, as the time evolution operator. The time evolution of an input is defined with respect to the system through which it propagates and can be solved using analytic or numeric techniques depending on the complexity of the medium. From this, we can write,

$$U_t|\boldsymbol{x}, 0\rangle = |\boldsymbol{x}, 0; t\rangle \tag{70}$$

In this work, we assume that the system and any measure of it do not change with respect to time, mainly, the system is time-invariant over the period during which the image is formed. Using the above notation, we shall denote a source as localized at its temporal and spatial origin; however, this is not in general true of a later time. As the goal of the imaging process is to describe a spatial measurement, and we consider such a measurement time-invariant, any

localized, non-time evolved source at this point in space is suitable to form such a measurement. As an example, we can consider the following three measurements of some time independent observable, $O$, at a point, $\boldsymbol{x}$, to be equivalent,

$$\langle x|O|x\rangle = \langle x,0|O|x,0\rangle = \langle x,t|O|x,t\rangle \tag{71}$$

### *5.2. Inverse Imaging and Time Reversal*

The goal of imaging can thusly be presented as finding an equivalent way of representing the spatial basis using a set of space time points. In ultrasound, this is done through an inverse approach. Inverse methods were primarily established in Mathias Fink's work [35–38] as a solution to the focusing problem. In this work, we make use of the ray series expansion to present the results in a simplified manner. In ultrasound imaging, we wish to measure a local point using a delocalized measurement. In our space-time model, we can present such a problem as,

$$\sum_n a_n|x_n,t_n;t\rangle = |x,t\rangle \tag{72}$$

Mainly, we wish to find a set of delocalized emitters and receivers at fixed points in space and time that form an equivalent localized spatial measurement at a later point time. By properly selecting this series of points, it is possible to reconstruct every point in the system, allowing the set of points to form a spatial basis upon which imaging can occur.

The simplest example of an inverse solution can be found in acoustic microscopy. Although the forward solution yields the desired problem, it is far easier to use Helmholtz reciprocity and consider the inverse problem, mainly, we wish to find the time evolution of a point source,

$$U|x,0\rangle = \sum_n a_n |x_n, t_n\rangle \tag{73}$$

Where the amplitude coefficients are chosen to correspond to a specific point in space and time. In a homogeneous medium, we can consider a constant time solution of a circular or spherical shell. When this is done, under time reversal, the enclosing shell can be used to perfectly represent one such point in space. We often approximate this measurement with only a portion of the complete shell, allowing for imaging to occur through a rasterization of the transducer or imaged part.

In phased array imaging, we allow for a variable time solution. Using the same equation, we can choose an arbitrary enclosing surface and follow the same procedure. In a homogeneous medium, we expect the time and amplitude coefficients to be based on their distance from the source, as seen in Figure 20, rather than a constant as in the previous case. Phased array has the distinct advantage in that, by choosing a set of points that completely encloses the system, varying amplitude and time combinations can be used to represent any spatial point within the system, allowing for a phased array transducer to form a complete basis in theory. Despite this, we are often limited in the sampling

process to a partially enclosing shell by constraints of accessibility, meaning that such a process only approximately holds.

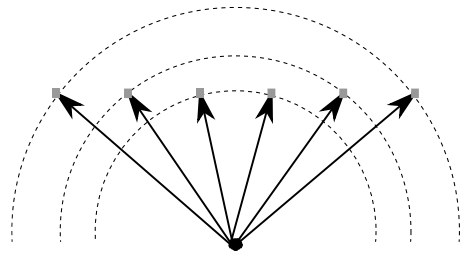

Figure 20 – A depiction of a series of sources located along a line. As the wave propagates outward from a point source, the intersection of the wavefronts with the points determines the phase offset and amplitude of the inverse problem.

In an inhomogeneous medium, the situation becomes notably more complicated. As a wave can echo inside the sample, each point is expected to record not a singular time, but a series of time points, or a signal. In theory, this signal may be infinitely long, but the amplitude shall often decay such that the summation over a finite time period can be used to approximately reconstruct our original point source. Mathematically, we can express such a process as,

$$|x, t\rangle = U \sum_{n,m} a_{nm} |x_n, t_m\rangle \tag{74}$$

Such a process is further limited by the fact that the energy may not be in the same form as the originating source, as mode conversion may occur. If the sampling medium supports more than one wave modality, the summation of all modalities must be used to form a basis. Furthermore, as energy is lost to other forms through attenuation, and the propagation process is only approximated as linear, we rarely expect our sampling set to form a complete basis. As such, the

topics discussed from here on should be taken as an approximate form of the solution.

Rather than make use of a transmission delay corresponding to each spatial point, it is also possible to measure the temporal signal from each emitter as a function of time at each receiving point that forms this basis. This data, known as full matrix capture (FMC) data, is used in this work to accelerate the imaging process. Once this data is collected, selecting samples that correspond to those desired for spatial focusing can chosen to reconstruct the image in post-process, allowing for analysis of the data using a variety of focal techniques. Such a process also allows for a digital rescaling of the amplitudes, whereas the use of true phased array techniques require complicated electronics to emit arbitrary signals.

### *5.3. Simplifications to the Imaging Process*

The first simplification used in this work is the same as in most imaging processes. Although exact solutions presented in the previous chapter are idealized, we seldom have complete knowledge of the propagation medium or the tools to solve for arbitrary wave propagation through the medium. To overcome this, we work in the interaction picture, whereby we assume that the propagator of our system is of an approximate form $U_0$. To this propagator, we add a perturbation, $U_V$ such that the complete propagator takes the form,

$$U = U_0 + U_V \tag{75}$$

When this is performed, we see that any input based on the idealized form will ignore the interactions between this idealized form and the perturbations in the system. This can result in the presence of reverberations when these interactions are not accounted for within the image formation process. In this work, we make use of an iterative approach, where the coupling medium is used to form an initial image and the time evolution of the system updated based on the boundary detected and the physical properties of the brazed joint and coupling medium.

The second approximation used in this work is formulated based on the ray series expansion and the equivalent response function. If one considers a setup as shown in Figure 21, a wave packet can be propagated from this origin to the destination through the given boundary using the ray series expansion.

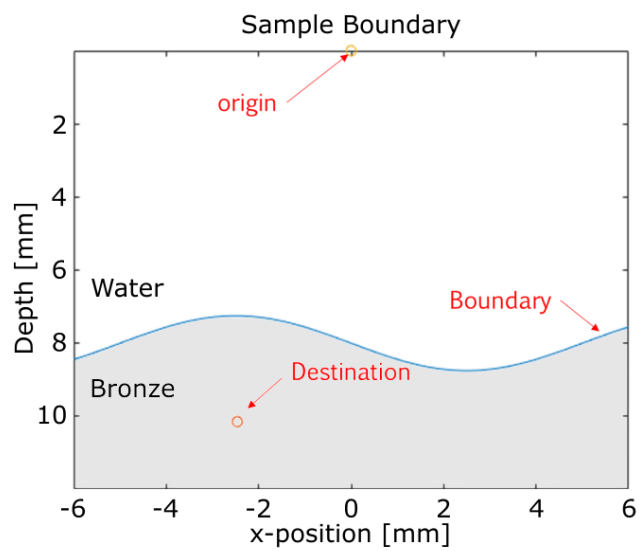


Figure 21 – A depiction of the setup that can be solved using numerical techniques. Here, a source and destination point are selected, separated by a boundary between two materials. By tracing the rays through the boundary, from the source to the destination, an approximation of the propagation signal can be solved.

Mainly, if we consider the simulation process as shown in Figure 22, the process of imaging can be drastically simplified. By considering the time of flight of each possible path between the origin and destination through the boundary in question, the wave packet can be convolved with time-delayed Dirac impulses to achieve a path representation. Here, we can note that about the stationary point, corresponding to Fermat's principle, constructive interference occurs. When this representation is scaled by its corresponding amplitude, forming an amplitude path representation, many paths in the propagation are found to have no significant amplitude present at the point in question. Summation along these paths forms a propagation signature that confirms that only a single dominant solution is present. By using an approximate deconvolution of such a signal, a single dominant solution can be used as the equivalent response function.

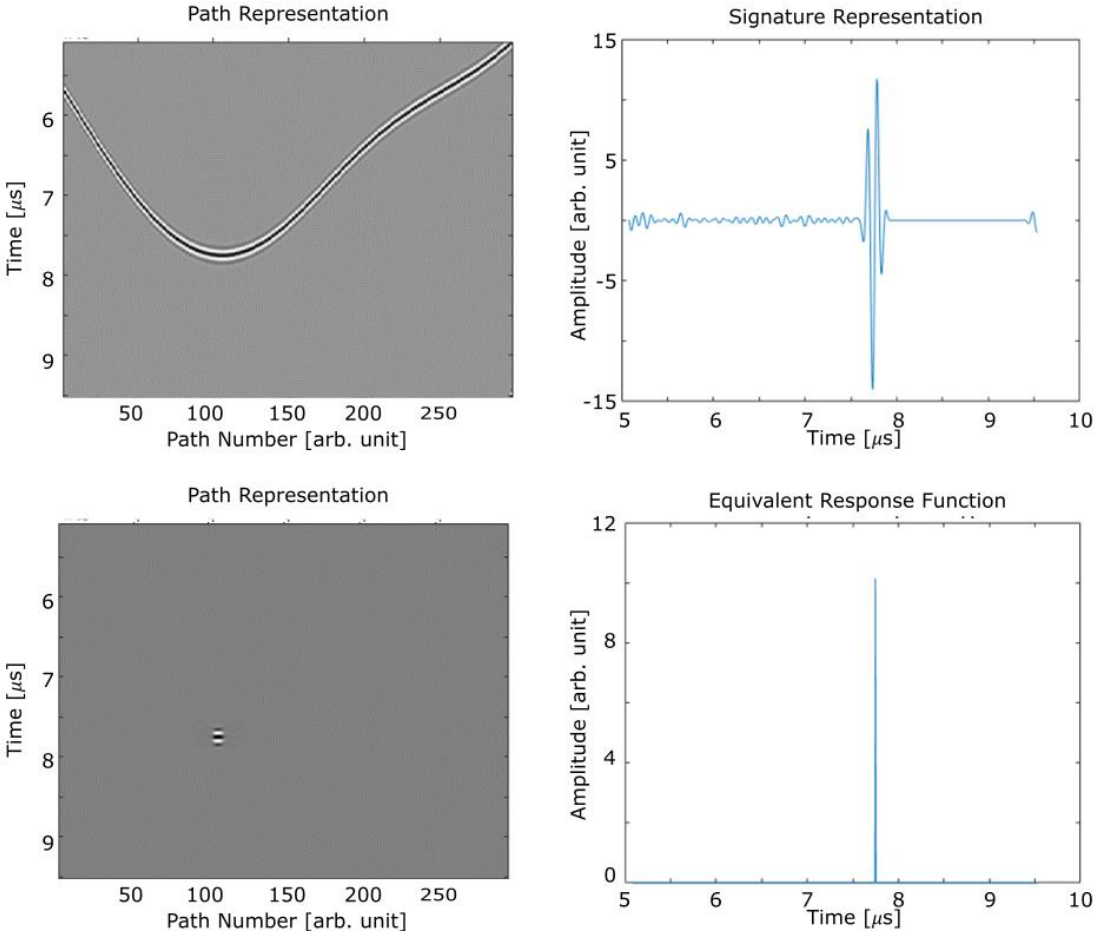


Figure 22 – A depiction of the various steps in ray tracing. Here, we consider the delay introduced by each path (upper left) to form a path image. Scaling by amplitude results in only a few dominant paths in many cases (bottom left). These paths each contribute to a signature (top right) that can be approximated with an equivalent response function (bottom right) based on the dominant path.

Under this assumption, mainly of dominant paths, the infinite time signal proposed in the theory of time-reversal can be approximated to a good degree by only a limited number of pulses in most cases. We further approximate this to a single dominant solution, making the image formation process a delay, sum and multiply technique that can be achieved in hardware with relative ease.

With these approximations stated, we can now formulate the image formation process in its entirety. For the measurement of a single point, we may substitute this with our indirect basis in the form of,

$$\langle x|O|x\rangle \approx \frac{1}{A_{tot}} \sum_{n'} \sum_{n} a_n a_{n'} \langle x_{n'}, t_0 + t_{n'} + t_n | UOU | x_n, t_0 \rangle \tag{76}$$

Where the amplitude coefficients and time shifts are chosen to correspond to these maximal paths between origin and point of convergence, and the point of convergence and reception points. The total amplitude is a correction factor introduced to account for the incomplete sampling by scaling the image with respect to the total amplitude incident on each pixel, $A_{tot}$, in accordance with,

$$A_{tot} = \sum_{n'} \sum_{n} a_n a_{n'} \tag{77}$$

The final step in the image formation process is to set pixels whose total amplitude falls below a minimum threshold to zero. This is done when the value of $A_{tot}$ drops below 5% of the maximum, corresponding to a poorly sampled pixel. If this is not done, additional artifacts result as the amplitude normalization factor approaches zero. The final approximation used in this work is that of half matrix capture, where Helmholtz reciprocity used to decrease the computational overhead. The total image formation process can, therefore, be broken into the flow chart in Figure 23.

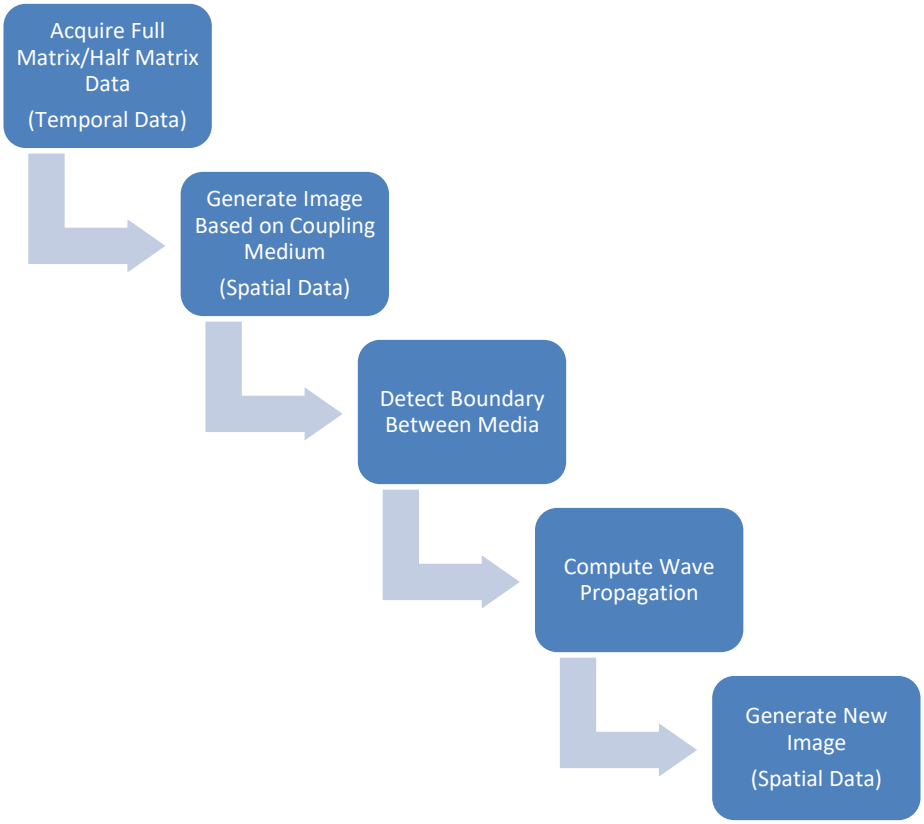


Figure 23 – A flow diagram depicting the image formation process. By collecting raw temporal data, we first perform the spatial remapping based on the properties of the coupling media. Using the formed image, a boundary between the sample and coupling medium is determined and the wave propagation model updated based on this. The final step is to perform as secondary spatial remapping to form a focused image.

### *5.4. Comparison with Current Imaging Techniques*

Although it is not possible to compare to all techniques, as much of the equipment available from manufacturers implement proprietary algorithms for focusing, it is possible to compare to the literature available. From their early work on the total focusing method (TFM), Drinkwater's group has published multiple reviews of the TFM and FMC techniques and comparisons to traditional phased array approaches[40–45], which themselves are based on synthetic

aperture approaches[46]. As the propagator, and its interaction with the observable is often termed as a scattering process, the work is done on the identification of the defect based on its scattering matrix also has potential applicability to future work in the characterization of defects[47–57].

The closest comparison to the proposed technique found in literature was done for the case of a homogeneous medium, where a scaling factor based on the beam profile was proposed[58][58]. This profile-based correction does work out to the same correction proposed in this work; however, in an inhomogeneous medium the addition of the boundary conditions, and the possibility of multipath solutions must be accounted for. Additional corrections based on the ray methods has been done in the case of a flat boundary[59]; however, as a flat boundary results in divergent rays, the numerical implementation and results found there would not be valid in much of this work, where a self-focusing effect is found to be present.

The simplest correction found in literature is to use a surface adaptive array. This technique allows for adaptive imaging through the employ of a flexible array, where the elements conform to the surface of the inspected part. In these cases, the Hamiltonian is considered that of a constant material, making phased delays analytic. These techniques have proven reliable; however, cost and frequency limitations make them unsuitable for this work.

In many cases, the goal of real-time imaging results in the simplification of using only a first-order ray theory expansion, where the time of flight is employed, but

the amplitude weighting, or second-order equation, and subsequent renormalization, is ignored. This simplification has been employed in multiple works [60–62] but has been found insufficient in the imaging of highly curved surfaces, such as those in this work. This occurs due to the fact that the surface acts as a lens, meaning that the corresponding amplitude weighting varies greatly between elements.

Some adaptive techniques have also used plane wave emitters[63–65], where the phase delays are updated to simulate a plane wave emission in the secondary media. This technique was not explored as it requires specialized equipment to perform efficiently. It also suffers from the same amplitude considerations previously mentioned.

Convolutional imaging has been used in non-destructive testing, although the renormalization was not performed. This work, done in a more simple media, was shown to be effective in increasing the resolution of the image, as theory suggests[66–68].

One proposed method that may prove satisfactory is that of the virtual source aperture imaging. This technique poses to recast the emitted and received wave data to a set of new emitters/receivers[69–74]. This technique is found to provide improved imaging results but can be broken into the same class of imaging proposed here. It is notable that the renormalization technique was not employed in these works, and the amplitude coefficients were only considered using simple geometric approaches.

# Chapter 6

# Ultrasonic Equipment Manufacture, Design and Calibration

Acquisition and processing components tend to be grouped into a single electronics unit. In this section, we discuss these components at a simplified level as applicable to this work.

## *6.1. Data Acquisition and Processing Equipment*

In order to generate an ultrasound signal, a transducer is employed to convert electrical signals into a mechanical one. In piezoelectric transducers, this is done through a high voltage emitter that drives the transducer, sometimes referred to as a pulsar. The excitation signal can be produced in a variety of forms, including unipolar, spike, bipolar and even arbitrary signal generation on advanced equipment. In current systems, the most common modalities are unipolar or bipolar, as they offer a lower cost of implementation. In general, bipolar pulses allow for an increase in the energy transmitted into the sample, at a cost of a longer pulse length.

In phased array equipment, multiple pulsars must be synchronized together to a common clock in order to allow for precise time delays between the individual elements that form the imaging basis. In general, these pulsars use a common high voltage rail, meaning that most phased array systems do not allow for per element amplitude variations. Some variation can be introduced by varying the pulse length and pattern[75]; however, in the full matrix capture modality used in this work, such features are not needed for optimal imaging.

On the reception side, the primary components are the amplifiers, filters and analog-digital converters (ADC). Due to the low efficiency of ultrasound transducers, the received signal after emission and reception is often of a voltage that is unreadable by most ADCs. In order to overcome this, amplifiers are employed, offering gain amplitudes in the 50-92dB range on most equipment using low noise amplifiers.

Filtering of the signal to remove noise can occur before or after conversion to a digital signal; however, as the application of pre-filters often requires the design of a specific circuit for any given signal, many systems offer digital filtering. In this work, we employ a filter in the post-process to remove the presence of DC components from the signal.

The final process is to convert this analog signal to a digital format. Industrial ultrasound systems tend to range from a sampling rate of 100MHz at 10 Bit to 125 MHz at 14-bit resolutions, although lower sampling rates can be used in most applications. The bit range determines the amplitude resolution, while the sampling rate determines the temporal resolution of the signal. In general, the sampling frequency only needs to be sufficient to meet the Nyquist limit; however, as white noise is inversely proportional to the root of the sampling rate it is common to use higher sampling rates. These higher rates also have the advantage in that interpolation can make use of simplified methods, such as cubic, linear, or nearest-neighbour interpolation models as the sampling rate increases. In this work, the sampling rate is approximately 8 points per wavelength, allowing for the nearest neighbour interpolation to be employed.

In a phased array system, the number of amplifiers and ADCs is increased to accommodate the number of elements in the basis. By tying to a common clock rate, the time at which the signal is recorded can be known relatively between individual channels and with respect to the emission pulse, allowing for imaging to occur. In full matrix capture, the electronics can be simplified, as the data can be collected using a series of emissions, varying the receiving elements while keeping the emission element constant. This, in theory, allows for only a single channel receiver to acquire full matrix data; however, it is beneficial to employ a multi-channel to increase acquisition speed, preventing operator movements from introducing artifacts into the imaging process through the introduction of a temporally dependent Hamiltonian.

The formation of an image using the previously discussed technique can occur in hardware using an FPGA when the employed technique is simple, such as the case of phased array imaging. In this work, we make use of a desktop graphics card for the computation of the delay laws, fields, and image formation process. As these graphics processors have drastically increased in power efficiency and portability over the course of this project, it is hoped that a portable implementation may be possible in the future.

For acquisition electronics, this project has used a total of 5 differing systems for acquisition; however, the images in this work have all been taken using the pragma pro system with a PAUT32/128 instrument cartridge. This system offered a number of benefits in that it can address arrays up to 128 elements and offered higher sampling rates (125 MHz at 12-bit resolution), bipolar pulsars and an

open-source API for data acquisition. In order to allow for acquisition and processing, the C++ API was incorporated into a MATLAB interfacing library, allowing for direct data acquisition in MATLAB. Currently, data is acquired in a multiplexed fashion; however, future software updates are expected to add full matrix capture support.

### *6.2. Transducers*

Ultrasound transducers are any material that converts one form of energy into ultrasound. In general, these transducers can come in the form of piezoelectric, electromagnetic acoustic transducers (EMAT), magnetostrictive transducers, and others. In this work, we make use of the piezoceramic transducer due to the higher resolutions the technology currently offers. In this section, the manufacture and design of ultrasound transducers are discussed, along with areas of future improvement as manufacturing advances.

#### *6.2.1. Piezoceramic*

A piezoceramic material is one that can be polarized through the application of an electric field. By heating these materials above the curie temperature, and applying a large electric potential, a net polarization can be introduced into the lattice. If this field is maintained during cooling, the resultant material will have a fixed polarization[76]. The application of an electric field subsequent to this process will result in the contraction or expansion of the material as the internal field is perturbed.

The manufacturing of a transducer involves a multi-part process. In the design of a single transducer, a wafer of piezoelectric material is constructed to be at a

half-wavelength thickness of the desired frequency, allowing for an on-resonance emission. This wafer is then bonded to a silver electrode on either side, which allows for the application of a potential across the wafer. These electrodes must be bonded to conductive wires to allow for the application of an external potential.

In general, ultrasound imaging employs pulsed transducers to allow for higher resolutions and to better approximate the desired delta function. In order to shorten the emission pulse, a damping material is added as a backing to the array. This material serves the purpose both of shortening the pulse of the transducer and attenuating the wave emitted in the opposing direction. Such an attenuation, combined with a scattering material at the back of the transducer, reduces the need for considering the back-propagating pulse.

The final design component of a transducer is the front face material. In general, piezoceramic materials have an impedance that is approximately 20 times greater than water[75], resulting in poor transmission of sound. In order to alleviate this, the use of a quarter-wave matching layer is employed. This matching layer, in theory, provides a perfect transmission into the second media when the proper impedance is selected; however, as ultrasound transducers tend to be broadband, this layer is not completely effective, resulting in additional frequency changes due to the off-resonant conditions caused by such a cavity. Due to this, the front face can also play a role in the pulse shape of a transducer. The complete design, seen in Figure 24, serves as a reference for the design of phased array transducers.


Figure 24 – An example of the transducer design. The silver electrodes are used to apply a potential to a piezoelectric element, causing a resonant excitation. By using a heavy backing material, the pulse length can be dampened to produce a pulsed signal. The matching layer is employed to increase transmission energy into the intended material.

In the manufacture of a phased array transducer, additional steps must be employed. A larger, single element is sectioned into a set of smaller elements during the production process. Each individual element must then be electrically connected using a series of cables, with additional steps performed to reduce cross element interference. These additional steps make phased array manufacturing a far more complicated process; however, the design principles remain theoretically approachable.

### *6.3. Transducer Design*

The design of a transducer can make use of a single crystal, 1D linear array, or 2D matrix array. These transducers can have a physical focusing applied, changing the curvature of the transducer, be cut into a variety of shapes and potentially even be flexible[75]. The various layouts of linear arrays, seen in Figure 25, serves as a reference for describing arrays in this work. The exact array design always depends on the inspection at hand, with the transducer array, which physically forms the imaging basis, ultimately determining the resolution limit of the system.

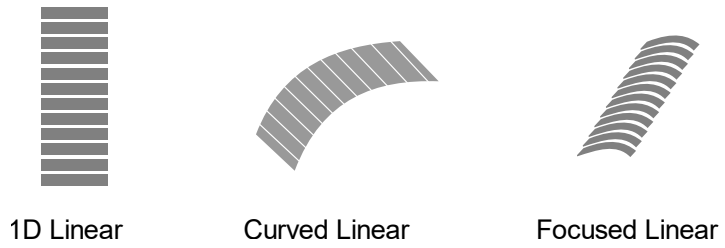


Figure 25 – An example of the various linear array types available. The 1D linear has no focus applied in the non-phased or passive dimension. The curved linear array applies a focus on the active or phased direction while the focused linear applies the focusing in the passive direction. Adapted from [77].

In this work, we make use of a linear array, which blends the elements of both single element and phased array transducers in what is referred to as a passive and active element respectively. As a result of this blending, the design of a linear array involves optimizing both dimensions using the design principles for a single element and phased array, such that both will be explored in this chapter. Array design is covered in almost any standard ultrasound book as well as numerous papers[41][78].

### *6.3.1. Frequency and Bandwidth Selection of Transducer*

The selection of center frequency and bandwidth ultimately determines the pulse shape and the resolution limit of the system. In general, although a Dirac impulse is desired, the pulse shape takes the form of a driven damped system due to the capacitive effect of the transducer. On reception, this process is reversed, yielding a transducer signal with a characteristic pulse shape more akin to a gaussian. The pulse length tends to be specified in accordance with the length at half maximum and the length at the tenth maximum, allowing for a resolution estimation. In cases where the pulse is Gaussian-shaped, it is common to also

specify the bandwidth of the transducer and its Q-factor; however, as the resolution is the desired property, non-gaussian envelopes tend to be common.

In this work, high-resolution arrays were explored, of which two common designs are applicable. In traditional manufacturing, pulse lengths of 2.5 cycles are common; however, in the design of flat arrays, resolutions of up to 1.5 cycles are capable of using proprietary electroacoustic designs. In this work, we explored both options, each of which offers trade-offs in terms of axial and lateral resolution. During the manufacturing process, the manufacturer was instructed to attempt the highest possible axial resolution using a design frequency of 18.5 MHz.

### *6.3.2. Passive Element Design*

The design on the passive dimension of the transducer follows the same principles of designing a single element transducer. Although the transducer element is square, the design principles often make use of the analytic functions that can be found for circular transducers, with a minimal deviation between the two patterns being neglected in most cases.

In the design of a single element transducer, the size and shape of the transducer can be varied to change the emission pattern. When a flat transducer is used in emission, it is common to make use of the natural focus of the transducer to achieve a higher lateral resolution. This effect relies on the natural focusing effect that occurs between the near field and far-field of an emitting element, as seen in Figure 26. This near field occurs at a fixed distance, $N$,

based on the wavelength of the transducer, $\lambda$, and its diameter, $D$, in accordance with[39],

$$N = \frac{D^2}{4\lambda} \tag{78}$$

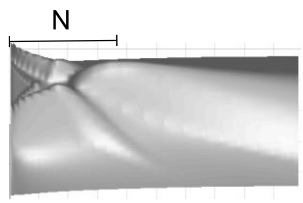


Figure 26 – a typical emission pattern of a circular piston transducer. An interference pattern results from the aperture of the emitted, resulting in a peak at a defined near field distance N from the transducer surface.

With this in mind, a single element transducer is sized in accordance with its desired imaging distance. In this work, 12 mm was determined to be the desired distance between the front surface and the transducer and the workpiece. In addition, a depth of up to 1 mm of the workpiece component was expected; as a result, the modified calculation was performed to take into account the added propagation distance. Ignoring the change in the divergence rate at the boundary due to refraction effects, the desired transducer diameter was found in accordance with,

$$D^2 = 4(\lambda_1 N_1 + \lambda_2 N_2) \tag{79}$$

where the wavelength and propagation distance for each media is used in the calculation, yielding a diameter of 2.6 mm. At this diameter, simulations of the beam field in water were conducted. These simulations, shown in Figure 27 and Figure 28 below, serve as a reference from which other designs are compared.

Measurement of the axial and lateral amplitude profile shows a beam width of 2.48 mm at full-width half maximum in the lateral direction, with minimal field deviation in the axial direction.

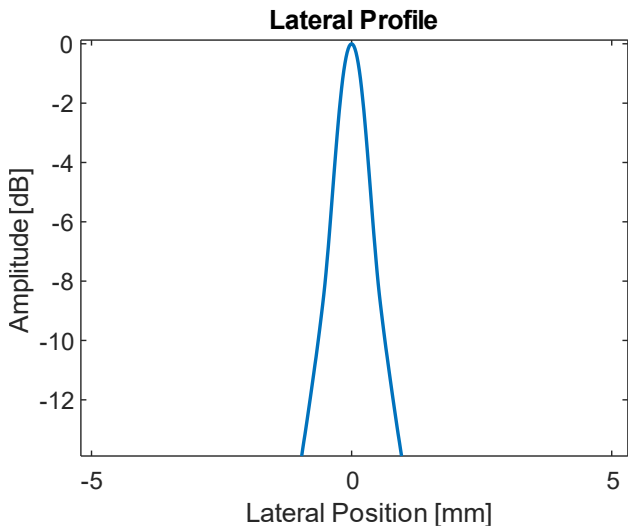


Figure 27 – A depiction of the lateral profile of the emission of a flat transducer used in the work. A beamwidth of 2.48 mm at full-width half max was found.

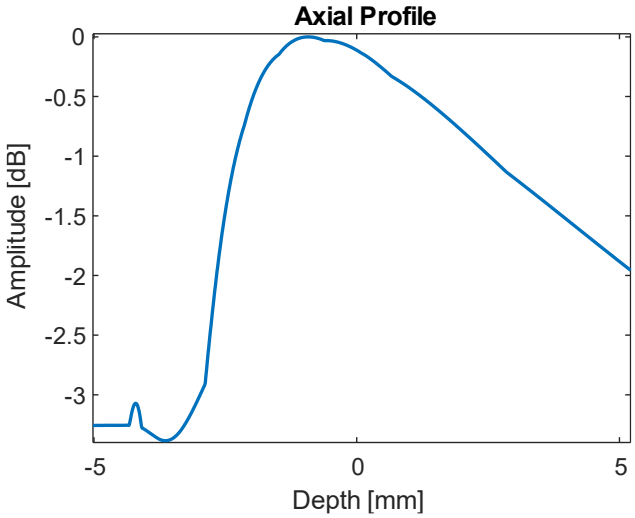


Figure 28 – A plot of the axial transducer profile for the unfocused array used in this work. The field is indicated for the passive imaging direction with minimal deviation found along the length of the transducer.

Although the lateral resolution of such a transducer was found to be poor, in samples with a cylindrical symmetry the resolution is not expected to affect the results. As samples break this symmetry, imaging is expected and was found to degrade poorly.

In the case of a focused transducer, the design considerations must be modified. A focused transducer makes use of mechanical lensing, either through a physical lens or, in this case, a curving of the array element, to bring the focal spot closer to the array. By choosing a radius of curvature that corresponds to the desired focal length, a high lateral resolution can be achieved.

In addition to the curvature, the size of the transducer affects both the resolution and the focal length, or region over which the amplitude is stable. Areas within the focal length can be imaged without changing the position of the transducer by varying the reception time, with a small trade-off in resolution. As the size of the transducer increases, the lateral resolution increases at a trade-off to the focal length, as shown in Figure 29, where the convergence/divergence rate is seen to change as a function of the transducer size or angular span. This allows for some estimate of the lateral resolution in accordance with the abbe diffraction formula[78],

$$W = \frac{0.44\lambda}{\sin\left(\frac{\alpha}{2}\right)} \tag{80}$$

where the beam width $W$ is related to the arc angle $\alpha$ through the center frequency wavelength.

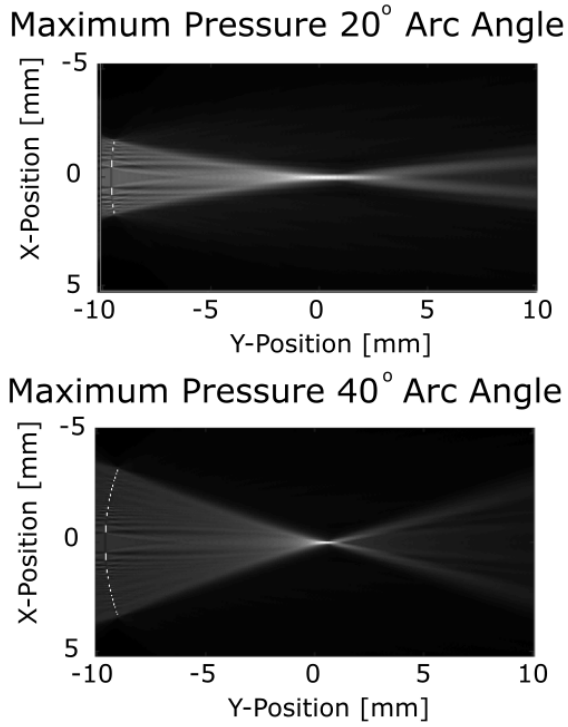


Figure 29 – A depiction of the focal length as a function of the transducer arc angle. As the size of the transducer increases, the convergence and divergence rate increases as well. This can result in variations in the image amplitude as a function of depth.

In this work, simulations were performed on an arc angle between 10 and 40 degrees with the spatial and lateral resolution for each analyzed as shown in Figure 30. In each case, a radius of curvature of 15 mm was employed as in the flat transducer case. From this array of simulations, a 20-degree arc angle, corresponding to a 5mm diameter, was chosen as the optimal trade-off. As simulations were performed in water, it was worth noting the focal length is reduced by approximately a factor of 3 based on the variance in sound speed between bronze and water.

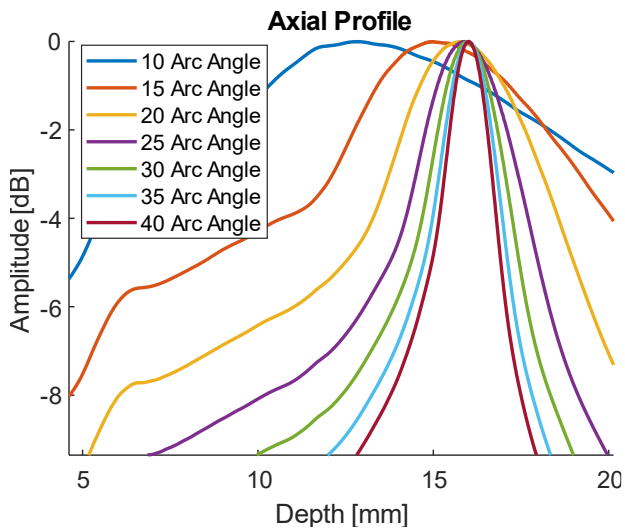


Figure 30 – A depiction of the axial field amplitude for the inactive direction of the phased array based on the arc angle. As the arc angle increases, the field converges and diverges at a faster rate, resulting in a lower focal length.

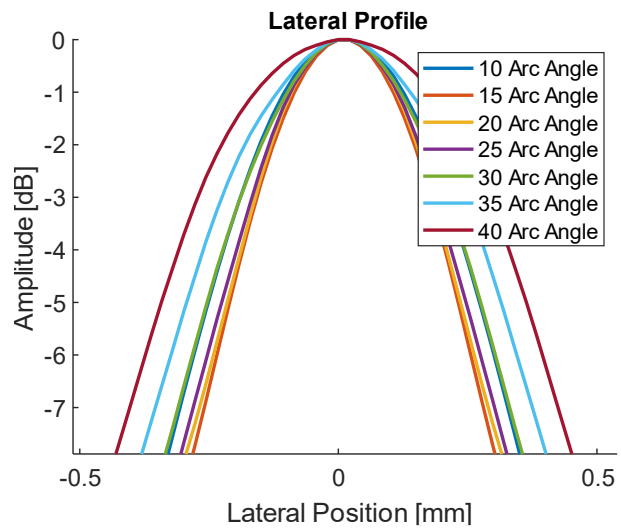


Figure 31 – A depiction of the lateral field amplitude for the inactive direction of the phased array based on the arc angle. A notable increase in the resolution occurs as the angle increases from 15-20 degrees; however, further increases result in minimal gains.

Although both axial and lateral resolution is important, other trade-offs such as alignment must be considered. In the case of imaging a surface, the incident wave must return to the transducer in order to allow for imaging. In the case of

the flat, 2.6 mm array, a small tilt of the array results in a limited amount of the energy returning to the array. This condition is notably relaxed in the curved array, making alignment easier during imaging.

### *6.3.3. Active Element Design*

In the design of the phased or active dimension, additional considerations are needed. With the individual elements forming an equivalent basis, we must apply both the elements of traditional design with the limitations of sampling theory. In general, the design variables in the active dimension are that of element size, pitch and the number of elements. These features, shown in Figure 32, are indirectly related to the kerf, or sectioning width, and total aperture or size of the transducer.

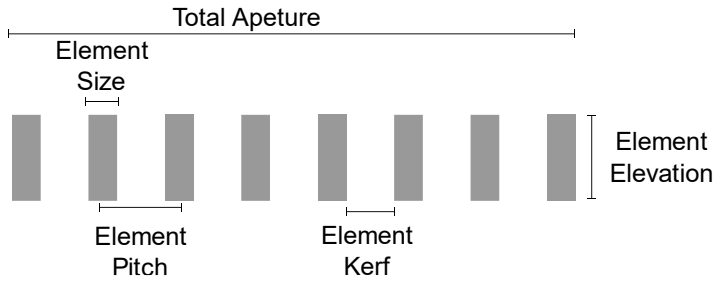


Figure 32 – A depiction of the various elements of a phased array's design.

Based on sampling theory, an ideal element should be a point source emitter placed at half-wavelength spacing; however, at the frequency of 18.5 MHz in water, this results in an element spacing of 40 microns. Currently, the smallest available sectioning method for industrial applications results in a kerf of 25 microns, making manufacturing problematic. Although future manufacturing techniques may allow for this, decreasing element size also results in decreased amplitude and greater variation between elements, as the thickness and

polarizability are expected to vary along with a manufactured transducer. In our design, the smallest achievable element pitch was 100 microns, with designs in this work being based on this limit.

In addition to manufacturing limits, as the probe was designed prior to the purchase of the acquisition system, the limitation of a 64-element design was explored. This was chosen as 32-element designs were found to be inadequate in earlier tests[79], and most hardware is only available in 16, 32, 64 or 128 channel arrangements.

In theory, sampling limitations due to the choice of a particular pitch result in the presence of grating lobes; however, the intensity of these grating lobes has also been found to be dependence on the choice of element size used in the design.

### *6.4. Element Sizing*

At the frequency we desired, a curved linear array was unavailable, meaning that the elements are linear in the active direction. The element size in a flat or focused linear array determines the directivity of the element in accordance with a single slit diffraction formula. In this work, the comparison between various element sizes was performed for 50 to 200-micron elements. Each element has a directivity pattern as demonstrated in Figure 33.

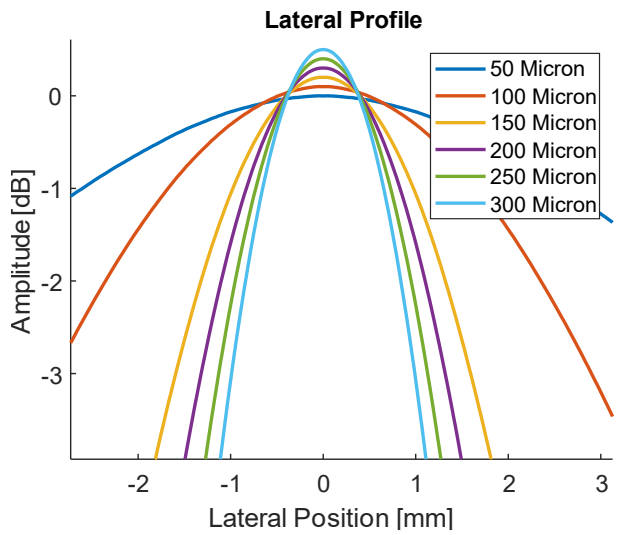


Figure 33 – A depiction of the various element sizes. Side lobes within this imaging range appear as the element size increases beyond 125 microns, with the field approaching that of the point source as the size decreases.

As can be seen in the figure, the directivity of the elements does not produce any side lobes within the region of imaging; however, the angular sensitivity does decrease as the element size increases. As the 50-micron element produces a near idealized signal, we can see that the 75, 100- and 125-micron element allow for a minimal deviation across the span of 4 mm. As the radius of curvature of the joints has the potential to be very small, these element sizes were explored to provide the highest angular sensitivity.

### *6.5. Element Pitch*

With the chosen element size, the determination of the pitch can be made. Given that the smallest element kerf possible is that of 25 microns, the elementary pitch is limited to that of 100-150 microns. In this work, we explore 100, 125, and 150-micron pitches. These pitches violate the Nyquist limit, meaning that the presence of grating lobes is expected at large steering angles. For the case of

on-center steering, the location of these lobes can be estimated using the grating lobe formula[78], where the angle of the grating lobe is found by using,

$$B_{grating} = \sin^{-1}\left(\frac{m\lambda}{p}\right) \tag{81}$$

where, $m = \pm 1, \pm 2, \pm 3$

For the case of the 150, 125 and 100-micron pitch, this results in grating lobes at the 37, 46 and 64-degree mark respectively. Using this general rule, steering at these angles or above is expected to result in the imaging artifact of aliasing, where certain spatial features are remapped to differing locations. In ultrasound, the cause for this effect becomes apparent in Figure 34, where an appreciable intensity is located at both the focal point on the right and the side lobe on the left of the image. This results in any measure along the central lobe having a partial mapping of any reflectors located in the grating lobe present in the obtained signal. For reference, a depiction of the improvements that can be made via the inverse apodization is included for reference.

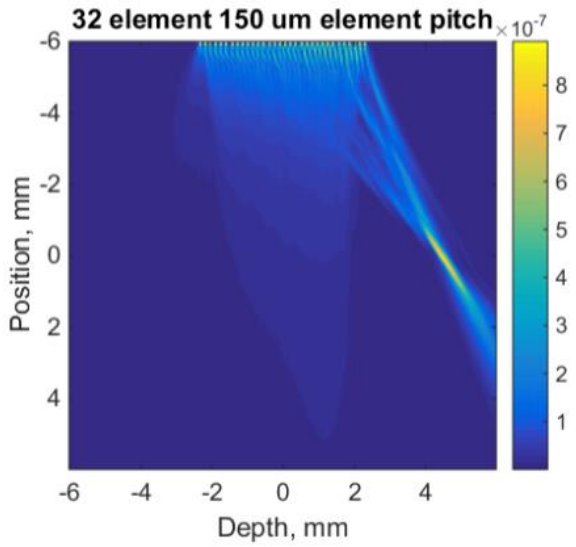


Figure 34 – A depiction of the side lobes and grating lobes produced by an element pitch of 150 um. In imaging, the side lobe results in an incorrect remapping of features to other parts of the image due to spatial aliasing. This effect can be reduced using apodization based on inverse methods, as is done in this work.

The number of elements was chosen to be 64 as an aperture of 32 elements proved problematic in earlier tests due to the limited effective imaging area of the array[79]. A minimum aperture was defined in accordance with the near field of the transducer elements. In theory, this means that a reflector located off-centre to the array, as shown in Figure 35, must have an effective aperture above that point such that the near field condition is met. For the transducer explored here, a 12 mm imaging distance corresponds to an effective aperture of 20, 16 and 14 elements for imaging to occur in accordance with the given pitches or 100, 125 and 150 microns. For an array of 64 elements, this results in an effective imaging region of 4, 5.5 and 6.9 mm respectively.

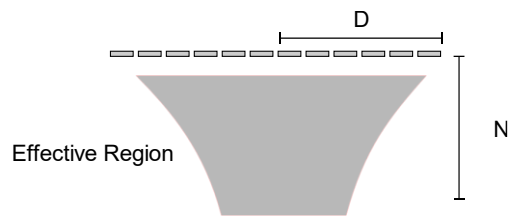


Figure 35 – A depiction of the effective imaging region, or region under which the transducer possesses a large enough aperture to form an in-focus image. Imaging outside of this region is expected to have notably lower quality as the transducer cannot physically focus.

The secondary issue in the case of transducer size is the inability to image at larger angles. In the case of an angular reflector located at a fixed distance D from the transducer, an effective angular aperture can be defined based on the angle of the reflector relative to the surface of the transducer, $\theta$, and an effective angular aperture, $D_{ang}$, can be found based on the angular distance, $N_{ang}$. This aperture is given in accordance with,

$$D_{ang} = \sqrt{\frac{N_{ang}}{4\lambda \cos\theta}} \tag{82}$$

If this effective aperture, shown in Figure 36, does not meet the far-field distance, imaging at these angles is expected to again suffer from a loss of resolution. This limit, in addition to the directivity of the elements, requires that a trade-off be made between the element pitch and the array size that is non-trivial in nature. It should be noted that the above equation is based on the assumption of the array's ability to generate a synthetic array at the angle of incidence with its surface.

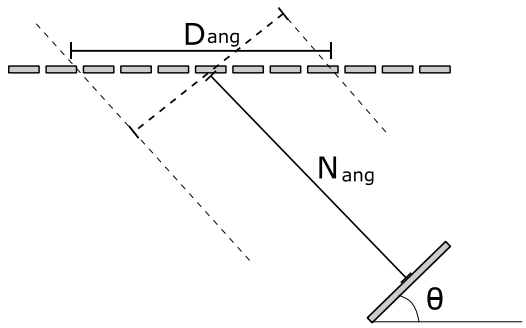


Figure 36 – A modified near field equation for imaging at angles. This near field assumes an ideal transducer, using an effective aperture based on the angle of the defect. Defects whose angle and depth are greater than allowed will have decreased visibility.

### *6.6. Simulation Results*

Although we can estimate steering lobes, the amplitude and influence on imaging are difficult to estimate. To determine the presence of side lobes and gauge imaging quality, a series of brass phantoms were simulated in water with a fixed distance of 12 mm between the transducer and surface. The transducer element pitch was varied from 100 to 150 microns, with a 25-micron kerf to investigate the potential designs.

Simulations were performed for each of the array sizes to acquire full matrix data on joints with a radius of curvature between 1 and 4 mm. In this case, the ability to image each boundary is analyzed for the angle and distance at which imaging becomes impossible. Although we later investigate sub-surface imaging, the ability to steer at greater angles directly affects this. It can also be understood that the boundary itself acts as a second aperture, meaning that increased visibility of the boundary is directly correlated to the ability to image sub-surface defects.

After the data was simulated, reconstruction was performed using the total focusing method, for which each point in space was focused with a grid size of 256*512. As the boundary size changes in each image, the axes were scaled to display an axis with equal scaling in both directions.

From the reconstruction, it became apparent that the image quality did not change significantly for varying pitch, with the decreased pitch resulting in a lower effecting imaging area. At the 4mm radius, the visibility of the upper edge was severely degraded in both the 100- and 125-micron pitch images due to the smaller total aperture. As a result, a pitch of 150 microns was selected for this work.

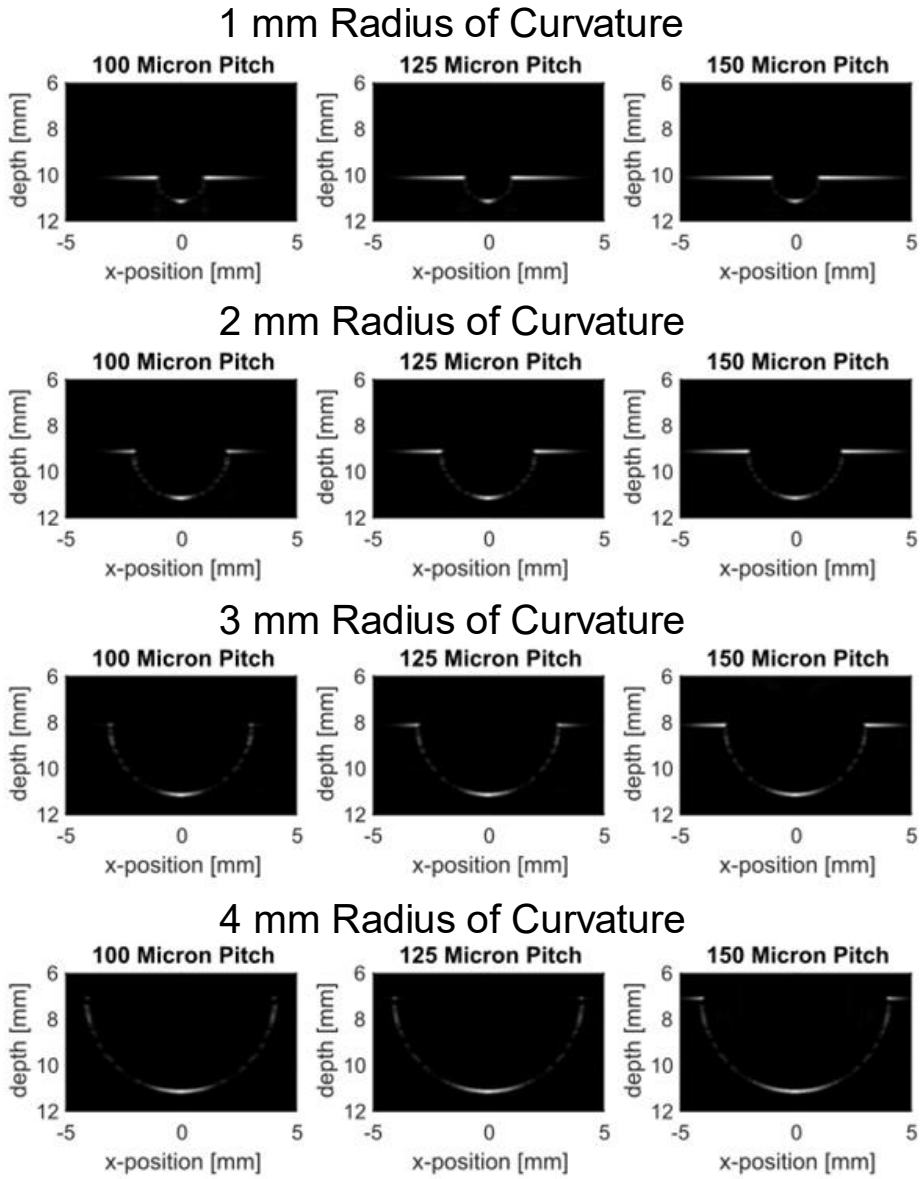


Figure 37 – A depiction of the imaging of bronze phantom in water. Here, the removal of a section of the bronze to simulate a varying degree of curvature is performed. As the probe size was increased, the effective imaging area was found to increase without any loss of angular sensitivity. For this reason, a larger probe was found to offer benefits over those of smaller size.

### *6.7. Experimental Calibration*

Based on the previous results, both a flat and focused transducer were purchased, with the flat being used to image the bronze phantoms in subsequent sections and the focused transducer found to be more applicable to welded

joints, where the geometry was found to vary such that a linear symmetry was not present. The properties of these transducers are summarized in Table 1.

| Parameter | Value (Focused 15mm) | Value (Flat) |
|---|---|---|
| Frequency | 16.5 MHz | 16.5 MHz |
| Pitch | 0.15 mm | 0.15 mm |
| Kerf | 0.025 mm | 0.025 mm |
| Element Elevation | 5 mm | 2.6 mm |
| Number of Elements | 64 | 64 |

Table 1 – An outline of the transducer properties used in this work. The primary difference between the two arrays is the choice of the elevation, with one probe offering a focused profile and the other being flat.

Calibration of a transducer can include several standard measurements. Measurements can include element sensitivity, bandwidth, center frequency, element cross talk, impedance, and pulse duration. Many of these standard measurements are done during the manufacturing process; however, some measurements, such as the overall probe imaging ability, must be done in the lab. In this case, the imaging ability was assessed by determining the point spread function (PSF).

In order to measure the PSF of the imaging system, a 30-micron wire was used as the imaging target. As the wire is 1/3 of the wavelength, it meets the requirements of the point source assumption and should be suitable for the 60% bandwidth typical of transducers. This target was placed at the center of the imaging system with water used as a coupling. Full matrix data was then acquired, with focusing done using the standard TFM algorithm. The resulting image, seen in Figure 38 and Figure 39 for the flat and focused transducer respectively, shows the point spread function. From this image, both vertical and

horizontal profiles were extracted, with the horizontal profile being extracted after enveloping the image. The full-width half max and full-width tenth max were then determined. The results of these measurements are detailed in subsequent pages. The presence of grating lobes in the image was found to be minimal, with the amplitude being around 5% of the main peak energy.

| **Linear Array** | |
|---|---|
| **Lateral Resolution** | |
| **Amplitude Level** | Width |
| **50%** | 0.14 mm |
| **10%** | 0.25 mm |
| **Axial Resolution** | |
| **Amplitude Level** | Width |
| **50%** | 0.07 mm |
| **10%** | 0.13 mm |

Table 2 – An outline of the transducer resolution for the linear, unfocused array.

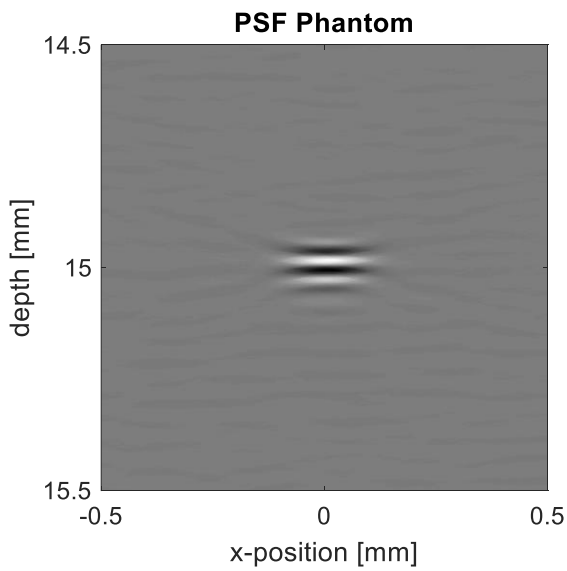


Figure 38 – A depiction of the point spread phantom for the transducer that is unfocused in the elevation direction.

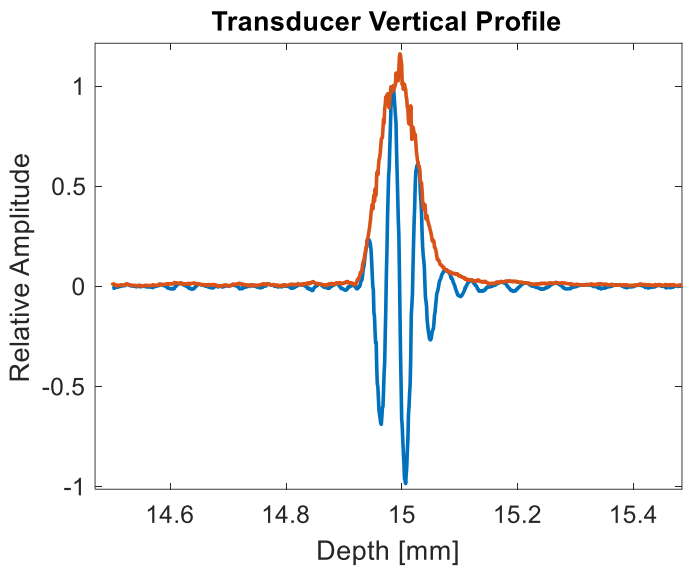


Figure 39 – A depiction of the vertical profile for the unfocused array point spread function. In this case, the measured resolution was determined in accordance with the full-width half and full-width tenth max of this diagram.

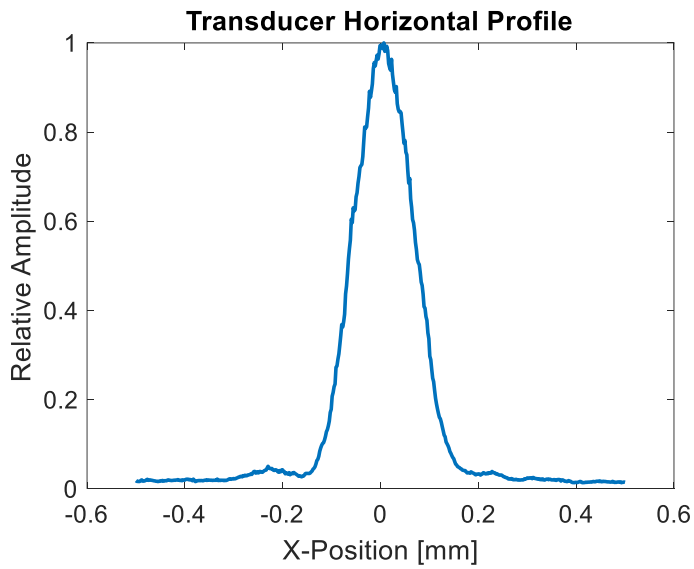


Figure 40 – A depiction of the horizontal transducer profile for the point spread function of the unfocused array. In this case, side lobes are present on both sides, but are notably low, indicating good focal ability.

| Focused Linear Array | |
|---|---|
| **Lateral Resolution** | |
| **Amplitude Level** | Width |
| **50%** | 0.14 mm |
| **10%** | 0.25 mm |
| **Axial Resolution** | |
| **Amplitude Level** | Width |
| **50%** | 0.07 mm |
| **10%** | 0.13 mm |

Table 3 – An outline of the transducer properties used in this work. The primary difference between the two arrays is the choice of the elevation, with one probe offering a focused profile and the other being flat.

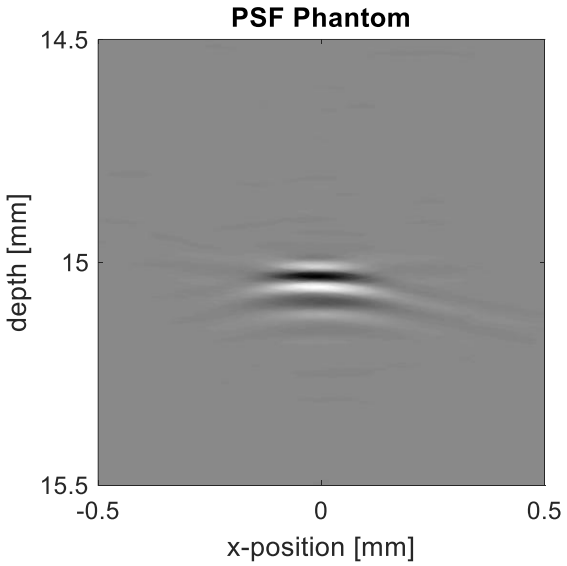


Figure 41 - A depiction of the point spread phantom for the transducer that is unfocused in the elevation direction.

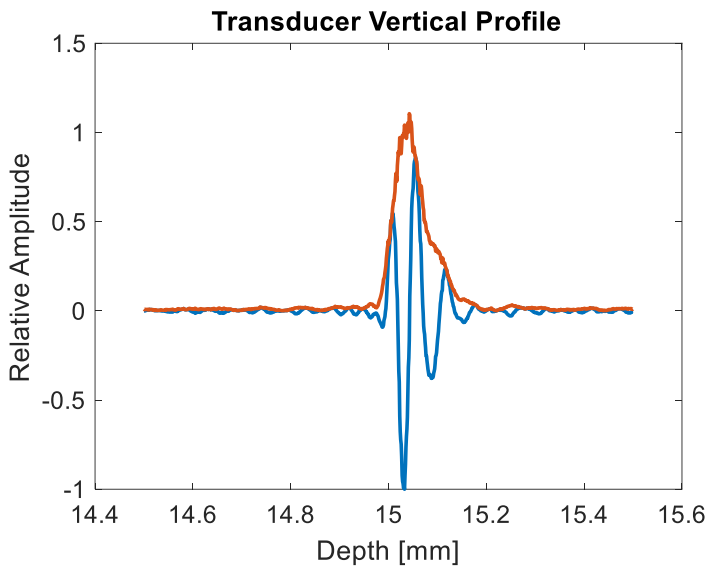


Figure 42 - A depiction of the vertical profile for the focused array point spread function. In this case, the measured resolution was determined in accordance with the full-width half and full-width tenth max of this diagram.

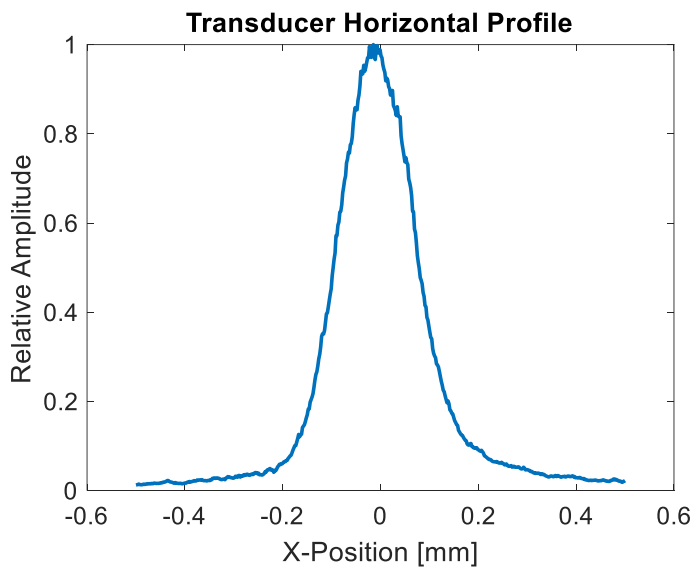


Figure 43 – A depiction of the horizontal profile of the elevation focused array. A minor asymetry is observes in the function and the side lobes are at a low enough amplitude so as to not be seen.

# Chapter 7

# Imaging of Bronze Phantoms

In order to determine the viability of the developed imaging technique for brazed joints, phantoms were simulated and manufactured to allow for the exploration of a variety of defects in an ideal imaging environment. Although these phantoms are two dimensional and do not properly represent a true braze, they were found to illuminate the limitations of the proposed technique. In this chapter, we discuss the results of analyzing these idealized specimens.

## *7.1. Design of Defective Samples*

In order to design a suitable set of phantoms, measurements were taken of brazed surfaces, showing them to be of a radius of curvature of 1.5 mm and up in production pieces. In previous work, joints of higher radius were found to be more difficult to inspect without applying the second-order corrections, making these smaller radii the subject of this chapter[79]. It shall be shown, however, that as the sample radius increases, traditional techniques can be employed.

For simulated joints, a radius of 1-4 mm was explored through simulation. In each case, a variety of defects were constructed, with modifications made in consultation with our research partner to ensure a likeness to the desired defects.

In order to have a reference sample, one phantom was designed with no physical defects. Here, a fixed radius/diameter is machined from the sample. Previously, this was explored for probe design; however, in this section, we shall explore the

limitations introduced by the probe design, imaging approximations, and radius of joint curvature. This phantom, seen in Figure 44, sets the baseline from which other samples are manufactured.

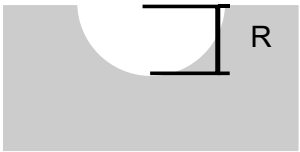


Figure 44 – An example of the standard from which all samples have been built. This block contains a simple radial cutout simulating the upper surface of a bronze braze joint.

For the case of a pore, the pore was selected to be of a fixed size of 0.5 mm and at a depth of 1 mm, with a deviation from the center of 20 degrees. Although these parameters could deviate in a joint, this was estimated to be within the comfort level of detection. Due to the sample, seen in Figure 45, being 2D, the pore is manufactured and simulated as a through-hole rather than a true pore.

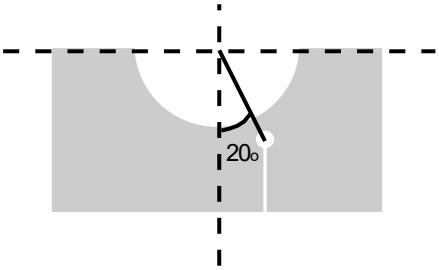


Figure 45 – A depiction of the size and location of a pore relative to the boundary in an idealized phantom.

By removing a narrow band of material from the bronze block, a simulated lack of adhesion can occur as seen in Figure 46. Like the pore, this lack of adhesion was made at a fixed depth of 1 mm but at a higher tilt angle of 45 degrees. In the

case of simulation, the entire section after this band was removed to simulate an absolute reflection. In the case of the real phantom, the formation of an air gap in water due to the narrow size of the slot resulted in an ideal reflection.

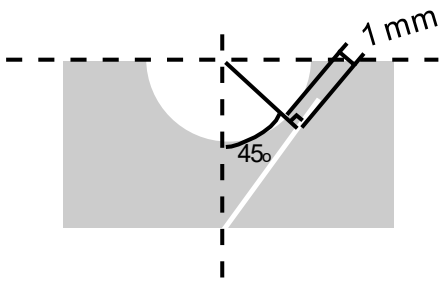


Figure 46 – A depiction of a phantom used to simulate a lack of adhesion in the braze specimen. By keeping a fixed angle and depth, the determination of the system's ability to imagine such a defect can be explored.

The design of a crack poses some challenges, as cracks are physically different from a machined slot. As the cracks desired for inspection are non-surface breaking and inside the filler material, this phantom, seen in Figure 47, was designed to be of a bottom crack.  In the case of simulations, a minimum width of 1 grid point was used; however, in the actual manufacturing process, the minimum cut possible was a 300-micron cut. In both cases, non-linear effects from the crack are ignored, somewhat limiting the viability of comparison. Ideally, a real crack could be generated using stress methods; however, the facilities to manufacture a sample were unavailable, with the exact location of such a crack often difficult to reproduce.

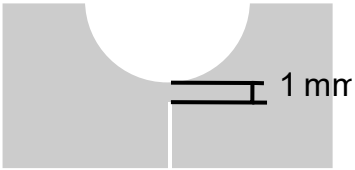


Figure 47 – A depiction of a bottom crack in a sample. In this case, physical sectioning of the material was performed, making the response somewhat differing from a physical crack.

To simulate the determination of braze thickens, both concave and convex bottom surfaces were constructed. In each case, the thickness between the top and bottoms was 1 mm, as indicated in Figure 47 and Figure 48. These phantoms were used to gauge both the vertical and angular resolution of imaging technique, yielding some estimation of its ability to size the weld correctly.

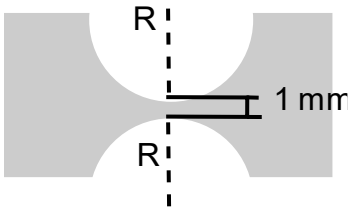


Figure 48 – A depiction of the concave bottom surface joint. The bottom surface is made to be the same diameter as the top surface at a minimum depth of 1 mm.

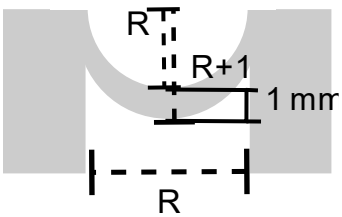

Figure 49 - A depiction of the convex bottom surface joint. The bottom surface is made to be 1 mm larger diameter than the top surface at a fixed depth of 1 mm.

In addition to simulation, each phantom was manufactured according to the specifications for the 4 mm radius of curvature. In each case, electron discharge manufacturing [EDM] was employed due to its ability to offer resolutions higher than most traditional manufacturing techniques. These phantoms, shown in Figure 50, serve as the experimental reference samples. In order to match the expected noise levels in the braze specimen, the same alloy was purchased in both rod and ingot form. The material properties between these forms were found to have almost no deviation. As the Ingot is a rapid cooling process, changes in material properties due to variations in cooling rate were expected to be seen between these samples.

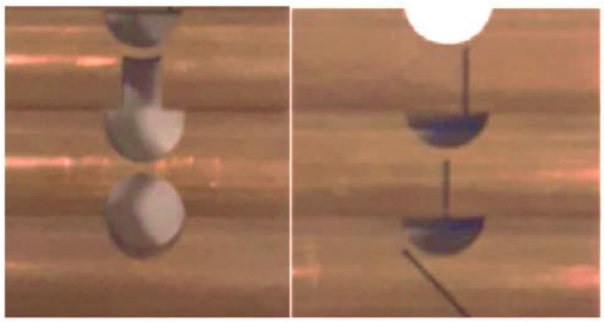

Figure 50 – A depiction of the physical phantoms used in this work. In each case, the phantoms were designed in accordance with the specifications using a fixed upper surface curvature of a 4 mm radius.

### *7.2. Imaging Results*

When imaging the phantoms, analysis of the phantoms with no physical features provides a useful baseline for analysis. These samples allow for the measurement of image artifacts in the absence of experimental noise. In order to

maximize the layout of artifacts, the threshold used in the reconstruction process was removed to maximize the potential for artifacts. These reconstructions, shown in Figure 51, are used subsequently to describe the variety of artifacts.

The first issue is the apparent circular banding that appears in the bottom of all images but is only inside of the reconstruction area in the 1 and 2 mm specimen. This artifact results from reflections in water being remapped to the bronze portion of the image. This is evidenced by the change in the position of this reflection as the radius of the upper surface increases.

The second issue is also occurring due to the upper boundary being remapped; however, in this case, it is remapped to a portion where a grating lobe is producing a notable portion of the field. This is evidenced in the 1 mm phantom by the sharp inversion of the boundary as it reaches this point, which corresponds to the half-wavelength offset that has been shown for side lobes. This was further verified by analyzing the amplitude fields of the elements in post-processing.

The third issue occurs due to diffraction off of the upper surface of the circle, where the curved portion reaches the flat. This defect, seen by a visible banding below the upper surface, was found to be eliminated in the imaging of real samples, which do not contain sharp changes in geometry.

In general, these artifacts completely corrupt the image when the radius of curvature dropped below 1.5 mm, making imaging impossible in the smallest of joints. In addition to this, it is notable that only a portion of the upper boundary is

detectable, meaning that the boundary itself will be seen to act as an aperture due to the angular dependence of the transmission coefficient and the limited angular sensitivity of the probe. As a result of this, imaging at radii of 1 mm is rarely able to form a focus at the intended defect depth, further complicating imaging.

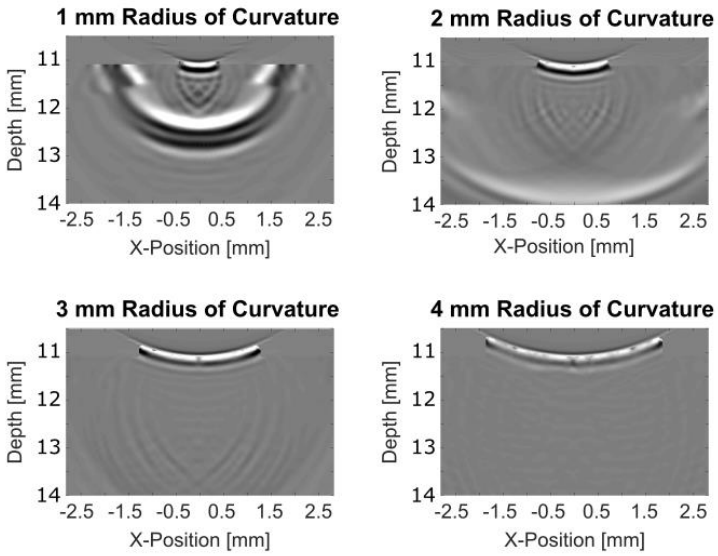


Figure 51 – A comparison of the physical artifacts resulting from the reconstruction of simulated data. In the upper left image, we see a banding along the middle portion of the image due to reflections from the upper surface being remapped to the subsurface. The upper portion of this band shows a discontinuity as the grating lobe switches to the dominant solution. The final defect, near the upper boundary, results from the sharp drop-offs that are inherent to ray theory about caustics. This effect is also present in other images but drops off drastically as the radius increases.

### *7.3. Comparison to Physical Samples*

In comparing to physical samples, the primary difference between the model results and those of physical samples is the presence of shear waves in the physical specimen. The presence of shear waves is expected to result in some artifacts in the imaging process; however, these artifacts are reduced due to the

different sound speed between these wave modalities. During the focusing process, the shear wave's appearance becomes notable only if the phases align in a manner under which constructive interference results.

In theory, the presence of shear waves can be exploited for the use of imaging by changing the focal laws such that they correspond to these propagation modalities. Although shear waves were developed in the modelling capabilities, the exploration of these waves cannot be employed using the current method. This occurs due to the inability of the probe to detect boundaries with a high degree of curvature. As shear waves are only of notable amplitude at higher angles of incidence, the inability to detect a surface at these angles makes imaging all but impossible. In this section, we look primarily to the samples inspected to test the viability of ignoring these shear waves in the reconstruction process. In this case, the physical phantom and simulation are compared directly, with attempts made to minimize any positioning and alignment errors. In order to maximize the similarity to the simulation, the phantoms were scanned using the flat transducer, for which an approximation of a 2D imaging system can be considered valid.

In the defect-free sample, a measurement of the expected noise level due to the grain structure of the bronze material was explored. The deviation is expected between the grain reflections in each sample; however, the intensity of these reflections should be of a similar level. In comparison, the simulated model completely lacks this noise. In the case of shear waves, as no reflectors are

present in the imaged region, and water does not support shear wave propagation, no additional reflections are noted.

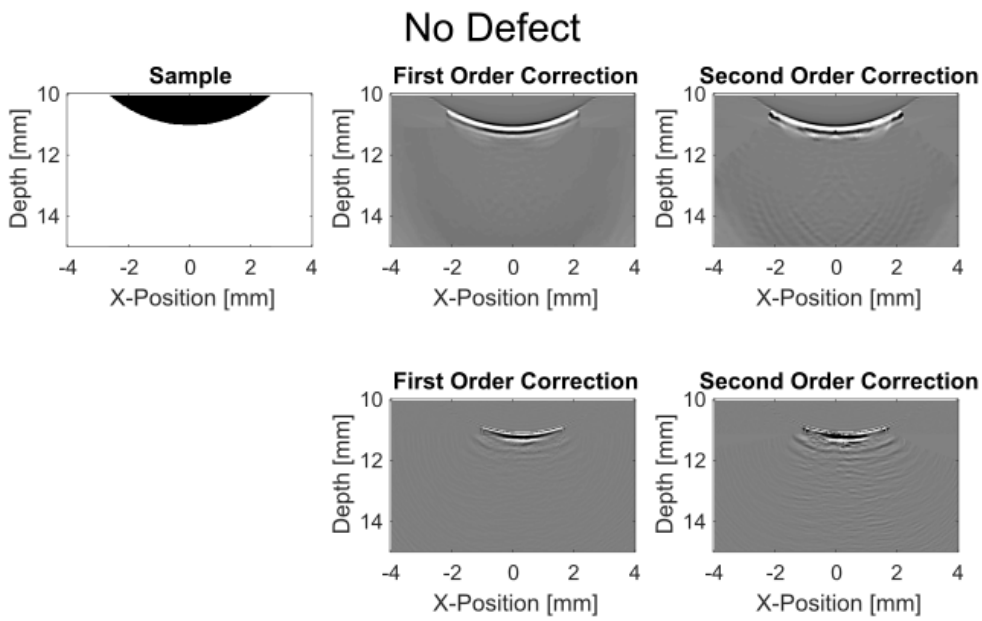


Figure 52 – A depiction of the idealized surface in both simulation (top) and real samples (bottom) for the case of no subsurface reflectors. The upper boundary is noted to have a slight subsurface reflection due to the pulse length of the transducer. No shear waves are expected in this image due to water being used as a coupling medium.

In the case of a convex bottom sample, we note multiple echoes present due to the ignorance of the interaction between these surfaces in the employed Hamiltonian. After the first echo, we also note an additional signal present in the real sample that is absent from the simulated results. As the sound speed in brass is noted to be approximately 4890 m/s and 2100 m/s for shear and longitudinal waves respectively, the position of the additional reflection is in the region corresponding to the shear wave. This effect, shown in

Figure 53, is noted to be present after the initial reflection, meaning that such reflections would not affect the ability to make a quality determination in any brazed joint. In addition to the additional reflections, it is noted that the presence of multiple echoes is present. This effect occurs due to the exclusion of the sub surface reflector from the propagation model.

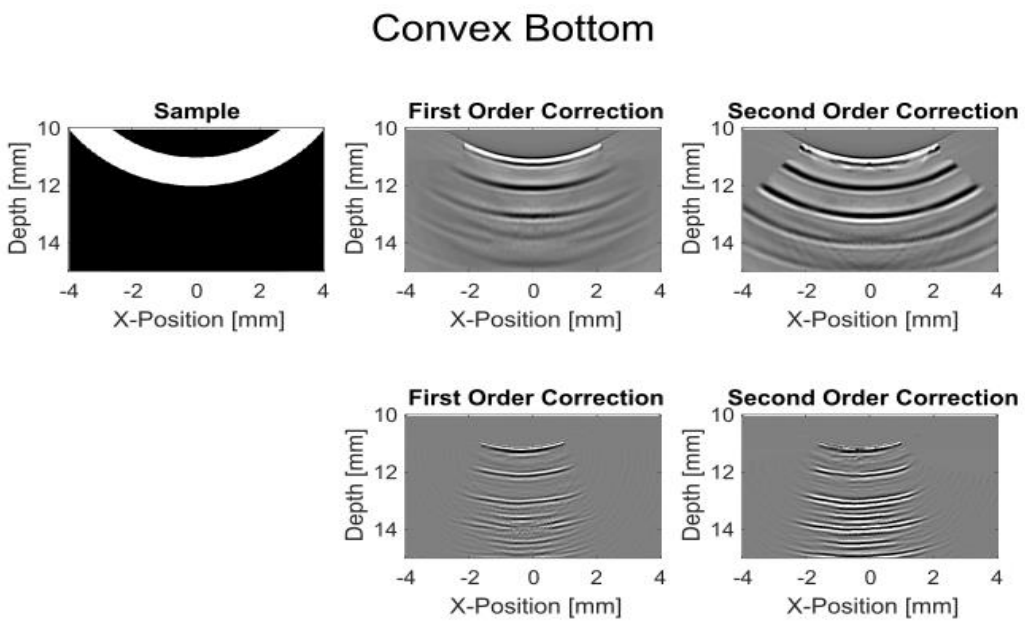


Figure 53 – An image of the reconstruction results for the convex bottom sample in simulation (top) and experimental (bottom) measurements. In this case, the presence of a shear wave reflection is noted after the secondary echo from the surface. This artifact is, however, outside of the area of interest and is not expected to affect imaging results.

Such an effect was not noted in the case of the convex bottom surface as well. In this case, the surfaces result in a divergence of the echoes between them, with the amplitude of the wave decaying notably. This change in the symmetry results in the shear wave reflection being remapped perpendicularly to the boundary. These additional reflections were again after the primary reflection, meaning that

they would also have minimal impact on the inspection process. The amplitude of these reflections was also found to improve when employing second-order corrections, becoming negligible in amplitude with respect to the desired reflection.

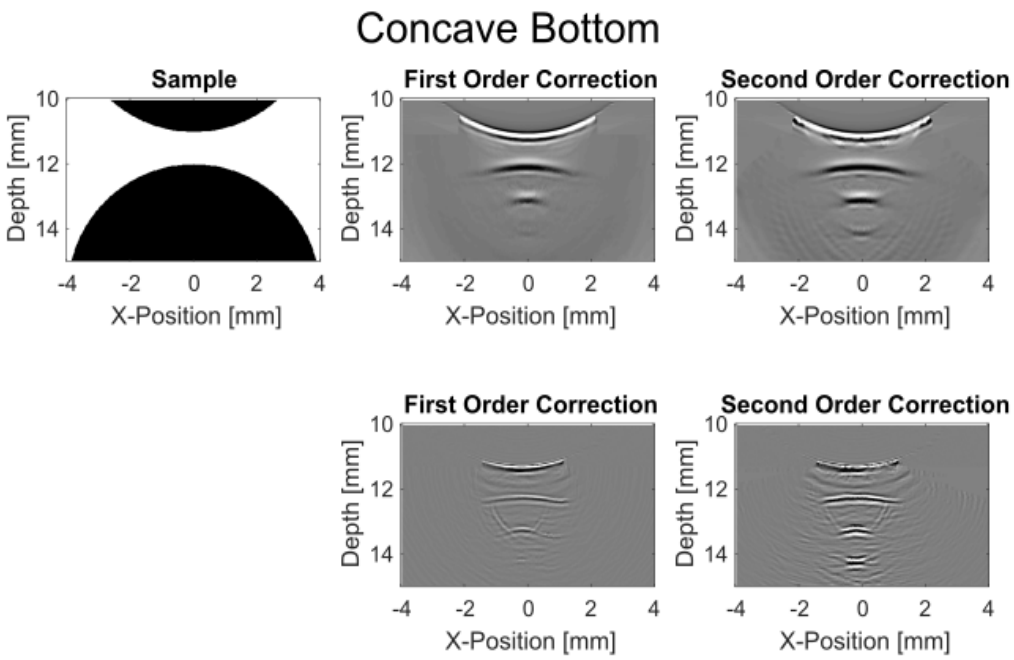


Figure 54 – An image of the reconstruction results for the concave bottom sample in simulation (top) and experimental (bottom) measurements. In this case, the presence of a shear wave reflection is noted more in the real sample when first-order corrections are used.

In all other cases, the presence of shear waves was not noted within the image. In the pore, this is expected due to the much smaller radius of the pore, resulting in any reflected shear waves being weaker than the case of the concave bottom. Such an effect is also seen in the sample depicting the bottom crack. In the case of the lack of adhesion sample, the shear wave will propagate at a differing angle in accordance with Snell's law.  This results in a lack of coherence when mapped with respect to the longitudinal wave path. These reconstructions, shown in

Figure 54, Figure 55 and Figure 56, demonstrate that most defects will not form appreciable shear waves under imaging. In addition to the lack of shear waves, it is noted that physical samples were found to be far more likely to meet the threshold of detection when second-order corrections were applied. In many cases, first-order corrections resulted in a defect amplitude comparable to the noise level of the sample.

In general, it was found that although shear waves can be present in an image, they often occur either outside of the area of interest or at a negligible amplitude with respect to the primary reflector. As a result of this analysis, they are primarily ignored in the next chapter, where physical joints are inspected.

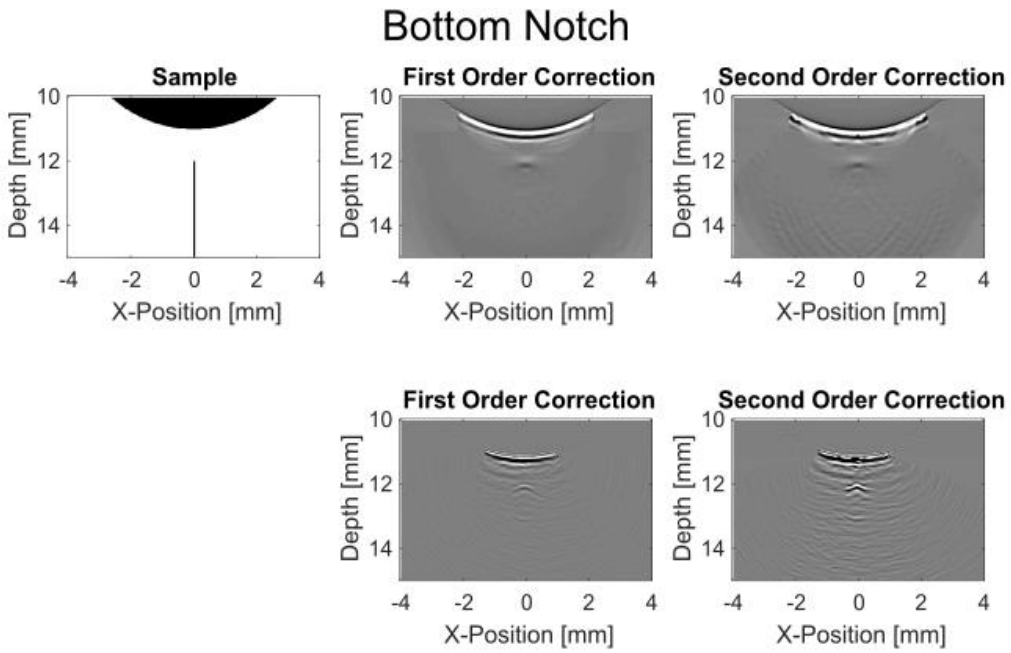


Figure 55 – An image of the reconstruction results for the bottom notch sample in simulation (top) and experimental (bottom) measurements. In this case, the presence of a shear wave reflection is not noted. The primary deviation from the simualted results is the higher reflection from the inner notch caused by its increase in size over the simulation results.

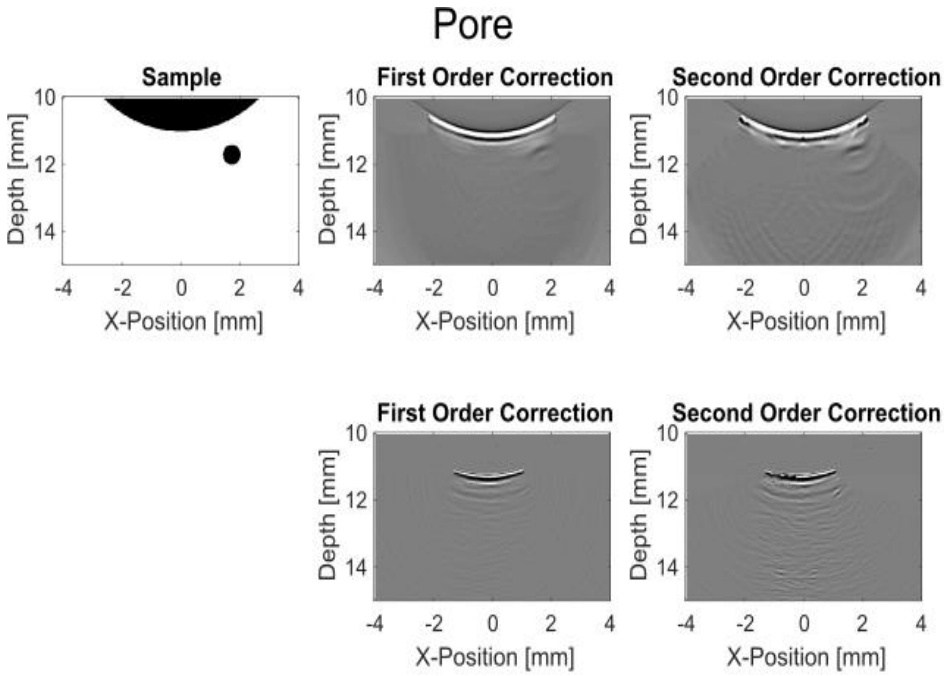


Figure 56 – An image of the reconstruction results for the sample with a simulated pore in simulation (top) and experimental (bottom) measurements. In this case, no shear waves are noted; however, the pore visibility is affected by its location. Rotations of the transducer can alleviate this effect.

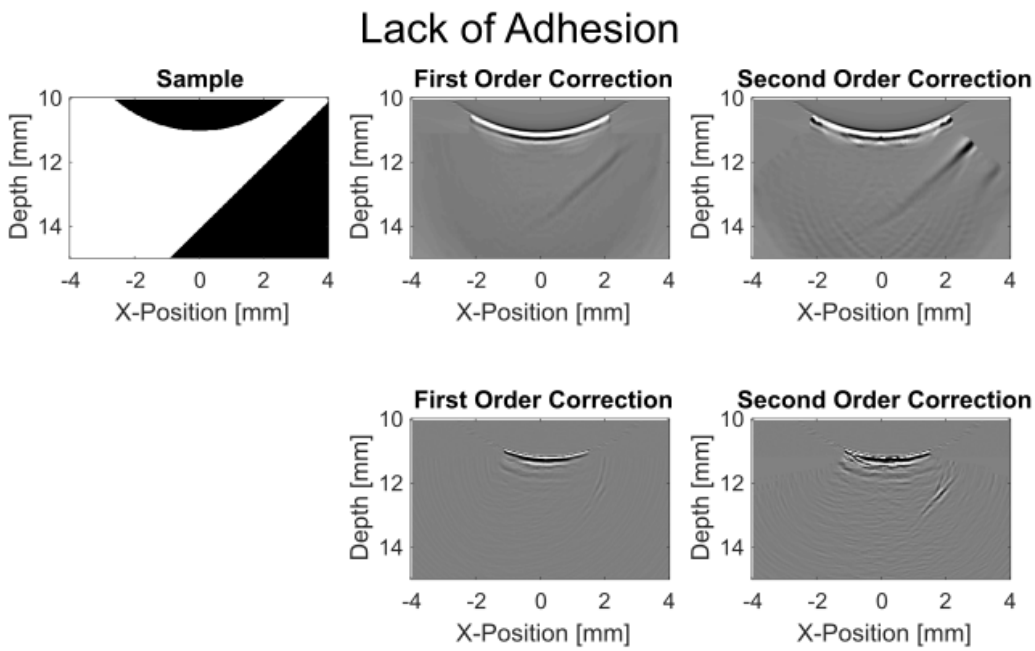


Figure 57– An image of the reconstruction results for the lack of adhesion sample in simulation (top) and experimental (bottom) measurements. Although no shear wave is found to be visible, it is noted that in the case of first-order corrections, the boundary was below the threshold of visibility. Second-order corrections allow for some visualization with a decreased visibility as the depth increases due to the angular aperture of the upper boundary.

### *7.4. Imaging Subsurface Defects and the Influence of Radius of Curvature*

In order to access the viability of subsurface imaging for a range of curvatures, this section outlines the change in visibility of each defect as the upper surface curvature varies. This section acts to compare the imaging ability of the proposed second-order corrections to those of the first-order for various curvatures, yielding some insight into the transitional point where the proposed technique offers a significant advantage over more traditional imaging techniques. As the proposed technique has a notable computational overhead associated with it, this can also be used to accelerate the processing in the future.

In the case of a pore, the second-order corrections offer a significant advantage as the radius of curvature drops below 3 mm, offering almost no benefit at the radius of 4 mm. These variations, seen in Figure 58, is, of course, limited to a specific region of the image and do not show a more complete picture.

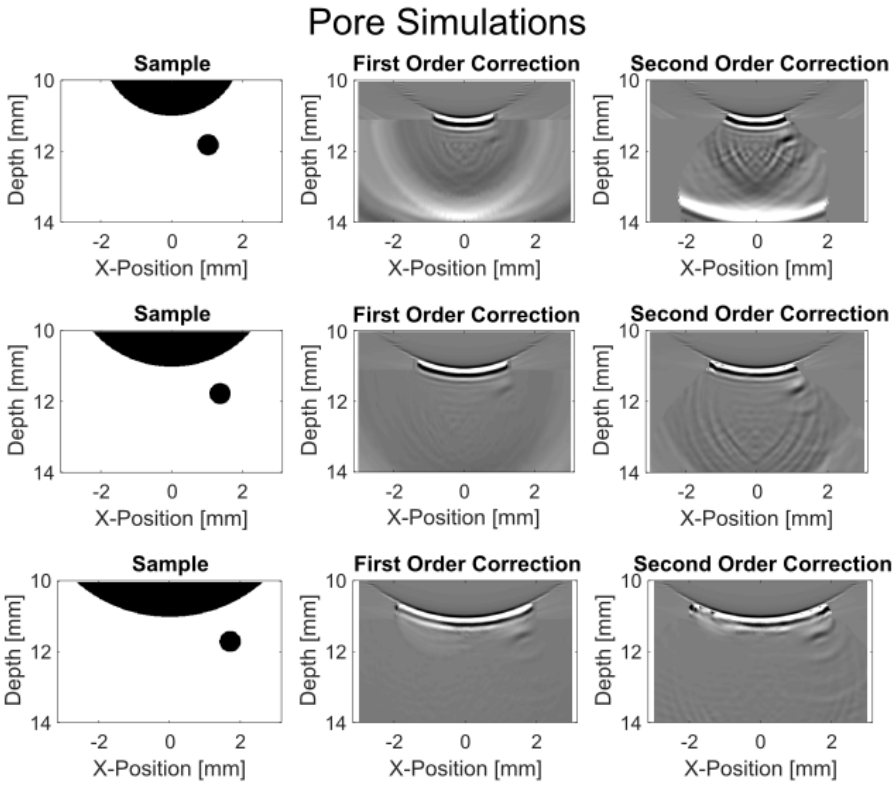


Figure 58 – A depiction of the simulated results for pore imaging at various radii of curvature for the upper surface. In each case, the pore is found to be visible. At 2 mm, second-order corrections do improve the amplitude of the pore; however, they also increase deterministic noise in the image.

In the case of a lack of adhesion, the imaging was found to improve somewhat in the lateral direction in all cases, making the defect more visible than the traditional technique. In the case of a 1 mm and 2 mm radius, the side lobe presence results in a curvature being added into the image in the upper right corner. This defect, which poses some issue, was found to be further suppressed

through the change in the threshold of the normalization amplitude; however, its presence here does pose a limitation in detecting defects at these large angles. This is expected to be improved by scanning at differing angles, as discussed in the further work section.

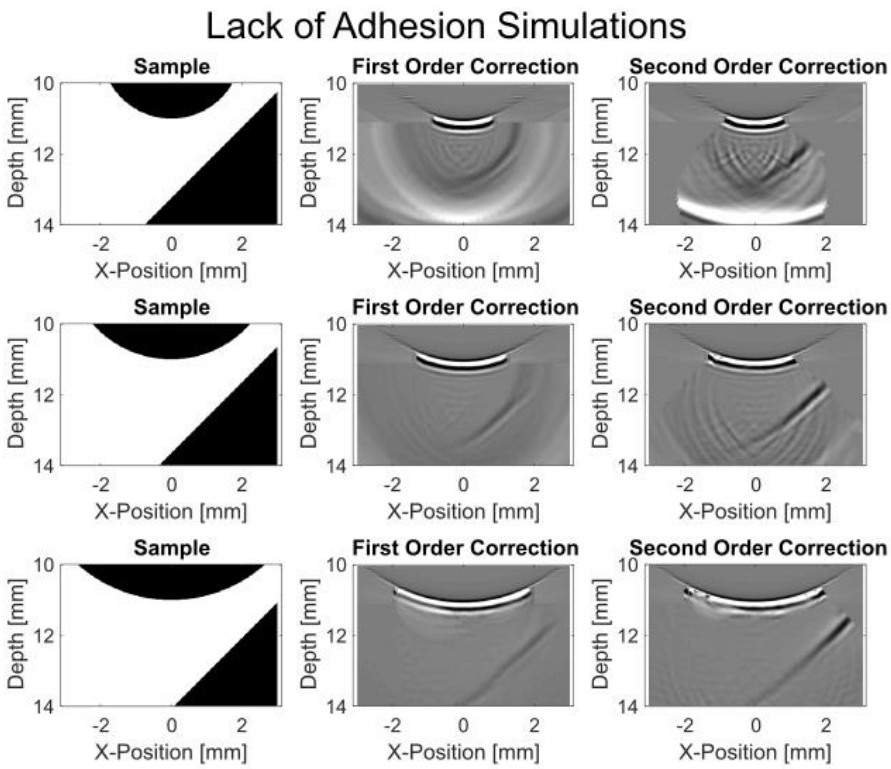


Figure 59– A depiction of the simulated results for lack of adhesion at various radii of curvature for the upper surface. In each case, the sloped surface is visible, with a slight increase in the visibility at greater depths using second-order corrections.

In the convex bottom simulations, the increase in the visibility of the bottom surface as the imaging angle increases shows the key benefit of second-order corrections, with the technique offering a distinct advantage in almost all cases. It is noted that in the case of 4 mm curvature, the benefits once again decrease, showing a key transition between these two radii. These effects, shown in Figure

60, were also found to be reflected in the case of the concave bottom surface detailed in Figure 61.

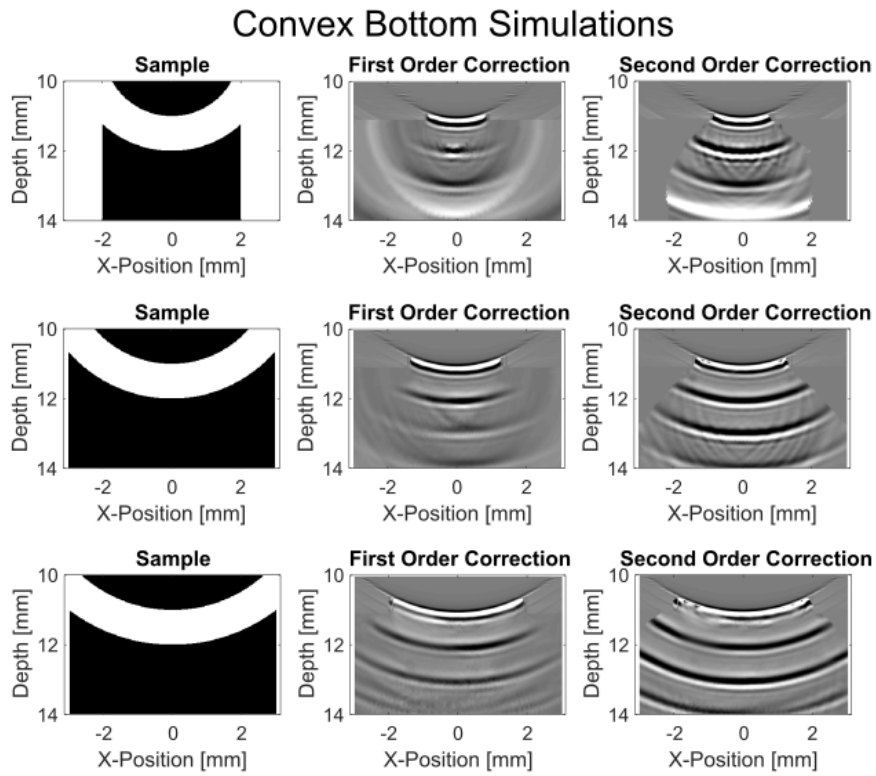


Figure 60– A depiction of the results for the convex bottom at various radii of curvature. In the case of the convex bottom surface, the surface was found to be visible in most cases; however, at higher angles, the visibility was improved by applying second-order corrections.

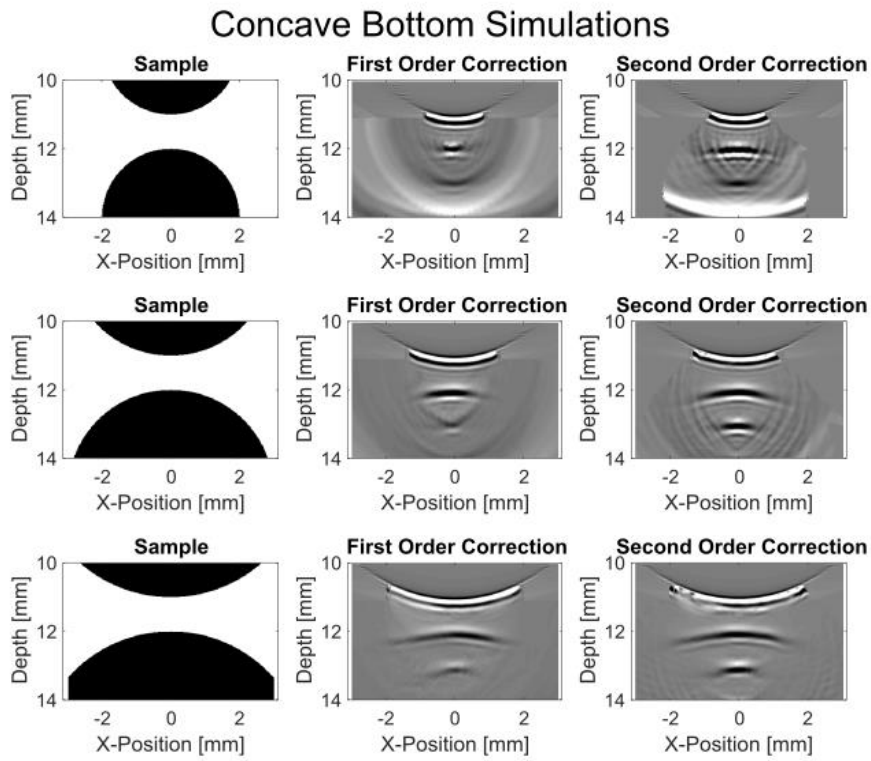


Figure 61 - A depiction of the simulated results for the concave bottom at various radii of curvature for the upper surface. For the case of a concave bottom surface, the surface was found to be visible in most cases; however, at higher angles, the visibility was improved by applying second-order corrections.

In the case of the bottom notch, the location of the defect being central to the surface shows that the second-order techniques offer less benefit in the imaging of idealized reflectors in this region. Although some increase in the visibility was found at the 2 mm radius, the lack of any other reflectors within the image makes analysis and identification possible in all cases using either first or second-order techniques.

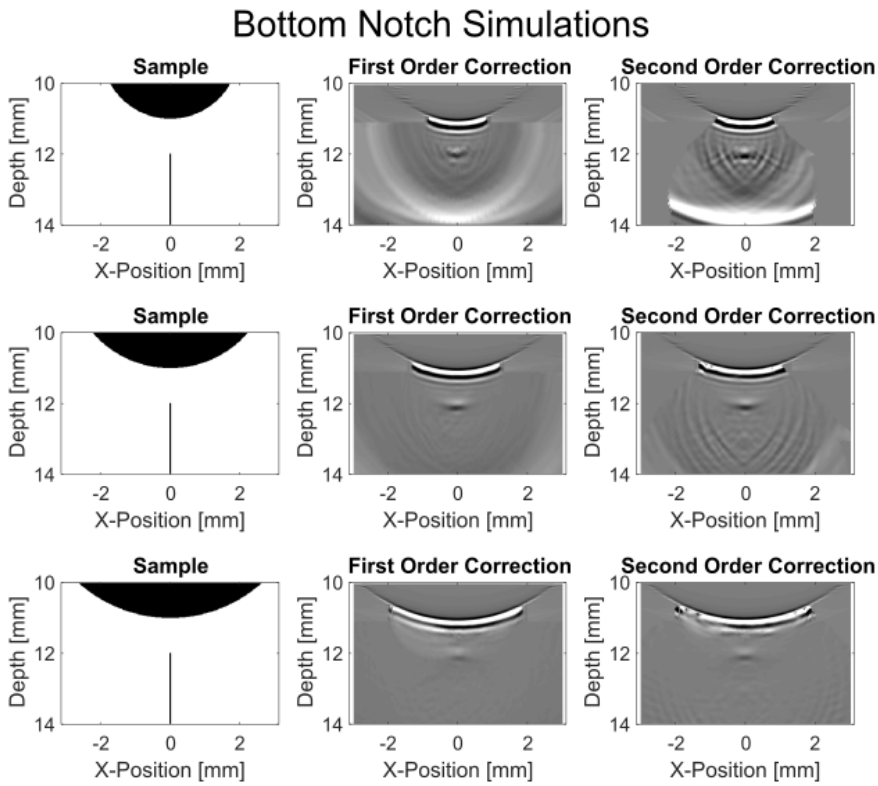


Figure 62 - A depiction of the simulated results for bottom notch phantom at various radii of curvature for the upper surface. For the case of the bottom notch, the visibility was found to be fairly consistent between first and second-order corrections. This can be explained due to the location of the defect being at the center of the image.

### *7.5. Conclusion*

Based on the samples inspected in this section, the implementation of second-order corrections was found to offer beneficial results as the radius of curvature dropped below the 3 mm mark. Despite these benefits, the imaging of samples with a radius of curvature approaching 1 mm was found to be impossible using first or second-order corrections. These limitations, which are inherent of the high-frequency approximation used in current imaging systems, set a

fundamental limit in the ultrasound imaging field given current limitations of transducer manufacturing.

The imaging of smaller radii also presents the potential for side lobes to cause artifacts in the imaging process. This effect, caused by the limited visibility of the upper surface, can be corrected by scanning at a differing angle where side lobes will not be present in this region.

# Chapter 8

# Imaging of Braze Samples

In the early stages of this work, imaging resulted in mixed success. This was due to the use of first-order corrections, and the use of transducers whose designs formed an insufficient basis in terms of size and pitch of the elements. Despite these early limitations, the early success of imaging specific physical samples, combined with the results of simulations, allowed for the acquisition of the equipment used in this work. In this chapter, we primarily assess the capabilities of the current system, rather than these early results, to accurately reflect the capability of ultrasound in the assessment of laser brazed joints. These results demonstrate the significant progress made in imaging of laser brazed joints through the upper surface.

This chapter makes use of two comparative methods for assessing the quality of ultrasonic images, mainly CT imaging and cross-sectional analysis. CT images were found to offer a much better analysis tool due to its higher accuracy in the inactive imaging direction. Using this, the detection of pores and other defects in which span fractions of a millimetre can be performed. Cross sectioning, although cheaper, has the disadvantage of both destroying the sample in the area and having a resolution of a few mm in the inactive direction.

## *8.1. Early Imaging of Braze Samples*

Early scanning of brazing samples with the original equipment was found to be inadequate for a variety of reasons. In this early work, the use of a 32 element, 0.25 mm pitch array with an unfocused elevation was explored. Here, the use of

a larger pitch resulted in poor steering angles, with artifacts being present in even idealized imaging cases due to inadequate sampling. This lack of steering, show in Figure 63, also resulted in inadequate subsurface imaging in the majority of samples. The use of an array with a smaller pitch did improve the results[80]; however, this array had a relatively small effective imaging area and could not visualize the outer geometry as a result. Reprocessing of such results with second-order techniques, which were not implemented at the time, did show improvement in the image quality, although not to the degree desired. Due to this, subsequent sections shall make use of the redesigned probe with data being required on a similar joint.

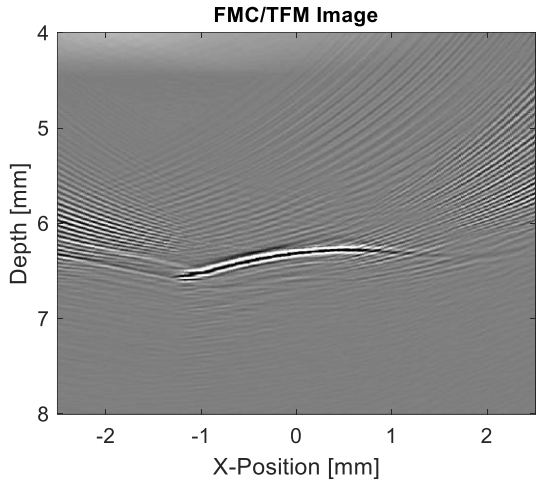


Figure 63 – A depiction of the early scans performed with an unoptimized transducer. In this case, only the upper braze surface is visible, with the steel plates not being seen within the imaged region.

### *8.2. Imaging of Braze Specimens*

In order to assess the imaging ability of the final system, samples were manufactured at our partner's facilities using two plates arranged in the flare at V-groove arrangement. These samples were manufactured in a manner intended

to produce particular defects; however, CT scanning showed them to contain a variety of defects rather than a singular type. Although the highly curved nature of the joints made imaging difficult, the geometry afforded the ability to encode the scan along the length of the braze using a translation stage and submerging the sample and transducer in water. This allowed for a comparison to x-ray CT slices/images along the length of the braze. Due to the expense of the CT images, the acquisition of CT data sets was limited; however, all defects outside of cracks and melting of the base metal were detected in the acquired CT data.

From the x-ray CT data, one principle issue in imaging was found. Although the upper surface was found to be fairly consistent, the bottom surface of the braze was found to vary significantly over short distances in some regions. In others, the bottom surface exhibited a notable slant, which reduces the visibility of the second boundary. These variabilities, seen in Figure 64, show some issues with the intended scanning technique in that the measure of a single point, through ultrasonic means or cross-section, may be insufficient to indicate the quality of the joint. In addition, the proposed transducer produces a focal point of approximately 1.5 mm in bronze, meaning that many images contain defects from multiple sections of the joint. Luckily, as the bottom surface did not vary widely enough to result in completely destructive interference, usable images were found along the majority of the joint.

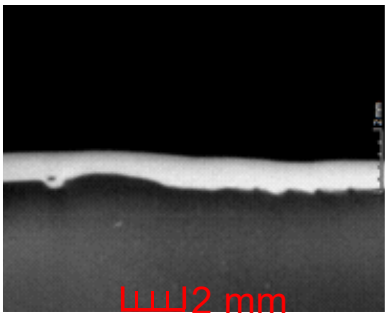


Figure 64 – An X-ray CT of the braze bottom surface. The high level of variations along the bottom surface makes imaging difficult. In the case of a flat transducer, averaging over large regions can result in poor image quality.

In the imaging of this sample, the results were drastically improved, yet still insufficient in some areas. In each case, the imaging results managed to detect most defects within the sample; however, limitations to the imaging resolution make discerning and identifying defects difficult. When imaging these samples, using first-order corrections was found to be completely unviable in most regions, with no visible subsurface defects or boundaries detected. The radius of curvature of the sample was often in the 2 mm range, where second-order corrections are found to dominate. As a comparative example, Figure 65 shows the comparison between first and second-order corrections on a sample with a radius of curvature of approximately 1.5 mm. In this case, second-order corrections were found necessary to generate a usable image. In the case of second-order corrections, the bottom surface of the braze sample was found to be of a notably higher contrast as compared to first-order corrections, where a notable spreading of this reflection is present. This result shows the increase in resolution second-order techniques provide.

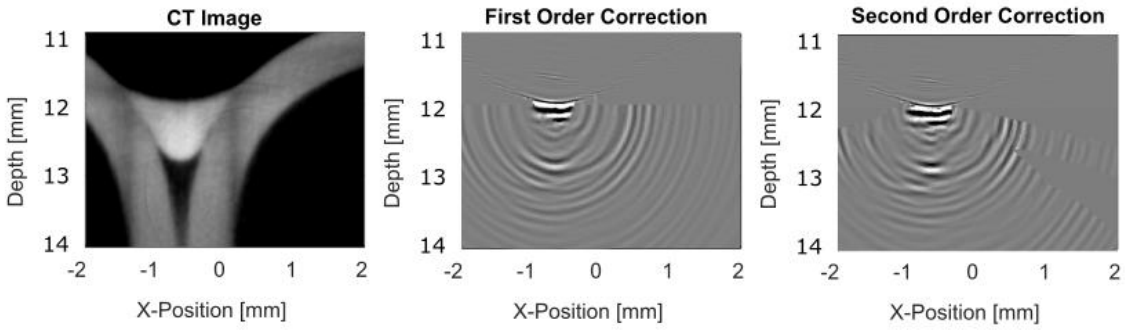


Figure 65 – A depiction of first and second-order corrections in the imaging process. It is notable that for a sample with a smaller radius of curvature, the second-order techniques reduce the spatial spread of the bottom surface reflection. Some banding still exists on the right side of the image due to the decreased angular aperture.

When comparing ultrasonic images to CT images, most defects were detectable; however, in the case of lack of adhesion, such as shown in Figure 66, the reflection from the upper tip of the unadhered area shows a similarity to the reflection from a pore, such as seen in Figure 67. These similarities show one disadvantage of ultrasonic techniques in that the impedance change caused by the defects results in a similar reflection, with the defect only being characterizable by its geometry. It is notable that current characterization techniques[47,53,81] are expected to fail in these cases due to the self-focusing effect of the surface, which prevents the extraction of directivity as a single element may exhibit an omnidirectional field.

Some characterization may be possible through the visibility of the sub-surface, as pores tend to be of limited size along the inactive direction, whereas lack of adhesion which spans a larger length of the sample. One notable deviation from the phantoms explored in the previous chapter is the absence of the banding effects in the image. These subsurface reflections, which occur from

reverberations due to the internal geometry of the surface were eliminated as the surface arc angle was decreased.

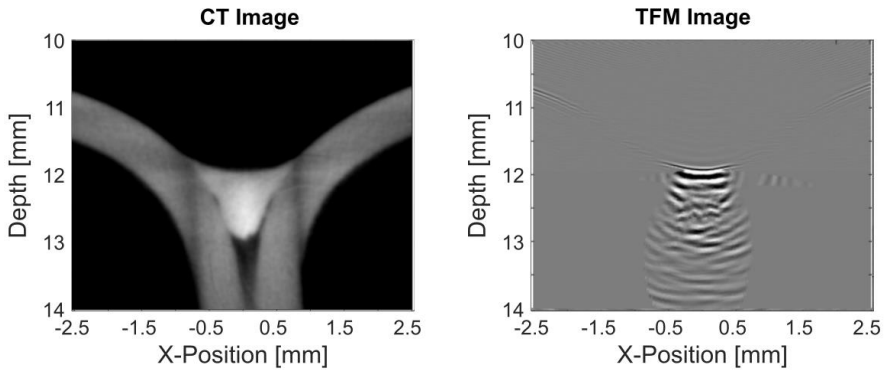


Figure 66 – A depiction of the second-order corrected image for a region with multiple defects present. Here, the overlapping defects result in an image that is very poor, with no visible subsurface. In such cases, the sample would be considered defective.

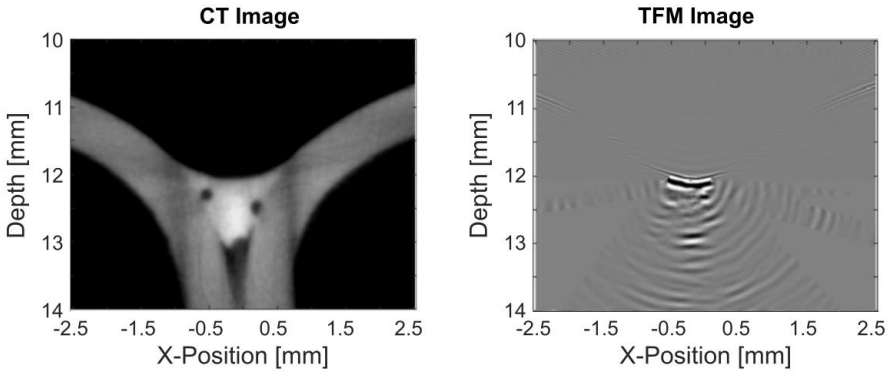


Figure 67 – A depiction of pores in a sample. Here, regions without pores do not block the ultrasound signal, making both the pores and lower boundary present at the same time due to averaging along the inactive direction.

In regions with a lower radius of curvature, such as seen in Figure 68, more characteristics of the braze, such as the bottom surface profile, and the presence of a lack of adhesion in the sample on the left side, were visible. Unfortunately, a larger than desirable beam spot size in the inactive direction resulted in additional, weaker reflections from other areas of the sample. In regions with a

low number of defects, the joint measurement was found to be possible with the leg length and throat thickness comparable to those of CT images. Despite this success, other samples, whose geometry may better represent real parts, were inspected to determine the wider applicability of the proposed system.

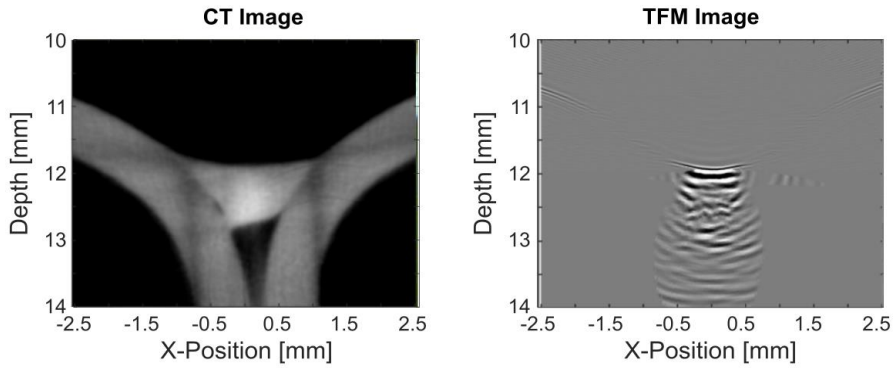


Figure 68 – A depiction of a region with a small lack of adhesion, shown as a secondary reflection coming off of the bottom surface reflection.

### *8.3. Measuring Joint Geometry*

To assess the ability of the system to determine joint geometry on a wider section of samples, imaging was conducted on a series of samples with differing geometries. These parts, representative of the final samples, provide a wider variety of geometries than in the samples containing defects. Although numerous images were acquired in the past, they were repeated with the newly acquired probe, which significantly reduced artifacts and improved imaging of both the upper and sub-surface. Although the use of a 6 axes stage has been employed in the past to optimize imaging, the results presented here use a more plant-friendly implementation that was designed as part of this work.

In a lab setting, submersion of smaller sections in a water tank is possible; however, in a plant environment, the submersion, scanning, and drying of large

parts make such an inspection technique impractical. Establishing a column of water using a pump or other means is also problematic due to the constant loss of water and the special environments needed to manage this. The desired implementation was determined to be simple to deploy, easy to clean and relatively low cost.

With this in mind, the use of a commercial delay line was explored. Most commercial delay lines make use of rubbers that highly attenuate ultrasound at higher frequencies, often limiting the use to frequencies below 5 MHz. One candidate that was found viable in this project was a solid gel delay line. This commercial delay line, distributed by the brand name Aquaflex, has a speed of sound of 1600 and a density of 1 kg/m^3, making it similar to water and water-based ultrasound gels. Due to this similarity, the use of a water-based coupling gel to fill the gap was found to produce no reflections or aberrations when imaging. This sound speed difference of approximately 8% also allows for direct comparison to water, which is easier to employ in lab settings as it requires no cleaning of the surface.

The secondary issue that was encountered was the alignment of the probe with the braze sample. Depending on the orientation of the defect, the angle of the probe with respect to the surface may increase the visibility of this subsurface feature. In addition to this, the alignment of the probe with the sample proved problematic without the use of a stage as both angle, position and orientation in the inactive direction must be maintained. To overcome this, an external housing was designed. This housing serves two purposes: firstly, it can be used to hold

an Aquaflex delay line to the transducer, and secondly, the use of pins allows for the alignment of the probe with respect to the braze. As the transducer is physically inserted into the housing, the use of pins also allows for the fixing of the transducer distance from the surface of the braze, even if the angle is changed. This housing, shown in Figure 69, serves primarily as a reference design, with eventual plans to replace pins with a safer option and reduce the overall housing design to allow clearance at higher angles of rotation. In use, images were found to be easily obtained, with only minor adjustments to the placement required to properly orient the surface of the sample with the probe. Given that surface imaging, which uses analytic delay laws, can be done in real-time the alignment procedure is fairly simple when using such a housing.

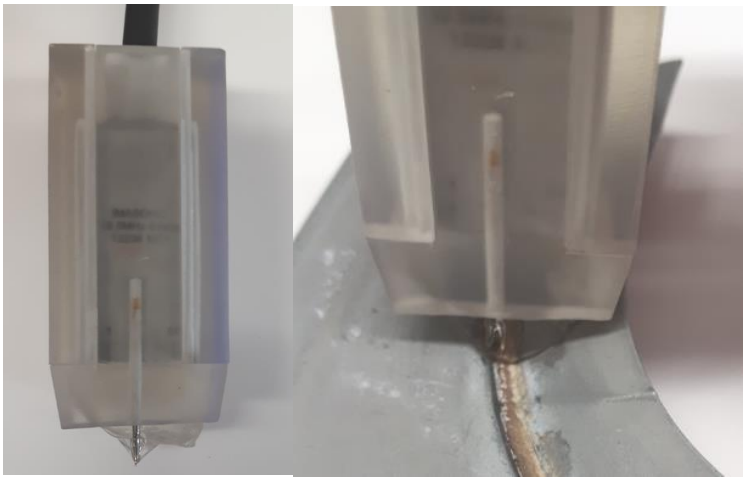

Figure 69 – A depiction of the current probe enclosure in use, the probe is encased in a 3D printed housing, with pins set to keep the probe at a fixed orientation and distance with respect to the sample. An aqua flex delay line is used with a small amount of gel to prevent the formation of air pockets with the surface.

In addition to the alignment, the imaging of a more arbitrary surface poses a problem in that the detection of the surface cannot be automated. In this work,

the use of a user-defined area of interest was incorporated into the boundary detection program to eliminate points that are not on the braze surface. As the reflections from both steel and bronze are of similar amplitude, this process requires some user knowledge about the geometry of the sample; however, as the upper surface is visible, this is not expected to cause issues in a plant environment. Despite the relative success, in some scans, the automated detection picked up points due to artifacts where the steel and brass reflections overlap. Currently, others in our group are researching methods to reduce these artifacts, as their presence can corrupt the image as rapid jumps are an eigenvalue solution due to the similarity to a physical point source.

When imaging these samples, which better resemble geometries expected in the automotive assembly, many samples were found to be of a much lower radius of curvature than present in the samples designed to have defects. As a result, geometry estimations were found to be possible in a variety of joints and, in some cases, without using second-order corrections. These measurements, shown in Figure 70 and Figure 71, can be compared to cross-sections in a region close to the scan area. It is notable that the bottom surface reflection was found to be visible even when the braze pool almost completely closes the gap.

The primary artifact found in these images occurs due to the reflection from the steel plates being incorrectly mapped. This results from the sound speed difference between bronze and steel resulting in reflections being remapped closer to the surface. As the impedance mismatch between bronze and steel is approximately two orders of magnitude less than that between water and bonze,

no internal reflections from the bronze steel boundary are detected. As a result, some defects, such as the melting of the base metal, cannot be seen ultrasonically.

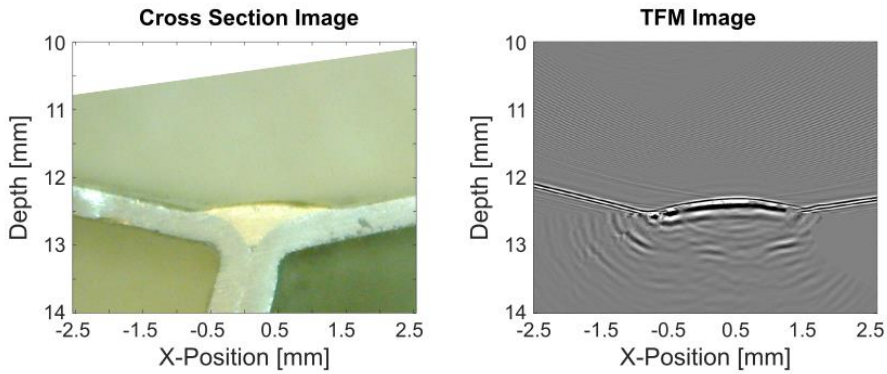


Figure 70 – A depiction of the subsurface of a sample from a representative part. Here, we compare a cross-section of the joint at the area ultrasound data was acquired. The lower gap of the braze can be seen alongside reflections from the steel plate.

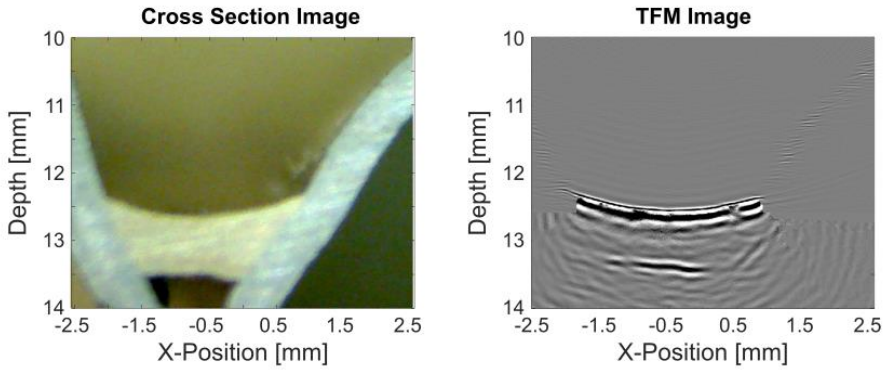


Figure 71 – A depiction of the subsurface image of a sample from a representative part. Here, we compare a cross-section of the joint at the area ultrasound data was acquired. The lower boundary reflection is present; however, some bleeding of the reflections from the steel plate does blend in with this lower surface.

In addition to direct images of the sample, some scans were acquired by rotating the transducer using the pins as a guide. This method can also allow for the visualization of geometric features that were not previously visible or to enhance

the visibility of inner surfaces, as seen in Figure 72. Here, scanning of the same sample as in Figure 71 allows for a much clearer discerning of the boundaries within the image. The reflections that blurred together when the sample was imaged at a single angle can now be distinctly differentiated. It is expected that in some geometries, the rotation of the transducer may be performed to verify the defect in question, as has been shown from scanning the bronze samples. This scanning arrangement, although useful, is still limited by the clearance of the housing, with more optimized designs expected to be produced in the future.

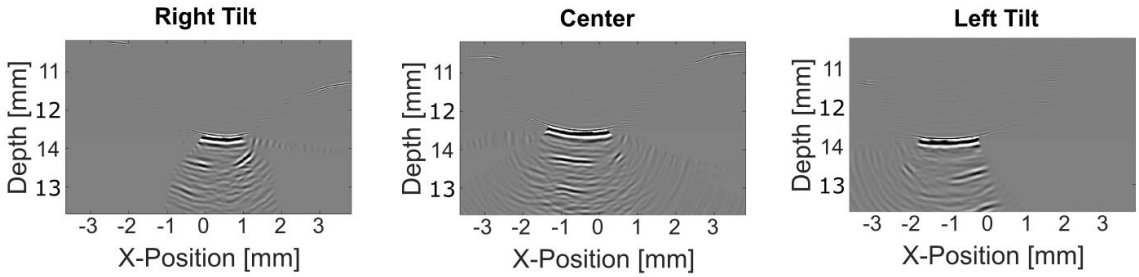


Figure 72 - A depiction of the same sample as in Figure 71. Here the probe is rotated at differing angles of approximately 15 degrees. These rotations change the visibility of sub-surfaces, allowing for the separation of the steel plate reflections from the bottom surface reflections.

### *8.4. Conclusions*

In this chapter, we analyzed the imaging ability of the probe on real braze samples. It was found that the results show the possibility of detecting joint geometry, pores and lack of adhesion; however, identifying and characterizing the defects are not always possible in cases where the radius of curvature decreases. In cases where the geometry is approaching a flat surface, a higher level of characterization is expected to be possible as evident from the increased visibility of features in acquired images. The design of a prototype system for scanning real specimens was undertaken and proved a viable option for

scanning outside of lab environments. This housing was also found to allow for imaging at various angles, which improves the image quality in regions where the surface geometry and probe limitations prevent imaging.

# Chapter 9

## Conclusion and Future Work

In this work, a new method of imaging based on the second-order ray series expansion and a first-order approximation to the inverse imaging problem was proposed. The derivation of the technique was presented using a change of basis notation. Using this and the Lagrange formalism, the introduction of a physically interpretable normalization factor results alongside a physical meaning for the apodization or weighting factor used in many imaging techniques. This technique was shown to be equivalent to the current methods through further simplifications and offers numerous opportunities for future work as more complicated wave models become applicable to real-time.

With the purpose of imaging laser brazed samples in mind, the development of an optimized transducer, alongside a housing and coupling method for use in a plant environment was performed. The development of code for the acquisition, simulation and processing of ultrasonic data was completed using a computationally efficient implementation, allowing for testing of the device on a wide range of samples. A number of samples, simulating both real and idealized geometries and defects were explored, with the results showing that imaging of the brazed joint should be possible in many cases. It was further determined that although defects can not be characterized in all cases, the current inspection method is capable of detecting the majority of defects outside of the melting of the base metal and cracking.

Using this system, an explanation for the limitation of imaging in the case of high surface curvature has also been explored. It was found that in cases of high curvature, the surface acts as an additional aperture within the system, limiting the depth at which imaging can occur as the radius of curvature increases. This, coupled with the assumption of the smoothly varying surface as formulated in the ray series expansion, describes the breakdown of imaging as the curvature approached the wavelength of the transducer. In addition, the use of a weighted summation with a normalization process was shown to enhance the imaging of curved surfaces, providing a significant increase in image quality as the radius decreases.

Although these results show the great potential for characterizing the brazed joint, there still exist many improvements that can be made to the system. In the imaging algorithm, an efficient numerical model was chosen due to the time constraints of the inspection process. As computational hardware improves, more accurate techniques may become viable for the imaging process, further improving the inspection. As the current model relies on the determination of the Hamiltonian of the system, further improvements can be made to the detection of boundaries, including automated separation of the braze pool from the steel. Additional reconstruction improvements can be made by using iterative techniques and simulating the interactions of sub-surface reflectors. The current implementation also relies on the use of MATLAB to implement the various routines. Although some areas of the code perform well, the use of a compiled language offers many possibilities for improved performance.

To the acquisition hardware, improvements can be made to the housing design, removing the use of steel pins and replacing them with safer alternatives. In addition, the housing can be modified to allow for higher accessibility in some regions where rotation is currently not possible due to clearance issues. Due to cost constraints, the exploration of multiplexed hardware, which offers a significantly lower cost of implementation may be explored. Finally, technological improvements to the transducer manufacturing process may allow for the exploration of frequencies above those used in this work.

Due to the limited sample set, and the cost of comparative techniques needed to verify defect presence, a large scale assessment of the applicability to production geometries could not be explored. The acquisition of production parts, with verified geometries, provides the opportunity to perform such an assessment. If sufficient samples can be acquired, it may also be possible to automate the analysis process using image processing techniques, or even artificial intelligence.

Other components of the project, including the design of a user-friendly interface, acquisition of portable processing hardware, such as a laptop with dedicated graphics hardware, and many other minor steps must still be undertaken. These areas, scheduled for the coming year, will allow for the assessment of the system in a more industrial environment, where portability and ease of use become important.

Although many improvements, both minor and major, can be made in the future, this work has shown that the inspection of the laser brazing process can be performed using existing hardware in an efficient manner. The techniques developed here for high-frequency applications are, of course, directly applicable to other inspection processes, such as welds in wind turbines, pipes and automotive assemblies. These other areas have not been explored in this work but allow for further research avenues as the development of the device reaches a finalized state. This indirect achievement is expected to further increase the value of the research presented here as these avenues are explored.

## REFERENCES/BIBLIOGRAPHY

[1] Mostafa, A., and Medraj, M., 2017, “Binary Phase Diagrams and Thermodynamic Properties of Silicon and Essential Doping Elements (Al, As, B, Bi, Ga, In, N, P, Sb and Tl),” Materials (Basel)., **10**(6).

[2] Hirsch, J., 2011, “Aluminium in Innovative Light-Weight Car Design,” Mater. Trans., **52**(5), pp. 818–824.

[3] Zhang, W. H., Qiu, X. M., Sun, D. Q., and Han, L. J., 2011, “Effects of Resistance Spot Welding Parameters on Microstructures and Mechanical Properties of Dissimilar Material Joints of Galvanised High Strength Steel and Aluminium Alloy,” Sci. Technol. Weld. Join., **16**(2), pp. 153–161.

[4] En, B. S., 2003, “Brazing — Destructive Tests of Brazed Joints EN 12797:2000,” Eur. Stand.

[5] Ouellette, A., Titov, S., Ghaffari, B., Hetrick, E., and Maev, R., 2016, “Non-Destructive Evaluation of Laser Welded Joints in the Automotive Industry,” *ASNT 25th Research Symposium*, New Orleans, LA.

[6] Ellison, K. A., Lowden, P., and Liburdi, J., 1994, “Powder Metallurgy Repair of Turbine Components,” J. Eng. Gas Turbines Power, **116**(1), pp. 237–242.

[7] Makwana, P., Shome, M., Goecke, S. F., and De, A., 2016, “Gas Metal Arc Brazing of Galvannealed Steel Sheets,” Sci. Technol. Weld. Join., **21**(7), pp. 600–606.

[8] Shelyagin, V., Zaitsev, I., Bernatskyi, A., Khaskin, V., Shuba, I., Sydorets, V., and Siora, O., 2019, “Monitoring of Laser Welding Process Using Its Acoustic Emission Signal,” pp. 234–243.

[9] Shevchik, S., Le, Q.-T. T., Meylan, B., and Wasmer, K., 2018, “Acoustic Emission for in Situ Monitoring of Laser Processing,” *33rd European Conference on Acustic Emission Testing*.

[10] Gu, H., and Duley, W. W., 1996, “Resonant Acoustic Emission during Laser Welding of Metals,” J. Phys. D. Appl. Phys., **29**(3), pp. 550–555.

[11] Turner, D. C., 2014, “Three-Dimensional Backscatter X-Ray Imaging • Miniaturization of X-Ray Components,” In-sp. Insp. Work., pp. 1–31.

[12] Vepsäläinen, M., Markkanen, M., and Sundberg, P., 2014, *X-Ray Tomography of Large Objects with Limited Measurement Angle*, Helsinki, Finland.

[13] Le Jeune, L., Robert, S., Dumas, P., Membre, A., and Prada, C., 2015, “Adaptive Ultrasonic Imaging with the Total Focusing Method for Inspection of Complex Components Immersed in Water,” AIP Conf. Proc., **1650**(1), pp. 1037–1046.

[14] Jensen, F. B., Kuperman, W. A., Porter, M. B., and Schmidt, H., 2011, *Computational Ocean Acoustics*, Springer New York, NY.

[15] Kolsky, H., 1964, “Stress Waves in Solids,” J. Sound Vib., **1**(1), pp. 88–110.

[16] Cheng, J., Potter, J. N., Croxford, A. J., and Drinkwater, B. W., 2017, “Monitoring Fatigue Crack Growth Using Nonlinear Ultrasonic Phased Array Imaging,” Smart Mater. Struct., **26**(5).

[17] Baghani, A., Salcudean, S., and Rohling, R., 2009, “Theoretical Limitations of the Elastic Wave Equation Inversion for Tissue Elastography,” J. Acoust. Soc. Am., **126**(3), pp. 1541–1551.

[18] Auld, B. A., and Green, R. E., 1974, “Acoustic Fields and Waves in Solids: Two Volumes,” Phys. Today, **27**(10), pp. 63–64.

[19] Jr, L. W. S., and Sedov, A., 1996, “Reciprocity,” **15**(1), pp. 65–71.

[20] Auld, B. A., 1979, “General Electromechanical Reciprocity Relations Applied to the Calculation of Elastic Wave Scattering Coefficients,” Wave Motion, **1**(1), pp. 3–10.

[21] Fan, C., Caleap, M., Pan, M., and Drinkwater, B. W., 2014, “A Comparison between Ultrasonic Array Beamforming and Super Resolution Imaging Algorithms for Non-Destructive Evaluation,” Ultrasonics, **54**(7), pp. 1842–1850.

[22] F.R.S., L. R., 1899, “XXXIV. On the Transmission of Light through an Atmosphere Containing Small Particles in Suspension, and on the Origin of the Blue of the Sky,” London, Edinburgh, Dublin Philos. Mag. J. Sci., **47**(287), pp. 375–384.

[23] Treeby, B. E., Jaros, J., Rendell, A. P., and Cox, B. T., 2012, “Modeling Nonlinear Ultrasound Propagation in Heterogeneous Media with Power Law

Absorption Using a k -Space Pseudospectral Method," J. Acoust. Soc. Am., **131**(6), pp. 4324–4336.

[24] Firouzi, K., Cox, B., Treeby, B., and Saffari, N., 2011, "A First-order *k* -space Model for Elastic Wave Propagation in Heterogeneous Media.," J. Acoust. Soc. Am., **129**(4), pp. 2611–2611.

[25] Treeby, B. E., and Cox, B. T., 2010, "K-Wave : MATLAB Toolbox for the Simulation and Reconstruction of Photoacoustic Wave Fields," J. Biomed. Opt, **15**(April), pp. 1–12.

[26] Kruth, J. P., Bartscher, M., Carmignato, S., Schmitt, R., De Chiffre, L., and Weckenmann, A., 2011, "Computed Tomography for Dimensional Metrology," CIRP Ann. - Manuf. Technol., **60**(2), pp. 821–842.

[27] Baxley, P., Bucker, H., and Porter, M., 2000, "Comparison of Beam Tracing Algorithms," Proc. Fifth Eur. Conf. Underw. Acoust. ECUA 2000.

[28] Bucker, H. P., 1994, "A Simple 3-D Gaussian Beam Sound Propagation Model for Shallow Water," J. Acoust. Soc. Am., **95**(5), pp. 2437–2440.

[29] Treeby, B., Cox, B., and Jaros, J., 2016, "K-Wave,Manual Version 1.1," **1**.

[30] Weinberg, H., and Keenan, R. E., 1996, "Gaussian Ray Bundles for Modeling High-frequency Propagation Loss under Shallow-water Conditions," J. Acoust. Soc. Am., **100**(3), pp. 1421–1431.

[31] "Vector Form of Snell's Law" [Online]. Available: http://www.starkeffects.com/snells-law-vector.shtml. [Accessed: 15-Nov-2019].

[32] Peters, T., CT Image Reconstruction.

[33] Shankar, R., 1994, “Mathematical Introduction,” *Principles of Quantum Mechanics*, Springer US, Boston, MA, pp. 1–73.

[34] Dirac, P. A. M., 1939, “A New Notation for Quantum Mechanics,” Math. Proc. Cambridge Philos. Soc., **35**(3), pp. 416–418.

[35] Fink, M., 2013, “Time Reversal Mirrors,” 2013 Transducers Eurosensors XXVII 17th Int. Conf. Solid-State Sensors, Actuators Microsystems, TRANSDUCERS EUROSENSORS 2013, **26**, pp. 788–789.

[36] Wu, F., Thomas, J.-L., and Fink, M., 1992, “Time Reversal of Ultrasonic Fields—Part II: Experimental Results,” IEEE Trans. Ultrason. Ferroelectr. Freq. Control, **39**(5).

[37] Fink, M., 1992, “Time Reversal of Ultrasonic Fields. I. Basic Principles.,” IEEE Trans. Ultrason. Ferroelectr. Freq. Control, **39**(5), pp. 555–566.

[38] Fink, M., 1993, “Time-Reversal Mirrors,” J. Phys. D. Appl. Phys., **26**, p. 1333.

[39] Workman, G. L., and Kishoni, D., 2007, *Nondestructive Testing Handbook, Third Edition: Volume 7, Ultrasonic Testing (UT)*, American Society for Nondestructive Testing, Incorporated, Columbus, OH.

[40] Holmes, C., Drinkwater, B. W., and Wilcox, P. D., 2005, “Post-Processing of the Full Matrix of Ultrasonic Transmit – Receive Array Data for Non-Destructive Evaluation,” **38**, pp. 701–711.

[41] Drinkwater, B. W., and Wilcox, P. D., 2006, “Ultrasonic Arrays for Non-Destructive Evaluation: A Review,” NDT E Int., **39**(7), pp. 525–541.

[42] Zhang, J., Drinkwater, B. W., and Wilcox, P. D., 2013, “Efficient Computation of Delay Law for Imaging Structure with a Complex Surface,” IEEE Int. Ultrason. Symp. IUS, pp. 139–142.

[43] Zhang, J., Drinkwater, B. W., and Wilcox, P. D., 2013, “Comparison of Ultrasonic Array Imaging Algorithms for Non-Destructive Evaluation,” AIP Conf. Proc., **1511**(8), pp. 825–832.

[44] Zhang, J., Drinkwater, B., and Wilcox, P., 2014, “Efficient Immersion Imaging of Components with Nonplanar Surfaces,” IEEE Trans. Ultrason. Ferroelectr. Freq. Control, **61**(8), pp. 1284–1295.

[45] Fan, C., Caleap, M., Pan, M., and Drinkwater, B. W., 2014, “A Comparison between Ultrasonic Array Beamforming and Super Resolution Imaging Algorithms for Non-Destructive Evaluation,” Ultrasonics, **54**(7), pp. 1842–1850.

[46] Ozaki, Y., Sumitani, H., Tomoda, T., and Tanaka, M., 1988, “A New System for Realtime Synthetic Aperture Ultrasonic Imaging,” IEEE Trans. Ultrason. Ferroelectr. Freq. Control, **35**(6), pp. 828–838.

[47] Zhang, J., Drinkwater, B. W., and Wilcox, P. D., 2008, “Defect Characterization Using an Ultrasonic Array to Measure the Scattering Coefficient Matrix,” IEEE Trans. Ultrason. Ferroelectr. Freq. Control, **55**(10), pp. 2254–2265.

[48] Zhang, J., Drinkwater, B. W., and Wilcox, P. D., 2010, “The Use of Ultrasonic Arrays to Characterize Crack-like Defects,” J. Nondestruct. Eval., **29**(4), pp. 222–232.

[49] Peng, C., Bai, L., Zhang, J., and Drinkwater, B. W., 2018, “The Sizing of Small Surface-Breaking Fatigue Cracks Using Ultrasonic Arrays,” NDT E Int., **99**, pp. 64–71.

[50] Zhang, J., Drinkwater, B. W., and Wilcox, P. D., 2012, “Effect of Roughness on Imaging and Sizing Rough Crack-like Defects Using Ultrasonic Arrays,” IEEE Trans. Ultrason. Ferroelectr. Freq. Control, **59**(5), pp. 939–948.

[51] Bai, L., Velichko, A., and Drinkwater, B. W., 2019, “Grain Scattering Noise Modelling and Its Use in the Detection and Characterisation of Defects Using Ultrasonic Arrays,” IEEE Trans. Ultrason. Ferroelectr. Freq. Control, **66**(11), pp. 1–1.

[52] Velichko, A., Wilcox, P. D., and Drinkwater, B. W., 2013, “Array Imaging and Defect Characterization Using Post-Processing Approaches,” *Advances in Acoustic Microscopy and High Resolution Imaging*, John Wiley & Sons, Ltd, pp. 231–275.

[53] Bai, L., Velichko, A., and Drinkwater, B. W., 2015, “Characterization of Defects Using Ultrasonic Arrays: A Dynamic Classifier Approach,” IEEE Trans. Ultrason. Ferroelectr. Freq. Control, **62**(12), pp. 2146–2160.

[54] Bai, L., Velichko, A., and Drinkwater, B. W., 2015, “Ultrasonic Characterization of Crack-like Defects Using Scattering Matrix Similarity Metrics,” IEEE Trans. Ultrason. Ferroelectr. Freq. Control, **62**(3), pp. 545–559.

[55] Malkin, R., Caleap, M., and Drinkwater, B. W., 2016, “A Numerical Database for Ultrasonic Defect Characterisation Using Array Data: Robustness and Accuracy,” NDT E Int., **83**, pp. 94–103.

[56] Safari, A., Zhang, J., Velichko, A., and Drinkwater, B. W., 2018, “Assessment Methodology for Defect Characterisation Using Ultrasonic Arrays,” NDT E Int., **94**(November 2017), pp. 126–136.

[57] Bai, L., Velichko, A., and Drinkwater, B. W., 2018, “Ultrasonic Defect Characterisation—Use of Amplitude, Phase, and Frequency Information,” J. Acoust. Soc. Am., **143**(1), pp. 349–360.

[58] Wright, M., Lesage, J., Marvasti, M., Peters, S., and Matheson, M., “Calibration Procedure Developed for FMC-TFM Based Imaging System.”

[59] Budyn, N., Bevan, R. L. T., Zhang, J., Croxford, A. J., and Wilcox, P. D., 2019, “A Model for Multiview Ultrasonic Array Inspection of Small Two-Dimensional Defects,” IEEE Trans. Ultrason. Ferroelectr. Freq. Control, **66**(6), pp. 1129–1139.

[60] Weston, M., 2011, “Advanced Ultrasonic Digital Imaging and Signal Processing for Applications in the Field of Non- Destructive Testing.”

[61] Sutcliffe, M., Weston, M., Dutton, B., and Cooper, I., 2012, “Real-Time Full Matrix Capture with Auto-Focussing of Known Geometry Throuogh Dual Layered Media,” Bindt, (1), pp. 1–8.

[62] Weston, M., Mudge, P., Davis, C., and Peyton, A., 2012, “Time Efficient Auto-Focussing Algorithms for Ultrasonic Inspection of Dual-Layered Media Using Full Matrix Capture,” NDT E Int., **47**, pp. 43–50.

[63] Le Jeune, L., Robert, S., Villaverde, E. L., and Prada, C., 2015, “Multimodal Plane Wave Imaging for Non-Destructive Testing,” Phys. Procedia, **70**, pp. 570–573.

[64] De, T., Doctorale, É., and Prada, M. C., 2016, “Léonard Le Jeune Docteur de l ’ Université Paris-Diderot – Paris 7 Imagerie Ultrasonore Par Émission d ’ Ondes Planes Pour Le Contrôle de Structures Complexes En Immersion.”

[65] Le Jeune, L., Robert, S., Lopez Villaverde, E., and Prada, C., 2016, “Plane Wave Imaging for Ultrasonic Non-Destructive Testing: Generalization to Multimodal Imaging,” Ultrasonics, **64**, pp. 128–138.

[66] Quaegebeur, N., and Masson, P., 2012, “Correlation-Based Imaging Technique Using Ultrasonic Transmit-Receive Array for Non-Destructive Evaluation,” Ultrasonics, **52**(8), pp. 1056–1064.

[67] Quaegebeur, N., Padois, T., Gauthier, P. A., and Masson, P., 2016, “Enhancement of Time-Domain Acoustic Imaging Based on Generalized Cross-

Correlation and Spatial Weighting," Mech. Syst. Signal Process., **75**, pp. 515–524.

[68] Masson, P., Quaegebeur, N., and Mainguy, F., 2016, "Implantation Efficace de l'acquisition Pleine Matrice En Imagerie Ultrasonore Temps R´eel," Congrès Fr. d'Acoustique, pp. 1719–1725.

[69] Bannouf, S., Robert, S., Casula, O., and Prada, C., 2013, "Data Set Reduction for Ultrasonic TFM Imaging Using the Effective Aperture Approach and Virtual Sources," J. Phys. Conf. Ser., **457**.

[70] Cruza, J. F., and Camacho, J., 2016, "Total Focusing Method with Virtual Sources in the Presence of Unknown Geometry Interfaces," IEEE Trans. Ultrason. Ferroelectr. Freq. Control, **63**(10), pp. 1581–1592.

[71] Cruza, J. F., Camacho, J., Serrano-Iribarnegaray, L., and Fritsch, C., 2013, "New Method for Real-Time Dynamic Focusing through Interfaces," IEEE Trans. Ultrason. Ferroelectr. Freq. Control, **60**(4), pp. 739–751.

[72] Camacho, J., Cruza, J. F., Fritsch, C., and Moreno, J. M., 2014, "Automatic Dynamic Depth Focusing for NDT," AIP Conf. Proc., **1581 33**(4), pp. 57–64.

[73] Kerr, W., Pierce, S. G., and Rowe, P., 2016, "Investigation of Synthetic Aperture Methods in Ultrasound Surface Imaging Using Elementary Surface Types," Ultrasonics, **72**, pp. 165–176.

[74] Camacho, J., and Cruza, J. F., 2015, “Auto-Focused Virtual Source Imaging with Arbitrarily Shaped Interfaces,” IEEE Trans. Ultrason. Ferroelectr. Freq. Control, **62**(11), pp. 1944–1956.

[75] Kaczkowski, P., 2016, “Arbitrary Waveform Generation with the Verasonics Research Ultrasound Platform,” pp. 1–18.

[76] Cochran, S., 2012, “1 - Piezoelectricity and Basic Configurations for Piezoelectric Ultrasonic Transducers,” *Woodhead Publishing Series in Electronic and Optical Materials*, K.B.T.-U.T. Nakamura, ed., Woodhead Publishing, pp. 3–35.

[77] “IMASONIC - Phased Array Probe Types” [Online]. Available: http://www.imasonic.com/Industry/PA_intro.php. [Accessed: 14-Sep-2019].

[78] Olympus NDT, 2007, Advances in Phased Array Ultrasonic Technology Applications, Olympus.

[79] Ouellette, A., Titov, S., Ghaffari, B., Hetrick, E., Maev, R. G., Ouellette, A., Titov, S., Ghaffari, B., Hetrick, E., and Maev, R. G., 2017, “Full Matrix Capture for Ultrasonic Imaging through Brazed Surfaces Full Matrix Capture for Ultrasonic Imaging through Brazed Surfaces,” *26th ASNT Research Symposium*, The American Society for Nondestructive Testing, Inc, pp. 13–16.

[80] Ouellette, A., Titov, S., Ghaffari, B., Hetrick, E., and Maev, R., 2017, “Full Matrix Capture for Ultrasonic Imaging through Brazed Surfaces,” *ASNT 26th Research Symposium*, Jacksonville, FL.

[81] Zhang, J., Drinkwater, B. W., Wilcox, P. D., and Hunter, A. J., 2010, “Defect Detection Using Ultrasonic Arrays: The Multi-Mode Total Focusing Method,” NDT E Int., **43**(2), pp. 123–133.

## VITA AUCTORIS

| | |
|---|---|
| NAME: | Andrew Ouellette |
| PLACE OF BIRTH: | Windsor, ON |
| YEAR OF BIRTH: | 1990 |
| EDUCATION: | University of Windsor, B.Sc., Windsor, ON, 2013<br>University of Windsor, M.Sc., Windsor, ON, 2015 |